2020

Understanding and Predicting Properties of Low-dimensional Functional Materials from First-principles

Naseem Ud Din
University of Central Florida

UNDERSTANDING AND PREDICTING PROPERTIES OF LOW-DIMENSIONAL FUNCTIONAL MATERIALS FROM FIRST-PRINCIPLES

by

NASEEM UD DIN
M.Phil. Quaid-I-Azam University Islamabad Pakistan 2012
M.Sc. University of Central Florida, USA, 2017

A dissertation submitted in partial fulfillment of the requirements
of the degree of Doctor of Philosophy
in the Department of Physics
in the College of Sciences
at the University of Central Florida
Orlando, Florida

Fall Term
2020

Major Professor: Talat Shahnaz Rahman

ABSTRACT

A periodic network with uniform single metal active site, in coordination with redox-active organic ligands, is a promising class of materials for next generation single atom catalysts. Towards this quest, in this dissertation I have carried out first-principles density functional theory (DFT) based calculations of the geometrical and electronic structure and magnetic properties of several transition-metal-organic-chains (TM-C) both in gas phase as well as on Au(111) surface. Of particular interest are dipyridyltetrazine (DT), Bis-pyrimidine (BP), and 1,10-phenanthroline5,6-dione, (PDO) ligands used to design the TM-C with several single TM atoms as the coordination center. I have screened several TM atoms to get their coordination geometry (stable structure) as well as analyzing their chemical activity through adsorption of small molecules on the TM center. Our results suggest that TM atoms with partially occupied *d*-orbitals exhibit strong affinity, while the TM atoms with fully occupied *d*-orbitals show weak affinity to the CO and O_2 molecule. We also investigate the effect of support (Au(111)) on geometry and charge state in case of V-BP and V-PDO systems, and found that the support not only alters the local coordination of TM-Cs, but also has significant charge transfer from TM-C to Au(111).

The tetrazine-based ligand, DT is only able to undergo a two-electron reduction, which limits the complexation to one metal per ligand. We studied the complexation of tetraethyltetraaza-anthraquinone (TAAQ) with elemental Fe, leading to complex metal–organic chains. We utilized the multiple binding pockets of TAAQ and achieve higher metal:ligand (M:L) ratios. Our results of various Fe:TAAQ ratio, suggests that thermodynamically one cannot create FeTAAQ species with higher than 2:1 M:L ratio.

The second part of this dissertation deals with electronic structure and excitation spectrum of hydrogenated single layer and clean bilayer MoS_2. We calculate the excitation spectrum of single-layer MoS_2 at several hydrogen coverages by using Density-Matrix Time-Dependent Density-Functional Theory (TDDFT). Binding energies of the excitons of the hydrogenated MoS_2 are relatively large (few tens of meV), making their experimental detection facile and suggesting hydrogenation as a knob for tuning the optical properties of single-layer MoS_2. To examine ultrafast charge dynamics in bilayer MoS_2, we applied DFT+Liouville equation approach and found that in conjunction with electron-phonon interaction ultrafast charge dynamics has a strong effect on the calculated emission spectrum. Our results reveal the importance of ultrafast charge dynamics in understanding photoemissive properties of a few-layer transition-metal dichalcogenide.

ACKNOWLEDGEMENTS

First, I would like to take this opportunity to express my sincere gratitude to my advisor Professor Talat S. Rahman for her patience, motivation, and guidance. Her great enthusiasm and rigorous attitude towards the research influenced me in many ways. I was lucky to have her as my mentor: she provided me with opportunities to work independently as well as in collaboration with various experimental groups. She embodies great leadership and thorough professional attitude, which directly and indirectly influenced me as a learner as a team member in her group. Besides her academic guidance, she also provides a very conducive work environment within the group, which helped all of us mentally and emotionally.

I want to thank to Dr. Duy Le. I started working him on various projects since I joined the group. He helped me technically throughout the course of my dissertation time. He is willing to take the initiative to new projects and walk me through every step toward arriving at a sound understanding of the problem at hand and, more generally, how to proceed effectively and efficiently to set and achieve goals.

I would like to thank Dr.Volodymyr Turkowski. I have worked with him in many different projects. I had extensive discussions with him that helped me gain theoretical understanding of various physical phenomena at the microscopic level and at ultrafast time scales. He also worked with me on projects that are not part of this dissertation.

I want to extend my gratitude to Professor Kenneth Caulton and Professor Steven L. Tait of University of Indiana. I have been working with them for the past few years. They guided me in

various projects and helped me explain the results so that a broader audience can benefit from the interdisciplinary aspect of my research.

I want to thank the former and current members of Dr. Rahman's research group: Dr Tao Jiang, , Dr. Takat B. Rawal, Dr. Zahra Hooshmand, Dr. Shree Ram Acharya, Rainier Berkley, Andre Childs, Dave Austin, Mahboob Ur Rehman, Dave Austin, Eric Switzer, and Jia Shi for academic discussions and the friendly atmosphere in the office.

I also would like to thank my wife Sana Akbar for her support and company. The years spent with her have been full of happiness and wonderful moments. Her encouragement always helps me overcome difficulties in academia and in life.

I would like to express all my deepest gratitude to my parents: for their unconditional support uninterrupted encouragement. They brought me up well and educated me well. They did their best to provide me with a good environment. Their kindness and courage made me into a positive and optimistic person. There are no words to convey how important they are and how much I love them. I could not have completed my study without their support.

Finally, I would like to thank my brothers Nasir Ud Din and Jamal Ud Din who have helped me financially since I start my high school. Their constant help and support provided me opportunity to achieve the significant milestone.

TABLE OF CONTENTS

LIST OF FIGURES

LIST OF TABLES

CHAPTER 1: INTRODUCTION

Supported transition metal (TM) nanoparticles are the most widely used as a heterogeneous catalyst in industrial reactions due to their high dispersion, large concentration of highly undercoordinated surface sites, and metal–support interaction that often greatly alters their catalysis[1-4]. The size of TM nanoparticles is a key factor in determining the efficiency of such catalysts. Because under-coordinated TM atoms often function as the catalytically active sites, therefore the specific activity per TM atom usually increases with decreasing size of the TM particles. However, the surface free energy of TM significantly increases with decrease in the particle size. This increase in surface free energy may cause aggregation of TM atoms into small clusters. One way to stabilize and avoid the TM species from aggregation is by using an appropriate support material that strongly interacts with the metal species. Such a strong metal-support interaction helps in forming and maintaining finely dispersed metal clusters with a high catalytic activity, an approach industry has used for a long time. Nevertheless, in practical supported metal catalysts the size and morphology of adsorbed metal particles is inhomogeneous, usually consisting of a mixture of sizes from nanoparticles to sub-nanometer clusters. These nanoparticles possess broad distribution of undercoordinated metal sites. This heterogeneity reduces the activity and selectivity of the supported catalyst by hindering the control of active sites of interest.

The ultimate small-size limit for metal particles is the single-atom catalyst (SAC), which consists of isolated metal atoms singly dispersed on the support. SACs maximize the efficiency of metal atom use: That is particularly important for supported noble metal catalysts. Moreover, with well-

defined and uniform single-atom dispersion, SACs offer great potential for achieving high activity and selectivity [5].

The goal of this thesis is to investigate the geometrical structure, electronic structure, charge state of metal organic chains, and probe the chemical activity of single TM atoms in coordination with various organic ligands of different reducing capability. The design of well dispersed metal organic chains with single metal active site, can thus be used as catalyst for energy needs. A variety of problems are addressed in this dissertation. Together they invite us to examine electronic structure, magnetic ground state, vibrational spectrum, optical and excited states of a range of materials from one-dimensional transition-metal-organic chains to two-dimensional transition-metal dichalcogenide. The choice of systems investigated in this study is motivated by available experimental data, whose rationalization is one of the goals of the research. The results of this work are obtained by means of state-of-the-art computational approaches based on density functional theory (DFT) and time-dependent density functional theory(TDDFT). The organization of the rest of the dissertation is follows:

Chapter 2 introduces the set of theoretical methods employed in the present work to disclose certain qualities characteristic of electronic properties of involved metal organic chains and 2D MoS_2, the chapter discusses the DFT and TDDFT methods for optimizing structure and calculating of formation energies, adsorption energies, electronic structure, excited states, and related properties.

Chapter 3 describes an *ab-initio* study of the screening of geometry of transition metal-organic chains (TM-C) in forming a stable planar chain structure, of their electronic structure, and of the

propensity for adsorption of small molecules on metal site of TM-C, using density functional theory with the inclusion of van der Waals interactions. By using organic ligand di-pyridyl-tetrazine (DT), the screening study helps identify the candidate TM-DT on the basis of relative stability as well as propensity for incoming gas molecules to interact with TM centers.

Chapter 4 investigates the structure and chemical properties of non-planar metal-organic chains. The investigation (still ongoing) is based on the quest to discover how the chemistry of metal center may be tuned by different organic ligands. By using Bis-Pyrimidine (BP) as a ligand we are able to compare the reducing capacity of ligand BP with DT as well as change in oxidation state of TM center (see chapter 3). We also examined the effect of Au(111) support on the geometry and chemical state of M-BP chains.

Chapter 5 presents the results of our DFT calculations concerning phenanthroline dioxide (M-PDO), both in gas phase and on Au(111). It reveals chains with planar MO_2N_2 coordination environment. We computed the charge state of metal centers and PDO in M-PDO formation and study the effect of Au(111) support on charge state as well as structure of M-PDO chains (with M=Vanadium).

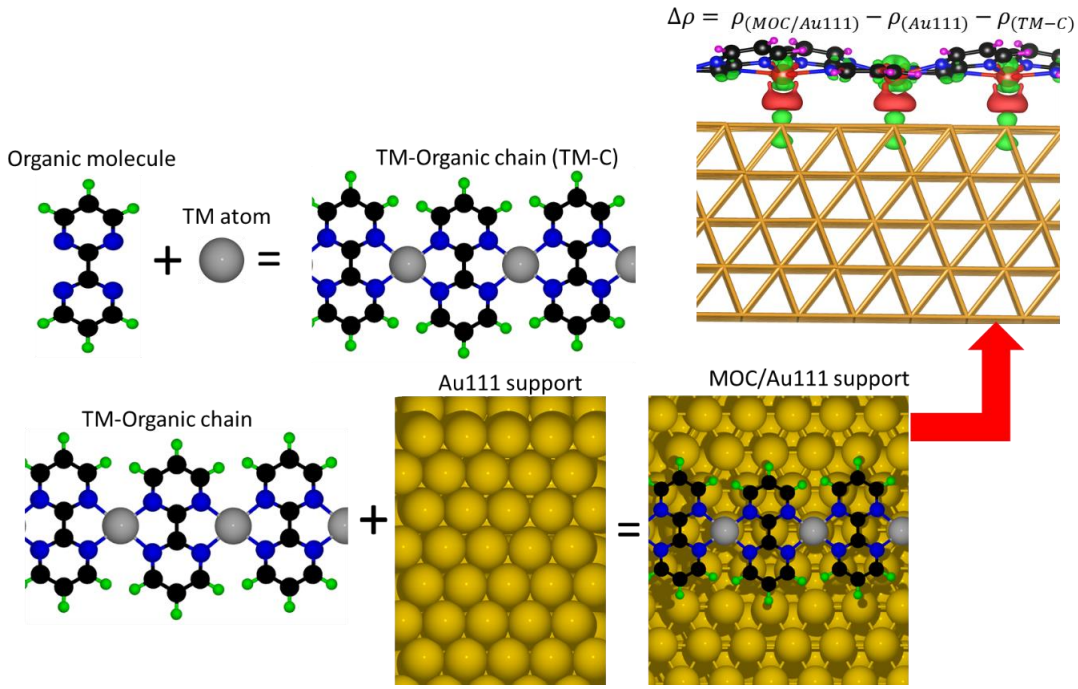

Figure 1.1: Schematic representation of metal organic complexation making a linear chain, in gas phase as well as on Au(111) support. The charge density difference cartoon shows the charge redistribution in TM-C on Au(111) support.

Chapter 6 We have shown the complexation between TAAQ ligand and iron. TAAQ functions as a redox-active ligand to form complex metal–organic structures. The TAAQ ligand is designed for greater reductive capacity and more metal binding pockets than do those taht are usually employed in metal–organic coordination networks. We also present the vibrational characteristics of TAAQ molecule and molecular network on Au(111) support and compared the results with experimental findings.

Chapter 7 deals with the excited states and exciton formation in hydrogenated MoS_2. We calculate the excitation spectrum of single-layer MoS_2 at several hydrogen coverages by using first-principles Density-Matrix Time-Dependent Density-Functional Theory (TDDFT).

In chapter 8 we discuss the ground state electronic structure and examine ultrafast charge dynamics in bilayer MoS_2, by applying density functional theory + Liouville equation approach. We found that in conjunction with electron-phonon interaction the ultrafast charge dynamics has a strong effect on the calculated emission spectrum. Our results thus reveal the importance of ultrafast charge dynamics in understanding photoemissive properties of a few-layer transition-metal dichalcogenide. The conclusion derived from the thesis is presented in chapter 9.

CHAPTER 2: THEORETICAL METHODS

2.1 Many-Body Equation

The many-body Hamiltonian describing a system of interaction electrons and nuclei reads

$$H = \hat{T}_e + \hat{T}_n + \hat{V}_{e-e} + \hat{V}_{n-n} + \hat{V}_{e-n} \quad (2.1)$$

Where $\hat{T}_e$ is the kinetic energy operators for the electrons in the system, $\hat{T}_n$ is the kinetic energy operator for each nucleus in the system, $\hat{V}_{e-e}$ is the potential energy arising from electron-electron interaction, $\hat{V}_{n-n}$ is the potential energy arising from nuclei-nuclei interaction also known as nuclear repulsion energy, $\hat{V}_{e-n}$ is the potential energy between electrons and nuclei in the system.

$$H = \sum_i -\frac{\hbar^2}{2m_e}\nabla_i^2 - \sum_i \frac{\hbar^2}{2M_I}\nabla_I^2 + \sum_{i\neq j}\frac{e^2}{2|r_i - r_j|} + \sum_{I\neq J}\frac{Z_I Z_J e^2}{2|R_I - R_J|} - \sum_{i,I}\frac{Z_I e^2}{2|r_i - R_I|} \quad (2.2)$$

Which represents a sum of kinetic energy terms $\hat{T}$ as well as electrostatic Coulomb interactions $\hat{V}$. In equation 2.2, r_i represents coordinates of the i'th electron (with mass m_e and charge -e), and R_I are the coordinated of I'th nucleus (with mass M_I and charge Z_Ie). The properties of the interacting system are now in principle derivable from the time-independent Schrödinger equation.

$$\hat{H}\Psi_i(r,R) = E_i\Psi_i(r,R) \quad (2.3)$$

where E_i is energy of the quantum mechanical state $\Psi_i(r,R)$. Here r and R are the full set of electronic and nuclear coordinated, respectively. If we have a system of N nuclei and n electrons, there will be totally $3n + 3N$ variables to describe the whole system. It is extremely challenging to obtain the full wave function of a system, thus necessary to apply approximations , for example, neglecting the kinetic energy of the nuclei (second term of equation 2.2) and the electrostatic

nucleus-nucleus repulsion (the fourth term of equation 2.2), since electrons move much faster than nuclei. This idea was an approximation introduced by Born and Oppenheimer in 1927 [6]

2.2 Thomas-Fermi Model

In 1920s Thomas and Fermi realized that statistical considerations should be considered to approximate the distribution of electrons in an atom. The Thomas model (1927) stated that "Electrons are distributed uniformly in the six-dimensional phase space for the motion of an electron at the rate of two for each h^3 of volume," and that there is an effective potential field that "is itself determined by the nuclear charge and this distribution of electrons" [7,8]. Assume that the space was divided into many small boxes (cells) with the same side length of l, and volume $\Delta V = l^3$, each containing fixed number of electrons ΔN. Assume that the electrons in each cell behave like independent fermions at 0 K, and the cells are independent to each other. The energy levels of a particle in a three-dimensional infinite well are given by the formula

$$\varepsilon(n_x, n_y, n_z) = \frac{h^2}{8ml^2}(n_x^2, n_y^2, n_z^2) \qquad (2.4)$$

where $n_x, n_y, n_z = 1,2,3$. For higher quantum numbers the number of distinct energy levels with energy smaller than ε can be approximated by 1/8th part of a sphere with radius R in the space (n_x, n_y, n_z). This number is the number of energy levels between ε and $\varepsilon + \delta\varepsilon$ is accordingly

$$\Phi(\varepsilon) = \frac{\pi}{6}\left(\frac{8ml^2\varepsilon}{h^2}\right)^{3/2} \qquad (2.5)$$

$$g(\varepsilon)\Delta\varepsilon = \varphi(\varepsilon + \delta\varepsilon) - \varphi(\varepsilon)$$

$$= \frac{\pi}{4}\left(\frac{8ml^2}{h^2}\right)^{3/2} \varepsilon^{1/2}\delta\varepsilon + O((\delta\varepsilon)^2) \qquad (2.6)$$

where the function $g(\varepsilon)$ is the density of state at energy ε. In order to compute the total energy for the cell with ΔN electrons, we need the probability for the state with energy ε, to be occupied which we call $f(\varepsilon)$. This is the Fermi-Dirac distribution.

$$f(\varepsilon) = \frac{1}{1+e^{\beta(\varepsilon-\mu)}} \qquad (2.7)$$

which at 0K reduces to a step function:

$$f(\varepsilon) = 1, \quad \varepsilon < \varepsilon_F$$

$$= 0, \quad \varepsilon > \varepsilon_F \quad \text{as} \quad \beta \to \propto \qquad (2.8)$$

where ε_F is so-called Fermi energy. All the states are with energy smaller than ε_F are occupied and those with energy greater than ε_F are empty. We can find the total energy of electrons in this cell by summing the contributions from different energy states.

$$\Delta E = 2\int \varepsilon f(\varepsilon) g(\varepsilon) d\varepsilon$$

$$= 4\pi \left(\frac{2m}{h^2}\right)^{\frac{3}{2}} l^3 \int_0^{\varepsilon_F} \varepsilon^{3/2} d\varepsilon$$

$$= \frac{8\pi}{5}\left(\frac{2m}{h^2}\right)^{3/2} l^3 \varepsilon_F^{5/2} \qquad (2.9)$$

where the factor 2 appears because each energy level is doubly occupied, by one electron with spin α and another with spin β. The Fermi energy ε_F is related to the number of electrons ΔN in the cell, through the formula

$$\Delta N = 2\int f(\varepsilon) g(\varepsilon) d\varepsilon$$

$$= \frac{8\pi}{5}\left(\frac{2m}{h^2}\right)^{3/2} l^3 \varepsilon_F^{3/2} \qquad (2.10)$$

Eliminating ε_F from equations 2.9 and 2.10 we obtain

$$\Delta E = \frac{3}{5}\Delta N \varepsilon_F$$

$$= \frac{3h^2}{10m}\left(\frac{3}{8\pi}\right)^{2/3} l^3 \left(\frac{\Delta N}{l^3}\right)^{5/3} \qquad (2.11)$$

This equation 2.11 is the relation between total kinetic energy and the electron density $\rho = {\Delta N}/{l^3} = {\Delta N}/{\Delta \mathrm{V}}$. The total kinetic energy can be found by adding the contributions from all cells.

$$T_{TF}[\rho] = C_F \int \rho^{5/3}(r) dr \qquad (2.12)$$

where the limit $\Delta V \to 0$, with $\rho = {\Delta N}/{l^3} = {\Delta N}/{\Delta \mathrm{V}} = \rho(r)$ finite has been taken to do integration instead of summation. This is the famous Thomas-Fermi kinetic energy functional. The energy formula for an atom in terms of electron density alone can be written as

$$E_{TF}[\rho(r)] = C_F \int \rho^{5/3}(r) dr - Z C_F \int \frac{\rho(r)}{r} dr + \frac{1}{2} \iint \frac{\rho(r_1)\rho(r_2)}{|r_1 - r_2|} dr_1 dr_2 \qquad (2.13)$$

This is the energy functional of Thomas-Fermi theory of atoms. We assume that the ground state of an atom can be achieved by minimizing the energy functional using electron density with a constraint.

$$N = N[\rho(r)] = \int \rho(r) dr \qquad (2.14)$$

where N is the total number of electrons in the atom. This constraint can be incorporated using Lagrange multiplier method. The ground-state electron density must satisfy the variational principle.

$$\delta\{E_{TF}[\rho] - \mu_{TF}(\int \rho(r)dr\ - N)\} = 0 \qquad (2.15)$$

which yields the Euler-Lagrange equation.

$$\mu_{TF} = \frac{\delta E_{TF}[\rho]}{\delta\rho(r)} = \frac{5}{3}C_F\rho^{2/3}(r) - \varphi(r) \qquad (2.16)$$

where

$$\varphi(r) = \frac{Z}{r} - \int \frac{\rho(r_2)}{|r-r_2|}dr_2 \qquad (2.17)$$

Thomas-Fermi model was model which cannot predict the molecular binding energy and also accuracy for atoms is not great as compared to other methods, so Thomas Fermi was considered to be an oversimplified model of not much importance for quantitative predictions in atomic, molecular and solid-state physics. However the landmark paper by Hohenberg and Kohn in 1964 [9] provided a fundamental mathematical theorems showing that the Thomas Fermi model may be treated as an approximation to an exact theory, the density functional theory for ground states.

2.3 The Hohenberg-Kohn Theorems

The first Hohenberg-Kohn Theorem states that " the external potential $v(r)$ is determined, within a trivial additive constant, by the electron density $\rho(r)$. To prove this theorem consider the nondegenerate ground state of a system with N-electrons with electron density $\rho(r)$. Assume if there were two external potentials v and v' differing by more than a constant, each giving same ρ for its ground state, we would have two Hamiltonians H and H'. The ground state densities would

be same and the normalized wave functions Ψ and Ψ′ would be different. Let us take Ψ′ as trial wavefunction for the $\hat{H}$,

$$E_0 < \langle \Psi' | \hat{H} | \Psi' \rangle = \langle \Psi' | \hat{H}' | \Psi' \rangle + \langle \Psi' | \hat{H} - \hat{H}' | \Psi' \rangle$$

$$= E_0' + \int \rho(r)[v(r) - v'(r)]\, dr \qquad (2.18)$$

where E_0 and E_0' are ground-state energies of $\hat{H}$ and $\hat{H}'$, respectively. Similarly take Ψ as a trial wavefunction for the $\hat{H}'$ problem.

$$E_0' < \langle \Psi | \hat{H}' | \Psi \rangle = \langle \Psi | \hat{H} | \Psi \rangle + \langle \Psi | \hat{H}' - \hat{H} | \Psi \rangle$$

$$= E_0 + \int \rho(r)[v(r) - v'(r)]\, dr \qquad (2.19)$$

Adding equation 2.18 and 2.19

$$E_0 + E_0' < E_0 + E_0' \qquad (2.20)$$

is a contradiction, so there cannot be two different v that give same ρ for their ground states. Thus, the electron density determines N and v and all related properties of ground-state, e.g. kinetic energy T[ρ], potential energy V[ρ] and total energy E[ρ]. We can write equation 2.13 to show explicit v dependence.

$$E_v[\rho] = T[\rho] + V_{ne}[\rho] + V_{ee}[\rho] \qquad (2.21)$$

$$= \int \rho(r) v(r) dr + F_{HK}[\rho]$$

where

$$F_{HK} = T[\rho] + V_{ee}[\rho] \qquad (2.22)$$

The second Hohenberg-Kohn theorem provides the energy variational principle. It reads: for a trial density $\tilde{\rho}(r)$, such that $\tilde{\rho}(r) > 0$ and $\int \tilde{\rho}(r)\, dr = N$,

$$E_0 \leq E_v[\tilde{\rho}] \qquad (2.23)$$

where $E_v[\tilde{\rho}]$ is energy functional. To prove this theorem, we know according to HK first theorem that $\tilde{\rho}$ determines its own $\tilde{v}$. Thus

$$\langle \Psi | \hat{H} | \Psi \rangle = \int \tilde{\rho}(r) v(r) dr + F_{HK}[\tilde{\rho}] = E_v[\tilde{\rho}] \geq E_v[\rho] \qquad (2.24)$$

Assuming the differentiability of $E_v[\rho]$ the variational principle requires that the ground-state density satisfy the stationary principle.

$$\delta\{E_v[\rho] - \mu(\int \rho(r) dr - N)\} = 0 \qquad (2.25)$$

which is Euler-Lagrange equation

$$\mu = \frac{\delta E_v[\rho]}{\delta \rho(r)} = v(r) + \frac{\delta F_{HK}[\rho]}{\delta \rho(r)} \qquad (2.26)$$

where μ is chemical potential. If we know $F_{HK}[\rho]$ equation 2.25 would be an exact equation for ground-state ρ. $F_{HK}[\rho]$ is universal functional of $\rho(r)$. If we have an explicit form of $F_{HK}[\rho]$ we can apply this method to any system.

2.4 Kohn-Sham Equations

The energy functional $E[\rho(r)]$ is, in principle, only dependent on 3-spatial variables of the density $\rho(r)$ and much simpler than the minimization of $\langle \Psi' | \hat{H} | \Psi' \rangle$ including 3n-dimensional variables of trial function Ψ'. However, the real difficulty is the evaluation of functional $E[\rho(r)]$; neither its explicit functional form is known nor is there a systematic procedure for finding such functional

dependence on $\rho(r)$. Indeed, the definition of $F_{HK}[\rho]$ requires the minimization of 3n-dimensional trial wave functions. The key realization was made by Kohn-Sham in 1965[10] with the emergence or "invention" of the Kohn-Sham(KS) fictitious noninteracting system. More precisely, constructing a fictitious system of non-interacting electrons that have the same ground-state density as the true system of interacting electrons. To understand the importance of this simplification, we will start by writing

$$\left\{-\frac{1}{2}\nabla^2 + V_s(\vec{r})\right\}\varphi_j(\overrightarrow{r}) = \epsilon_j\varphi_j(\overrightarrow{r}) \qquad (2.27)$$

$V_s(\vec{r})$ is the potential of single particle, and $\varphi_j(\overrightarrow{r})$ is the single-occupied wavefunction of the fictitious particles. In the case of a non-interacting system of n electrons, we can construct the wave function from the single electron wave function $\varphi_j(\overrightarrow{r})$ $(j = 1, \dots, n)$, called the Kohn-Sham(KS) orbitals, and the density is given by,

$$\rho(r) = \sum_{j=1}^{n}\varphi_j^*(r)\varphi_j(r) \qquad (2.28)$$

The charge density thus obtained is same as ground state charge density of real system. To find the KS potentials we will go back to the result obtained in Hohenberg-Kohn second theorem for a system of N interacting electrons

$$E[\rho(r)] = T[\rho(r)] + V[\rho(r)] + V_{ee}[\rho(r)] \qquad (2.29)$$

where

$$V[\rho(r)] = \int \rho(r)V_{ext}(r)d^3r \qquad (2.30)$$

and

$$V_{ee}[\rho(r)] = E_H[\rho(r)] + E_{XC}[\rho(r)] \qquad (2.31)$$

$E_H[\rho(r)]$ is classical Hartree potential.

$$E_H[\rho(r)] = \int \frac{\rho(r)}{|r-r'|} dr' \quad (2.32)$$

$E_{XC}[\rho(r)]$ is unknown, the ground state energy can be obtained using variational method.

$$E_{GS}[\rho(r)] = \frac{\delta E[\rho(r)]}{\delta \rho}|_{\rho=\rho_{GS}} \quad (2.33)$$

For non-interacting system

$$E_{GS}[\rho(r)] = \frac{\delta T[\rho(r)]}{\delta \rho}|_{\rho=\rho_{GS}} + V_s(r) \quad (2.34)$$

where

$$V_s(r) = V_{ext}[\rho(r) + V_H[\rho(r)] + V_{XC}[\rho(r)] \quad (2.35)$$

with

$$V_H[\rho(r)] = \frac{\delta E_H[\rho(r)]}{\delta \rho}|_{\rho=\rho_{GS}} \quad (2.36)$$

and

$$V_{XC}[\rho(r)] = \frac{\delta E_{XC}[\rho(r)]}{\delta \rho}|_{\rho=\rho_{GS}} \quad (2.37)$$

Therefore, Kohn Sham potential is the sum of original external potential, the classic Hartree potential and the unknown exchange-correlation potential. This also indicates that having that last piece of information about $V_{XC}[\rho(r)]$ can provide the set of self-consistent equations that finally gives the Hamiltonian and ground state energy of the original system using the non-interacting electrons, i.e. all the physical properties of a system in ground state. It is important to notice that these equations are based on two theorem which provide guidelines to find the global minimum of

system, by self-consistently finding the ground state density and therefore this is where DFT is limited in its power to describe physical properties of systems. It is "only" accurate for ground state properties and not excited states. The self-consistent Kohn-Sham equations can be solved iteratively.

2.5 Exchange and correlation Functionals

The only remaining part, and the most difficult task, is the explicit evaluation of the exchange-correlation functional $E_{XC}[\rho(r)]$. Unfortunately, there is no systematic method of evaluating E_{XC} for the real system of many electrons. However, owing to its unknown form the approximations are used widely with efficiency and low computational cost. While there are several approximations, we discuss only the two most used ones: the local density approximation and the generalized-gradient approximation functionals.

2.5.1 The local Density Approximation (LDA)

The local density approximation (LDA) assumes that the exchange-correlation energy experienced by each electron at point r is the same as that of a homogeneous electron gas with the same electron density. Using this approximation, the exchange energy and potential are calculated exactly as:

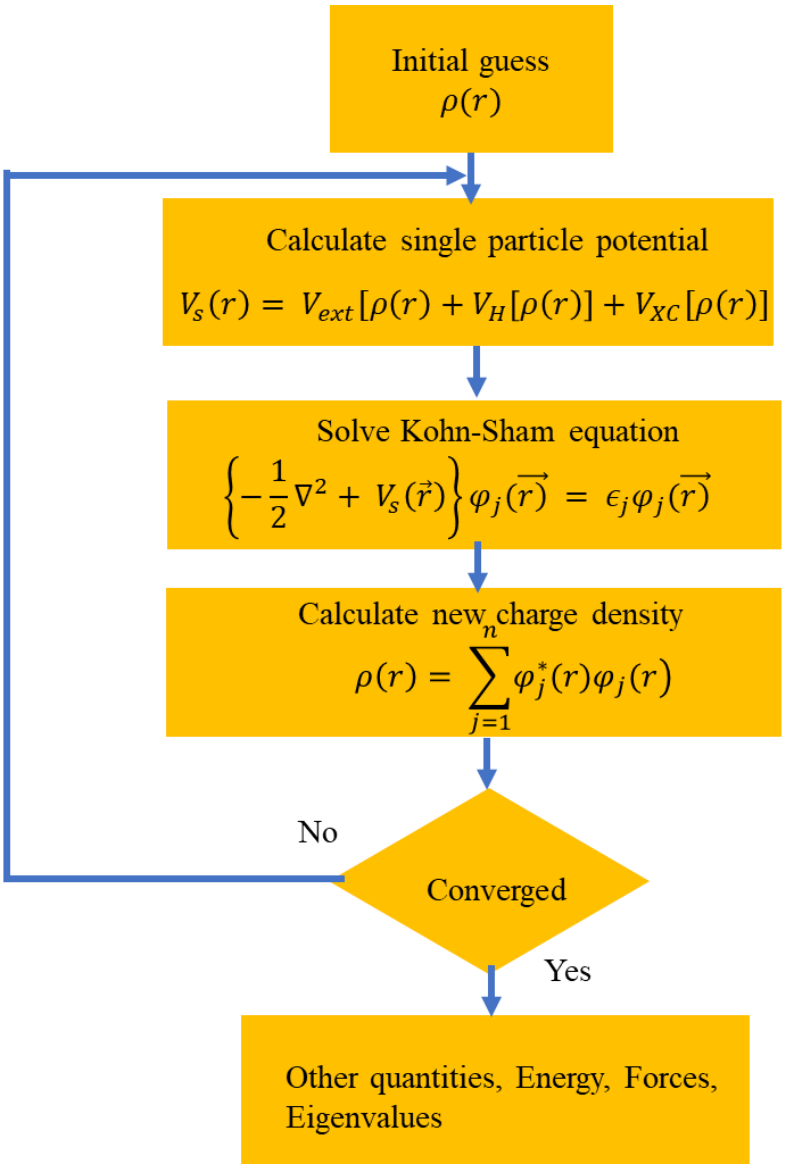

Figure 2.1: A flow chart representation of self-consistent ground state DFT calculations.

$$E_X = \int \rho(r) V_X dr \qquad (2.38)$$

and

$$V_X = -\left(\frac{81}{64}\right)^{1/3} \rho^{1/3}(r) = -\frac{0.4582}{r_s} \qquad (2.39)$$

r_s is the effective radius of the sphere with density $\rho(r)$ and is defined as:

$$\frac{4}{3}\pi r_s^3 = \frac{1}{\rho} \qquad (2.40)$$

Calculations of the correlation energy E_c and potential V_c is a difficult many-body problem. However, there are approximations to do so. Various approximations such as Vosko-Wilk-Nusiar (VWN) [11], Perdew-Zunger (PZ) [12] have been made to calculate the correlation energy. For example, the (PZ) approximation is widely used which presents the correlation potential as:

$$V_c = \{-0.1423(1 + 1.0529\sqrt{r_s} + 0.3334r_s \quad if\ r_s \geq 1$$

$$\{-0.048 + 0.0311\ln r_s + 0.002 r_s \ln r_s - 0.0016 r_s \ \ if\ r_s < 1 \qquad (2.41)$$

Though it is a very simplified approximation, yet LDA performs very well by calculating lattice parameters that are usually $1-2\%$ larger than experimental value. It fails, however, in many cases including: the magnetic properties, the electronic structure of strongly correlated systems, the dissociation energy of molecules and the adsorption energy of atoms and molecules on solid surfaces.

2.5.2 The Generalized-Gradient Approximation (GGA)

The next construction is to include both density and the gradient of the density in the evaluation, called the generalized gradient approximation (GGA). The first attempt in this direction was proposed by Kohn and Sham as gradient expansion approximation (GEA) [10]. However, this approximation resulted in worse failures than LDA. To solve this problem a variety of exchange-correlation functionals have been proposed in which the exchange-correlation energy has the following form

$$E_{XC} = \int F_{XC}[\rho(r), \nabla\rho(r), \nabla^2\rho(r)..]dr \qquad (2.42)$$

The generalized-gradient approximation (GGA) not only the exchange-correlation energy is a functional of electron density at $\vec{r}$, but also it is functional of charge variations at each point of space $\vec{r}$. GGA functionals have been calculated using two different strategies. The first known as *ab initio* approach, starts with the derivation of theoretical expression for F_{XC} . It then requires the functional to satisfy some or all known properties of the E_{XC} . The second strategy, known as an empirical approach, is based on fitting all the parameters of F_{XC} to reproduce many known experimental values. There are many variations for first one such as LYP[13] , PW91 [14] and PBE [15]. One of the shortcomings of both LDA and GGA is that because the non-locality of electrons is not fully considered, both approximations do not capture the long-range interactions.

2.6 van der Waals interactions in DFT

The van der Waals interactions are relatively weak, widespread in nature, play an important role in many chemical systems, describing interactions between atoms and molecules. For example, van der Waals interaction is the source of stability for physisorption of molecules on surfaces. DFT with LDA and GGA functionals has been extremely successful in predicting structural, elastic, vibrational properties of materials bound by metallic, ionic, covalent bonds, but neither LDA nor GGA describe vdW interaction. There are two ways: The first way is to add an empirical damped dispersion correction, which has been presented in well-known methods, such as, DFT-D [16] DFT-D2[17] ,and DFT-D3 [18],The second way is to develop a truly non-local exchange-correlation functional as in the well-known vdw-DF [19]and vdw-DF2 [20] methods.

2.6.1 DFT-D

A simple and crude approximation is the pair interaction between two ions, which was proposed by Grimme in 2004 [16], known as DFT-D. In this approximation, the total energy of the system consists of two different parts: (1) the total energy from DFT calculation (2) and an empirical damped dispersion correction

$$E_{tot}^{DFT-D} = E_{tot}^{DFT} + E_{tot}^{disp} \quad (2.43)$$

$$E_{tot}^{disp} = -s_6 \sum_{i=1}^{N_{at}-1} \sum_{j=i+1}^{N_{at}} \frac{C_6^{ij}}{R_{ij}^6} f_{dmp}(R_{ij}) \quad (2.44)$$

Here, N_{at} is the number atoms in the system, C_6^{ij} denotes the dispersion coefficient for atom pair ij, s_6 and f_{dmp} are scaling factors and damping function, R_{ij} is an interatomic distance.

2.6.2 DFT-D2

Part of the problems of the original DFT-D approach, especially with heavier elements, can be traced back to the combination rule employed for the composed C_6^{ij} coefficients that gives too much weight to the smaller coefficient (lighter atom). Careful testing of systems including elements up to xenon and large hydrocarbons with many hydrogen atoms showed that a geometric mean of the coefficient would lead to a better approximation. This is the second version of Grimme's dispersion correction method [17], labeled as DFT-D2:

$$E_{tot}^{disp} = -S_6 \sum_{i=1}^{N_{at}-1} \sum_{j=i+1}^{N_{at}} \frac{C_6^{ij}}{R_{ij}^6} f_{dmp}(R_{ij}) \quad (2.45)$$

Where s_6 and $f_{dmp}(R_{ij})$ are scaling factors and damping function to avoid the divergence at short distance and is given by

$$f_{dmp}(R_{ij}) = 1/1 + e^{-d(\frac{R_{ij}}{R_{r-1}})} \quad (2.46)$$

Where d=20; R_{ij} is the sum of atomic vdW radii of atom i and j. The coefficient C_6^{ij} is calculated as the follow:

$$C_6^{ij} = \sqrt{C_6^i C_6^j} \quad (2.47)$$

These coefficients are computed for a list of atoms corresponding to each DFT functional in [17]. Although DFT-D2 works very well in producing accurate binding energies between molecules as wells as atoms, it does not work very well for extended systems since it is independent of system. A newer version of this method was proposed by Grimme *et al*. in 2010 [18], which addresses these issues, known as DFT-D3

2.6.3 DFT-D3

DFT-D3 is the third version of DFT-D, which was proposed by Grimme *et al*. in 2010. The dispersion coefficients are calculated from first principles based pre-calculated C_6 coefficients, which is from a large database of dispersion coefficients calculated accurately for any pair of atoms:

$$E_{tot}^{disp} = E_{n=6}^{disp} + E_{n=8}^{disp} \quad (2.48)$$

Where

$$E_6^{disp} = s_6 f_6(r_{ij}) \frac{C_6^{ij}}{r_{ij}^6} \quad (2.49)$$

Here the coefficients

$$f_n(r_{ij}) = \frac{1}{1+6\left[\frac{r_{ij}}{s_n R_{ij}}\right]^{-\alpha}} \quad (2.50)$$

Where s_n and α are empirical parameters, R_{ij} is the cutoff radius of atom *i* and *j*.

2.7 van der Waals Density Functional

The methods vdW-DF and vdDW-DF2 [19,20] are vdW exchange-correlation functionals to take into account the vdW interaction into DFT calculations. In contrast to empirical damped dispersion corrections based on external parameters like the DFT-D family, the vdW-DF functional directly calculate the dispersion interaction from electron density. The vdW-DF method uses an exchange-correlation functional, which combines of all the correlations for all ranges:

$$E_{XC} = E_X^{GGA}[\rho(r)] + E_C^{LDA}[\rho(r)] + E_C^{non-local}[\rho(r)] \quad (2.51)$$

The non-local term for correlation energy is given by

$$E_C^{non-local}[\rho(r)] = \frac{1}{2}\int d^3r d^3r' \, \rho(r)K(r,r')\rho(r') \quad (2.52)$$

$K(r,r')$ is a universal kernel and its definition for different classes of vdW-DF methods can be found in the literature. The first and second terms in eq. (2.52) are the exchange energy evaluated using GGA functional and the local correlation energy obtained using LDA. Although this method is computationally more expensive than DFT-D methods, it improves the values of lattice parameter and binding energies because of more accurate approach for considering the non-local interactions.

2.8 Practical DFT Methods for Periodic Structures

Even after we have in hand the approaches to calculate the exchange-correlation functional and van der Waals interactions, it is still a problem to apply DFT to a realistic system because it contains infinite number of electrons and nuclei. By the help of Bloch's theorem [21], one can apply DFT methods to a periodic system.

2.8.1 Bloch's Theorem

Schrödinger's equation of an independent electron can write as

$$\left[-\frac{\hbar}{2m}\nabla^2 + V + V(r)\right]\Psi(r) = E\,\Psi(r) \qquad (2.53)$$

If the electron is in a periodic potential

$$V(r+l) = V(r) \qquad (2.54)$$

The solution should be plane waves

$$\Psi(r) = u_k(r)e^{ik.r} \qquad (2.55)$$

Where $u_k(r)$ have the same periodic symmetry as the lattice

$$u_k(r+l) = u_k(r) \qquad (2.56)$$

For the wave function at $r+l$, it should be

$$\Psi_k(r+l) = u_k(r+l)e^{ik.(r+l)} = u_k(r)e^{ik.l}e^{ik.r} = e^{ik.l}\Psi_k(r) \qquad (2.57)$$

Which is known as Bloch's theorem. The physical meaning is that the wave function at $r+l$ and r is with same probability density $|\psi(\boldsymbol{r})|^2$, whereas different phase factor $e^{ik.l}$.

2.8.2 k-point Sampling

Using Bloch's theorem there could be infinite number of vectors which give the same wave function. Since reciprocal lattice is also periodic it can be considered as a collection of unit cells in momentum space. This unit cell is called Brillouin Zone (BZ). The whole momentum space can be reproduced by translation of k vectors of BZ. Therefore, if we solve the KS equations at certain k- points we can have reasonable results for the unit cell. The set of these k points is called k-point sampling. The BZ is sampled by equally spaced mesh points which is called Monkhorst and Pack method [22]. The accuracy of calculation is dependent on the density of mesh points. In practice one needs to test the accuracy of calculations for different number of k-points until the increase in the density of mesh points does not affect the energy of system, i.e. convergence is achieved.

2.8.3 Plane-wave Basis Sets

Assuming that a unit cell is defined with three vectors a_1, a_2, and a_3 , the volume of the unit cell is

$$\Omega = a_1.(a_2 \times a_3) \qquad (2.58)$$

We consider a periodic case in which $\boldsymbol{r}$ and $\boldsymbol{r}$+$\boldsymbol{R}$ has same properties. For direct lattice vectors $\boldsymbol{R}$, one can write it as

$$R = n_1 a_1 + n_2 a_2 + n_3 a_3 \qquad (2.59)$$

where a_1, a_2, and a_3 are all integers. And there are three vectors b_1 , b_2, and b_3, in reciprocal lattice and there is a relationship between a_i and b_i:

$$b_i.a_i = 2\pi\delta_{ij} \qquad (2.60)$$

We can write the reciprocal lattice vector as

$$G = n_1 b_1 + n_2 b_2 + n_3 b_3 \quad (2.61)$$

Bloch's function can be described in reciprocal lattice vectors:

$$\psi_k(r) = \sum_G C_{k+G}\, e^{i(k+G).r} \quad (2.62)$$

Where $u_k(r)$ also being periodic in the reciprocal space

$$u_k(r) = \sum_G C_{k+G} e^{iG.r} \quad (2.63)$$

Kinetic energy operator is diagonal in the plane wave basis

$$-\frac{1}{2}\nabla^2\psi_k(r) = -\frac{1}{2}(i(k+G))^2 \sum_G C_{k+G} e^{i(k+G).r} = \frac{1}{2}(k+G)^2\psi_k(r) \quad (2.64)$$

So kinetic energy cutoff is defined as:

$$E_{cut} = \frac{1}{2}|k+G|^2 \quad (2.65)$$

However, the coefficients, $k+G$, for the plane waves with small kinetic energies are more important than those with large kinetic energies. Thus, the plane wave basis set can be truncated to include only plane waves that have kinetic energies that are smaller than some cutoff energy as illustrated. Kohn-Sham equation can be rewritten with Plane-wave Basis Sets as:

$$E_{cut} = \sum_{G'} \left[\frac{1}{2}|k+G|^2\delta_{GG'} + V_{GG'}^{eff}\right] C_{i,k+G} = \varepsilon_i C_{k+G'} \quad (2.66)$$

where

$$V_{GG'}^{eff} = \int V_{ext}^{eff} e^{i(G-G')} dr \quad (2.67)$$

Here E_{cut} is the plane wave cutoff energy. It is the highest kinetic energy of all basis functions and determines the number of basis functions. The basis set convergence can be systematically

controlled by increasing the plane wave cutoff energy. To reduce errors, we can increase the cutoff energy, the strength of plane-wave basis sets is its implementation ease, controllable accuracy (by varying the number of plane-wave basis set), and its appropriateness for periodic systems.

2.9 Pseudopotential Approximation

Pseudopotentials constitutes a possible way of avoiding atomic core states in first principles calculations of molecules and solids. The need for avoid core states arises in view of both the expensive work of considering all atomic states in such calculations, and that chemical bonds in molecules and solids involve valence states to a major extent. To avoid huge calculation on core electrons, the pseudopotential approximation was developed by Phillips and Kleinman [23], which behave as a smooth plane wave at the core replacing those of the core electrons. Real wave function of the valence electrons $\psi_v(r,k)$ is supposed to combine linearly with a smooth valence function $\lambda_v(r,k)$ and expand the remaining portion in terms of core states $\phi_c(r,k)$, which can be described as:

$$\psi_v(r,k) = \lambda_v(r,k) - \sum_c \sigma_{cv}(k)\phi_c(r,k) \qquad (2.68)$$

Because the smooth valence function $\lambda_v(r,k)$ is orthogonal to core states $\phi_c(r,k)$, we can get the portion parameter $\sigma_{cv}(k)$:

$$\sigma_{cv}(k) = \int dr' \phi_c^*(r,k) \qquad (2.69)$$

Schrödinger's equation of valence electrons is

$$\hat{H}\psi_v(r,k) = E_v(k)\psi_v(r,k) \qquad (2.70)$$

Schrödinger's equation of core electrons is

$$\hat{H}\phi_c(r,k) = E_c(k)\phi_c(r,k) \quad (2.71)$$

Substituting equation 2.69 into equation 2.71

$$\hat{H}[\lambda_v(r,k) - \sum_c \int dr' \phi_c^*(r,k)\lambda_v(r,k)\phi_c(r,k)] = E_v(k)\psi_v(r,k) \quad (2.72)$$

The left-hand side of this equation

$$\hat{H}\lambda_v(r,k) - E_c(k)\phi_c(r,k)\sum_c \int dr' \phi_c^*(r,k)\lambda_v(r,k) \quad (2.73)$$

The right-hand side of the equation reads

$$E_v(k)\lambda_v(r,k) - E_v(k)\sum_c \int dr' \phi_c^*(r,k)\lambda_v(r,k)\phi_c(r,k) \quad (2.74)$$

Left-hand side=right hand side

$$[\hat{H} + (E_v(k) - E_v(k))\int dr' \phi_c^*(r,k)\phi_c(r,k)]\lambda_v(r,k)] = E_v(k)\lambda_v(r,k) \quad (2.75)$$

We define the pseudopotential

$$\hat{H}_{pseudo} = \hat{H} + (E_v(k) - E_v(k))\int dr' \phi_c^*(r,k)\phi_c(r,k) \quad (2.76)$$

In the first-principle calculation, norm-conserving pseudopotential method is one of common methods, which was proposed by Hamann, Schlüter and Chiang in 1979 [24]. The new family of energy-independent pseudopotentials introduced here have the following desirable properties

(1) Real and pseudo valence eigenvalues agree for a chosen "prototype" atomic configuration.

(2) Real and pseudo atomic wave functions agree beyond a chosen "core radius"r_c.

(3) The integrals from 0 to r of the real and pseudo charge densities agree for $r < r_c$, for each valence state (norm conservation).

(4) The logarithmic derivatives of the real and pseudo wave function and their first energy derivatives agree for $r < r_c$

However, for elements belonging to Period 1 element and transition element, norm-conserving pseudopotential required large values of E_{CUT}. In 1990, Vanderbilt proposed a new and radical method for generating pseudopotentials by relaxing the norm-conservation constraint to obtain smoother pseudo wave functions [25].Pseudopotentials generated in this way (due to their softness) require a much smaller planewave cutoff and thus a much smaller number of planewaves. For this reason, they are usually called as ultrasoft pseudopotentials (USPP). This can be done by splitting the pseudo wave functions into two parts: Ultrasoft valence wave function that do not fulfill the norm conservation criteria In 1994, Blöchl introduced the projector-augmented wave method (PAW) [26] an all-electron equivalent method – that can be used for high accuracy first principles simulations. In (1999), Kresse and Joubert [27] made reformulation of the method to calculate electron density and illustrated the internal relations between USPP and PAW, so that PAW method became widely used. The main idea of the method is to use a transformation operator that can map the true wave functions onto pseudo wave functions. Since pseudo wave functions are computationally favorite, they are used in the Kohn-Sham equation. Once pseudo wave functions are obtained, the transformation operator constructs real wave functions that are used for evaluating observables.

2.10 Bader Charge Analysis

In so many cases the charge transferred among interacting atomic species, provides useful insight on the nature of bonding. However, the main basis for solving Kohn-Sham equations is electron density which is a continuous quantity and is not an observable. Therefore, to find the amount of charge transferred among atoms, a definition of atom based on charge density is required. Richard

Bader proposed a model named "Atoms in Molecules" (AIM) [28] to estimate the space of an individual atom by a 2D zero flux surface on which the charge density is a minimum perpendicular to this surface. These regions are called Bader volumes. The mathematical condition to be satisfied is:

$$\nabla n(r).n(r) = 0 \qquad (2.77)$$

$\hat{n}(r)$ is the unit vector of the 2D surface and $\nabla n(\vec{r})$ gives the gradient vector field of charge density Through an iterative procedure the product of $\nabla n(\vec{r})$ and $n\hat{}(\vec{r})$ are calculated until the gradient of the produced trajectory satisfies the above condition. Bader's method not only provides [29] a tool to visualize atoms in molecules, it also gives information on the transferred charge or multipole moments of interacting atoms. The total charge of each atom is estimated in Bader volume. In recent years, an algorithm has been developed by Henkelman *et al* [29] which implements Bader analysis in DFT calculations. This algorithm uses a grid-based calculation to obtain total charge of an atom. To achieve accurate results a fine grid should be used to avoid cusps at core region and provide correct number of valence electrons

2.11 Time-Dependent Density Functional Theory (TDDFT)

Accurate theoretical description of the optical properties of materials, especially semiconductors, is very important. From the practical side, these properties define the ability to absorb and emit light and many other features of the systems. Additionally, one needs to properly explain spectroscopic and other optical experimental data used to analyze the optical properties of

materials. These properties are defined to a large degree by the excited states in the system, thus, it is very important to correctly describe the optical absorption spectrum that includes all possible types of excitations in order to understand the properties of the existing and predict the properties of new materials. The standard modern ab initio tool to study excitations in finite systems and solids is TDDFT [30] , an effective theory of charge density, in which all effects of electron-electron interactions and, hence all nontrivial excitations are described by the XC potential. Unfortunately, in the case of solids, standard TDDFT XC potentials, like adiabatic LDA and GGA, do not give excitonic peaks in the absorption spectrum, or give such peaks with extremely small binding energies (see, e.g., [31-33]). Therefore, until very recent times the studies of excitons in semiconductors were almost universally based on a combined *ab initio*+many body approach, in which the GW calculations of the single-particle electronic structure were succeeded by calculations of the two-particle spectrum (that may include excitonic peaks) by solving the Bethe-Salpeter equation (BSE). This BSE approach [34-36]recommended itself as a reliable tool after being tested on many systems, though one also meets with difficulties when using it: large computational times, especially in the case of complex systems, not always well-adjusted approximations for the vertex function in solving the BS equation, etc. Thus, it would be very desirable to develop TDDFT XC potentials for excitons. Indeed, TDDFT is free from both shortcomings mentioned above—it is computationally much less expensive and is, in some sense, "exact", i.e., one does not need to make any approximation for the XC potential. Since excitons can be considered within linear response theory, to study these excitations one basically needs only the linear part of the XC potential defined by the XC kernel.

2.11.1 Charge Susceptibility, Absorption Spectrum and Excitons

Excitons are very often identified as isolated peaks below the conduction band edge in the experimentally observed absorption spectrum. The last function can be calculated from the result for the charge susceptibility. In this section, we give details of the general scheme on how to calculate charge susceptibility within many-body theory and TDDFT and how to obtain the absorption spectrum using these functions. More details on this can be found, for example, in Ref [37].

2.11.2 Many-Body Susceptibility

To calculate the charge susceptibility, let us begin with the formulation of general problem of linear response. In a perturbed system, one can separate the time-dependent charge density into the static (initial) and the perturbed (fluctuating) parts

$$n(\vec{r},t) = n_0(\vec{r}) + n_1(\vec{r},t). \qquad (2.78)$$

The space- and time-dependencies of the fluctuating part of the charge density $n_1(\vec{r},t)$ are defined by the external potential:

$$v(\vec{r},t) = v_0(\vec{r}) + v_1(\vec{r},t)\theta(t-t_0), \qquad (2.79)$$

where the first and the second parts are the static (including the ion) and the time-dependent (turned on at time t_0) parts of the potential, respectively. The second term also defines the interaction part of the many-body Hamiltonian operator in the Heisenberg representation:

$$\hat{H}_1(t) = \int d^3r' v_1(\vec{r}',t)\hat{n}(\vec{r}'), \qquad (2.80)$$

where $\hat{n}(\vec{r}')$ is the charge-density operator (here and below, the subscript 1 stands for the first-order, or linear, approximation). Part (2.80) of the total Hamiltonian $\hat{H}(t) = \hat{H}_0 + \hat{H}_1(t)$ defines the effects of the perturbation on the system ($\hat{H}_0$ is the Hamitonian of the unperturbed system). In order to find the charge susceptibility (and, hence, as we show below, the absorption spectrum), one does not need to solve the general nonequilibrium problem with the total, and usually a rather complicated, Hamiltonian $\hat{H}(t)$. As an alternative, one can calculate the susceptibility within the linear-response approximation by finding first the eigenenergies Ω_n and eigenfunctions Ψ_n from the solution of the static Schrödinger equation with the Hamiltonian $\hat{H}_0$. Ω_n and Ψ_n define the charge susceptibility, or the retarded density-density response function:

$$\chi_{nn}(\vec{r}, \vec{r}', t - t') = -i\theta(t - t')\langle\Psi_0|[\hat{n}(\vec{r}, t - t'), \hat{n}(\vec{r}', 0)]|\Psi_0\rangle \qquad (2.81)$$

(where $[\ldots, \ldots]$ is the commutator of the density operators. The last function in frequency representation:

$$\chi_{nn}(\vec{r}, \vec{r}', \omega) = -i\int_{-\infty}^{\infty} d\tau\theta(\tau)\langle\Psi_0|[\hat{n}(\vec{r}, \tau), \hat{n}(\vec{r}', 0)]|\Psi_0\rangle e^{i\omega\tau} \qquad (2.82)$$

allows one to calculate the absorption spectrum (see Section 2.11.5).

In the linear-response approximation, the expression for the susceptibility also defines the density fluctuation as functional of the external potential

$$n_1(\vec{r}, t) = \int_{-\infty}^{\infty} dt' \int d^3r'\chi_{nn}(\vec{r}, \vec{r}', t - t')v_1(\vec{r}', t'), \qquad (2.83)$$

i.e., Equations (2.81) and (2.82) completely define the excitation spectrum and the spatio-temporal charge dynamics.

To find the explicit frequency-dependent expression for the susceptibility (from Equation (2.82)), one can insert the sum of the product of eigenvectors $\sum_{n=0}^{\infty}|\Psi_n\rangle\langle\Psi_n|$ (equal one) between the density operators in Equation (2.82), and then use the interaction representation for the density operators: $\hat{n}(\vec{r},\tau) = e^{i\hat{H}_0\tau}\hat{n}(\vec{r})e^{-i\hat{H}_0\tau}$ ($\hat{n}(\vec{r})$ on the right-hand side is time-independent), and use the fact that $e^{-i\hat{H}_0\tau}|\Psi_n\rangle = e^{-i\Omega_n\tau}|\Psi_n\rangle$. This gives:

$$\chi_{nn}(\vec{r},\vec{r}',\omega) = \sum_{n=0}^{\infty}\left(\frac{\langle\Psi_0|\hat{n}\,(\vec{r})|\Psi_n\rangle\langle\Psi_n|\hat{n}(\vec{r}')|\Psi_0\rangle}{\omega-\Omega_n+\Omega_0+i\eta} - \frac{\langle\Psi_0|\hat{n}(\vec{r}')|\Psi_n\rangle\langle\Psi_n|\hat{n}(\vec{r})|\Psi_0\rangle}{\omega+\Omega_n-\Omega_0+i\eta}\right) \quad (2.84)$$

The last result can be also used to calculate the frequency-dependent fluctuating charge density from the frequency transform of Equation (2.83):

$$n_1(\vec{r},\omega) = \int d^3r'\chi_{nn}(\vec{r},\vec{r}',\omega)v_1(\vec{r}',\omega). \quad (2.85)$$

To summarize, knowledge of the eigenenergies and eigenfunctions of the unperturbed system allows one to calculate the charge susceptibility from Equation (2.84), which gives the excitation and absorption spectrum, including the excitonic peaks, and in general to obtain the linear-response charge dynamics from Equation (2.83) or Equation (2.85).

2.11.3 TDDFT Susceptibility

In TDDFT, the many-body problem is mapped on an effective problem of one electron in an "external" Kohn-Sham (KS) potential:

$$v_{KS}[n](\vec{r},t) = v(\vec{r},t) + \int d^3r'\frac{n(\vec{r}',t)}{|\vec{r}-\vec{r}'|} + v_{XC}[n](\vec{r},t), \quad (2.86)$$

which is in general a non-linear functional of the charge density (the first, the second and the last terms on the right-hand side are the external, Hartree and the XC potentials, correspondingly). To

find the linear-response TDDFT susceptibility, one can begin with substituting the linear (in external field and density) part of the KS "perturbing" potential $v_{KS1}(\vec{r}', t')$ into the linear-response TDDFT analogue of the many-body Equation (2.83):

$$n_1(\vec{r}, t) = \int dt' \int d^3r' \chi_{KS}(\vec{r}, t, \vec{r}', t') v_{KS1}(\vec{r}', t'), \quad (2.87)$$

where:

$$\chi_{KS}(\vec{r}, t, \vec{r}', t') = \frac{\delta n[v_{KS}](\vec{r}, t)}{\delta v_{KS}(\vec{r}', t')}_{| v_{KS}=v_{KS}[n_0](\vec{r})} \quad (2.88)$$

is the KS susceptibility. The explicit expression for the linear KS XC potential is:

$$v_{KS1}[n](\vec{r}, t) = v_1(\vec{r}, t) + \int d^3r' \frac{n_1(\vec{r}', t)}{|\vec{r} - \vec{r}'|} + v_{XC1}[n](\vec{r}, t), \quad (2.89)$$

The only nontrivial (XC) part of the KS potential can be written as:

$$v_{XC1}[n](\vec{r}, t) = \int dt' \int d^3r' f_{XC}(\vec{r}, t, \vec{r}', t') n_1(\vec{r}', t') \quad (2.90)$$

where:

$$f_{XC}(\vec{r}, t, \vec{r}', t') = \left(\frac{\delta v_{XC}[n](\vec{r}, t)}{\delta n(\vec{r}', t')}\right)_{n_0(\vec{r})} \quad (2.91)$$

is the XC kernel, the key component of the TDDFT theory for excitons.

As the next step of the derivation of the equation for the susceptibility, one can substitute Equation (2.90) into Equation (2.89), and then Equation (2.89) into Equation (2.87), which gives:

$$n_1(\vec{r}, t) = \int dt' \int d^3r' \chi_{KS}(\vec{r}, t, \vec{r}', t') \left[v_1(\vec{r}', t') + \int d\tau \int d^3x \left\{ \frac{\delta(t' - \tau)}{|\vec{r}' - \vec{x}|} + f_{XC}(\vec{r}', t', \vec{x}, \tau) \right\} n_1(\vec{x}, \tau) \right] \quad (2.92)$$

Expressing the linear charge density in the last equation in terms of the susceptibility Equation (2.83) gives the TDDFT equation for the charge susceptibility in terms of the KS susceptibility and the XC kernel:

$$\chi_{nn}(\vec{r},t,\vec{r}',t') = \chi_{KS}(\vec{r},t,\vec{r}',t') + \int d\tau \int d^3x \int_{-\infty}^{\infty} d\tau' \int d^3x' \chi_{KS}(\vec{r},t,\vec{x},\tau)\left\{\frac{\delta(\tau-\tau')}{|\vec{x}-\vec{x}'|} + f_{XC}(\vec{x},\tau,\vec{x}',t')\right\}\chi_{nn}(\vec{x}',\tau',\vec{r}',t'). \quad (2.93)$$

The KS susceptibility can be obtained from the static DFT results for the KS eigenfunctions $\varphi_i^0(\vec{r})$ and eigenenergies E_i as:

$$\chi_{KS}(\vec{r},\vec{r}',\omega) = \sum_{j,k=1}^{\infty}(f_k - f_j)\frac{\varphi_j^0(\vec{r})\varphi_k^{0*}(\vec{r})\varphi_j^{0*}(\vec{r}')\varphi_k^0(\vec{r}')}{\omega - E_j + E_k + i\eta}, \quad (2.94)$$

where E_F is the Fermi- or the highest-occupied molecular orbital energy and $f_j = \theta(E_F - E_j)$ are the state occupancies (see [38] for the details of the derivation of the last equation).

Equation (2.93) can be also written in the frequency domain:

$$\chi_{nn}(\vec{r},\vec{r}',\omega) = \chi_{KS}(\vec{r},\vec{r}',\omega) + \int d^3x \int d^3x' \chi_{KS}(\vec{r},\vec{x},\omega)\left\{\frac{1}{|\vec{x}-\vec{x}'|} + f_{XC}(\vec{x},\vec{x}',\omega)\right\}\chi_{nn}(\vec{x}',\vec{r}',\omega) \quad (2.95)$$

Then, inverting Equation (2.95) one may obtain the XC kernel in terms of the KS and total susceptibilities:

$$f_{XC}(\vec{r},\vec{r}',\omega) = \chi_{KS}^{-1}(\vec{r},\vec{r}',\omega) - \chi_{nn}^{-1}(\vec{r},\vec{r}',\omega) - \frac{1}{|\vec{r}-\vec{r}'|}. \quad (2.96)$$

Thus, one can calculate the charge susceptibility from Equation (2.93) by using the static DFT result for the KS susceptibility (from Equation (2.94)) and the TDDFT XC kernel. Provided the

XC kernel has the proper form, one can obtain the exciton peaks in the absorption spectrum obtained from the susceptibility, as shown in section 2.11.5.

2.11.4 Susceptibility: Finite vs. Extended (Periodic) Systems

The results obtained in the last two Subsections are valid in the general cases of finite systems and infinite non-periodic systems. In this subsection, we present the corresponding formula for the TDDFT susceptibility for periodic systems. In the last case, the problem is simplified, since one needs the KS eigenfunctions in the primitive cell only and the eigenvalues (band energies) are defined by the momenta in only one, the first, Brillouin zone.

Indeed, due to translation invariance of the response function:

$$\chi(\vec{r},\vec{r}',\omega)=\chi\left(\vec{r}+\vec{R},\vec{r}'+\vec{R},\omega\right) \qquad (2.97)$$

($\vec{R}$ are lattice vectors) and of the other functions, like $\chi_{KS}(\vec{r},\vec{r}',\omega)$, $f_{XC}(\vec{r},\vec{r}',\omega)$ and the Coulomb potential $\frac{1}{|\vec{r}-\vec{r}'|}$, one can express them as Fourier sums:

$$\chi(\vec{r},\vec{r}',\omega)=\frac{1}{V}\sum_{\vec{k}}\sum_{\vec{G},\vec{G}'}e^{-i(\vec{k}+\vec{G})\vec{r}}\chi\left(\vec{k}+\vec{G},\vec{k}+\vec{G}',\omega\right)e^{i(\vec{k}+\vec{G}')\vec{r}'} \qquad (2.98)$$

(and similar for $\chi_{KS}(\vec{r},\vec{r}',\omega)$ and $f_{XC}(\vec{r},\vec{r}',\omega)$) and:

$$\frac{1}{|\vec{r}-\vec{r}'|}=\frac{1}{V}\sum_{\vec{k}}\sum_{\vec{G},\vec{G}'}e^{-i(\vec{k}+\vec{G})\vec{r}}\delta_{\vec{G},\vec{G}'}\frac{4\pi}{|\vec{k}+\vec{G}|^2}e^{i(\vec{k}+\vec{G}')\vec{r}'}, \qquad (2.99)$$

where $\vec{G}$ and $\vec{G}'$ are the reciprocal vectors. To simplify the expressions for the functions in the sums in the last equations, we introduce the definitions:

$$\chi_{\vec{G}\vec{G}'}\left(\vec{k},\omega\right)=\chi\left(\vec{k}+\vec{G},\vec{k}+\vec{G}',\omega\right), \qquad (2.100)$$

$$v_{\vec{G}}(\vec{k}) = \frac{4\pi}{|\vec{k}+\vec{G}|^2} \qquad (2.101)$$

Substituting Equations (2.98)–(2.101) into Equation (2.95) gives the (reciprocal vector) matrix equation for the charge susceptibility:

$$\chi_{\vec{G}\vec{G}'}(\vec{k},\omega) = \chi_{KS\vec{G}\vec{G}'}(\vec{k},\omega) + \sum_{\vec{G}_1,\vec{G}_2} \chi_{KS\vec{G}\vec{G}_1}(\vec{k},\omega)\left\{v_{\vec{G}_1}(\vec{k},\omega)\delta_{\vec{G}_1\vec{G}_2} + f_{XC\vec{G}_1\vec{G}_2}(\vec{k},\omega)\right\}\chi_{\vec{G}_2\vec{G}'}(\vec{k},\omega), \qquad (2.102)$$

where the frequency-dependent KS matrix susceptibility is defined as:

$$\chi_{KS\vec{G}\vec{G}'}(\vec{k},\omega) = \frac{1}{V}\sum_{\vec{k}'}\sum_{j,l=1}^{\infty} \frac{\left(f_{l\vec{k}+\vec{k}'} - f_{j\vec{k}'}\right)}{\omega+\varepsilon_{j\vec{k}'}-\varepsilon_{l\vec{k}+\vec{k}'}+i\eta} \int d^3r \varphi^{0*}_{j\vec{k}'}(\vec{r}) e^{-i(\vec{k}+\vec{G})\vec{r}} \varphi^{0}_{l\vec{k}+\vec{k}'}(\vec{r}) \times$$

$$\int d^3r' \varphi^{0*}_{l\vec{k}+\vec{k}'}(\vec{r}') e^{i(\vec{k}+\vec{G}')\vec{r}'} \varphi^{0}_{j\vec{k}'}(\vec{r}'), \qquad (2.103)$$

and j, l are the band indices (for derivation of the last expression, see, for example, [37])

The solution of the matrix Equation (2.102) for $\chi_{\vec{G}\vec{G}'}(\vec{k},\omega)$ (in practice, the equation is solved with a finite number of the reciprocal vectors that defines the rank of the matrices) basically consists of matrix inversion, and can be written as:

$$\chi_{\vec{G}_1\vec{G}_2} = \sum_{\vec{G}_3} (A^{-1})_{\vec{G}_1\vec{G}_3} \chi^0_{\vec{G}_3\vec{G}_2}, \qquad (2.104)$$

where:

$$A_{\vec{G}_1\vec{G}_3} = \delta_{\vec{G}_1\vec{G}_3} - \sum_{\vec{G}_4} \chi^0_{\vec{G}_1\vec{G}_4} f_{HXC\vec{G}_4\vec{G}_3}, \qquad (2.105)$$

and:

$$f_{HXC\vec{G}_4\vec{G}_3} = v_{\vec{G}_4}\delta_{\vec{G}_4\vec{G}_3} + f_{XC\vec{G}_4\vec{G}_3} \qquad (2.106)$$

(we have omitted the momentum and frequency indices $(\vec{k}, \omega)$, which are the same for each function and matrix in Equations (2.104)–(2.106)). The required number of the required reciprocal vectors is needed to be checked separately for each problem.

In the next subsection, we present details how one can obtain the absorption spectrum by using the susceptibilities from Equations (2.84), (2.95), and (2.104).

2.11.5 Absorption Spectrum

The absorption spectrum can be obtained by calculating the imaginary part of the macroscopic dielectric function $\epsilon_{\mathrm{mac}}(\omega)$ that can be found by space-averaging the dielectric function $\epsilon(\vec{r}, \vec{r}', \omega)$. The last function relates to the charge (optical) susceptibility from the previous subsections as:

$$\epsilon(\vec{r}, \vec{r}', \omega) = 1 + 4\pi\chi(\vec{r}, \vec{r}', \omega). \quad (2.107)$$

In order to perform the macroscopic averaging of the last function, one can use the equation that connects the microscopic electric induction and the electric field by means of the dielectric function:

$$\vec{D}(\vec{r}, \omega) = \int d^3r' \epsilon(\vec{r}, \vec{r}', \omega)\vec{E}(\vec{r}', \omega), \quad (2.108)$$

which, in the case of a periodic system, can be transformed to:

$$\vec{D}_{\vec{G}}(\vec{k}, \omega) = \sum_{\vec{G}'} \epsilon_{\vec{G}\vec{G}'}(\vec{k}, \omega)\vec{E}_{\vec{G}'}(\vec{k}, \omega). \quad (2.109)$$

Averaging of the last equation over the unit cell gives the scalar relation between the macroscopic quantities:

$$\vec{D}_{\mathrm{mac}}(\omega) = \epsilon_{\mathrm{mac}}(\omega)\vec{E}_{\mathrm{mac}}(\omega). \quad (2.110)$$

In the homogeneous case, when $\epsilon(\vec{r},\vec{r}',\omega)=\epsilon(\vec{r}-\vec{r}',\omega)$, the dielectric function $\epsilon(\vec{r},\vec{r}',\omega)$ depends on the difference of two spatial vectors and its Fourier transform $\epsilon_{\vec{G}\vec{G}'}(\vec{k},\omega)$ is diagonal in the reciprocal vector indices. In this case, the average of $\epsilon(\vec{r},\vec{r}',\omega)$ can be easily obtained by integrating over $(\vec{r}-\vec{r}')$, which gives:

$$\epsilon_{\text{mac}}^{\text{hom}}(\omega)=\epsilon^{\text{hom}}(\vec{q}\to 0,\omega). \qquad (2.111)$$

In the general, non-homogeneous, case due to local-field effects (spatial fluctuations), the situation is more complicated since $\epsilon_{\vec{G}\vec{G}'}(\vec{k},\omega)$ is a non-diagonal matrix. In particular, in the case of cubic systems, to calculate $\epsilon_{\text{mac}}(\omega)$, one needs to perform the matrix inversion (see, e.g., [39])

$$\epsilon_{\text{mac}}(\omega)=\left[\epsilon^{-1}_{\vec{G}\vec{G}'}(\vec{k}\to 0,\omega)|_{\vec{G}=0,\vec{G}'=0}\right]^{-1}. \qquad (2.112)$$

In order to connect $\epsilon^{-1}_{\vec{G}\vec{G}'}(\vec{k}\to 0,\omega)$ with the charge susceptibility matrix, one can write, in analogy with Equation (2.110), the equation:

$$v_1(\vec{r},\omega)=\int \mathrm{d}^3r'\epsilon(\vec{r},\vec{r}',\omega)\left[v_1(\vec{r}',\omega)+\int d^3r''\frac{n_1(\vec{r}'',\omega)}{|\vec{r}'-\vec{r}''|}\right], \qquad (2.113)$$

Using Equation (2.83) gives:

$$\epsilon^{-1}(\vec{r},\vec{r}',\omega)=\delta(\vec{r}-\vec{r}')+\int d^3r''\frac{\chi(\vec{r}'',\vec{r}',\omega)}{|\vec{r}-\vec{r}''|}. \qquad (2.114)$$

In the periodic case, the last equation can be transformed to:

$$\epsilon^{-1}_{\vec{G}\vec{G}'}(\vec{k},\omega)=\delta_{\vec{G}\vec{G}'}+\mathrm{v}_{\vec{G}}(\vec{k})\chi_{\vec{G}\vec{G}'}(\vec{k},\omega). \qquad (2.115)$$

One can show from the last equation that the macroscopic dielectric function is:

$$\epsilon_{\text{mac}}(\omega)=1-\mathrm{v}_0(\vec{k}\to 0)\bar{\chi}_{00}(\vec{k}\to 0,\omega), \qquad (2.116)$$

where $\bar{\chi}_{\vec{G}\vec{G}'}(\vec{k},\omega)$ is calculated from Equation (2.102) with:

$$v_{\vec{G}}(\vec{k}) = \begin{cases} 0, \vec{G} = 0 \\ \frac{4\pi}{|\vec{k}+\vec{G}|^2}, \vec{G} \neq 0 \end{cases} \quad (2.117)$$

(for details of the derivation of Equation (2.115) and references, we refer the reader to Appendix M of [37])

2.11.6 TDDFT and Excitons: The Density-Matrix Approach

To begin, the discussion on studies of excitons with "pure" TDDFT, we present the DM formulation of this theory [32,33,40], which is one of the most convenient schemes for the practical applications. To derive the DM-TDDFT equation for the exciton binding energy, one can begin with the KS equation:

$$i\frac{\partial \Psi_k^v(r,t)}{\partial t} = H(r,t)\Psi_k^v(r,t), \quad (2.118)$$

where k is the wave vector, v is the valence-band index, and the KS Hamiltonian is:

$$H(r,t) = -\frac{\nabla^2}{2m} + V_H[n](r,t) + V_{XC}[n](r,t) + erE(t). \quad (2.119)$$

In the last equation, the terms on the right-hand side are the kinetic (first), Hartree (second), and XC (third) potentials, and an external homogeneous electric field (the last term). Equation (2.118) has to be solved self-consistently with the equation for the electron density:

$$n(r,t) = \sum_{l,|k|<k_F} \left|\Psi_k^l(r,t)\right|^2 \quad (2.120)$$

where l are the occupied band indices. In the DM representation, Equations (2.118) and (2.119) are solved by expanding the KS wave function in the basis of the static DFT wave functions $\varphi_k^{0l}(r)$:

$$\Psi_k^v(r,t) = \sum_l c_k^{vl}(t)\varphi_k^{0l}(r). \quad (2.121)$$

The time-dependent coefficients $c_{\mathbf{k}}^{vl}(t)$ completely describe the system dynamics. Below we drop index v for sake of simplicity, since we will consider the case of one valence band. The coefficients $c_{\mathbf{k}}^{l}(t)$ can be found from the following equation:

$$i\frac{\partial c_k^m}{\partial t} = \sum_l H_{kk}^{ml} c_k^l, \qquad (2.122)$$

where:

$$H_{kq}^{lm}(t) = \int \varphi_k^{0l*}(r) H[n](r,t) \varphi_q^{0m}(r) dr. \qquad (2.123)$$

However, to study the system response it is more convenient to consider the bilinear combination of c-coefficients, the density matrix:

$$\rho_{kq}^{lm}(t) = c_k^l(t) c_q^{m*}(t). \qquad (2.124)$$

Its diagonal elements describe the level occupancies, while the non-diagonal ones—the electron transitions, including the excitonic effects. The matrix elements satisfy the Liouville equation:

$$i\frac{\partial \rho_{kq}^{lm}(t)}{\partial t} = [H(t), \rho(t)]_{kq}^{lm}. \qquad (2.125)$$

In the case of two (valence *v* and conduction *c*) bands, one can derive the exciton TDDFT equation for the non-diagonal element $\rho_{kq}^{cv}(t)$ by using Equations (2.119), (2.120), (2.123), and (2.125). Expansion of the charge density fluctuations in Equation (2.125), in terms of the density matrix elements (Equation (2.124)) (by using Equation (2.120)), leads to the TDDFT Wannier equation [33]:

$$\left[\left(\varepsilon_{k+q}^{c} - \varepsilon_k^{v}\right)\delta_{kk'} + F_{kkk'k'}^{cvvc}\right]\rho_{n,k'+\alpha q}^{cv}(\omega) = E_{n,q}\,\rho_{n,k+\alpha q}^{cv}, \qquad (2.126)$$

where $\boldsymbol{q}$ is the exciton momentum, α is the reduced hole mass, and n is the bound state number. The effective electron-hole interaction is described by the last term in the brackets defined as:

$$F^{abcd}_{kqk'q'}(\omega) = \int dr_1 dr_2 \varphi^{0a*}_{k}(r_1)\varphi^{0b}_{q}(r_1) f_{XC}(r_1, r_2, \omega)\varphi^{0c*}_{k'}(r_2)\varphi^{0d}_{q'}(r_2). \quad (2.127)$$

One can obtain the excitonic binding energies from Equation (2.126) by setting q = 0. We have generalized the above formalism for the case of higher excitations—trions and biexcitons [40]. One can derive equations for these quasi-particles similar to Equation (2.126) by expanding the corresponding wave functions in terms of three (trion) and four (bi-exciton) KS wave functions with the coefficients that include the corresponding polarization matrix elements. The solution of the equation for this element will give the binding energy for the trion and biexciton. In addition to the e-h attraction terms of type (2.126), and the equation will also include the e-e and h-h repulsion terms with the interaction matrix elements:

$$w^{cdab}_{k_1k_2p_1p_2} = \frac{1}{\varepsilon_{ee}} \int dr_1 dr_2 \, \varphi^{0c*}_{k_1}(r_1)\varphi^{0d*}_{k_2}(r_2) \frac{1}{|r_1 - r_2|} \varphi^{0a}_{p_1}(r_1)\varphi^{0b}_{p_2}(r_2) \quad (2.128)$$

(ε_{ee} is static e-e screening; for details, see [40])

In the following subsection 2.11.7 I present an overview of the long range (LR) kernal to study excitons with TDDFT. To calculate the excitonic energy one can proceed in three ways:

(1) to calculate the dielectric function with a given fxc, as described in section 2.11.1. Then, the excitonic binding energies will be identified as peaks in the absorption spectrum.

(2) to propagate in time the KS equation, with consequent frequency transformation of the polarization matrix element which also defines the absorption spectrum that might include excitonic peaks.

(3) to solve the linearized Equation (2.126) for the excitonic binding energies.

The first and the third approaches correspond to the linear response (where the XC kernel is used), while the second might be regarded as a more general, since the time-propagation of the KS equation can be performed for any non-linear XC potential.

Below, we describe the LR-XC kernel which we will use to calculate the excitonic binding energies with Approach 3.

2.11.7 LR XC Kernel

Indeed, taking into account effects of LR interaction improves significantly the situation, the binding energies are often of order of the experimentally observed values. The simplest LR kernel is the kernel with the same name:

$$f_{XC}^{LR}(r, r') = -\frac{1}{\varepsilon}\frac{1}{|r-r'|}, \qquad (2.129)$$

where ε is the effective scattering parameter (dielectric function).

More systematically one can construct an XC kernel that considers the effects of the LR interaction by using an energy functional that includes such effects. A natural choice for such a functional is the exact exchange (EXX) energy:

$$E_X^{exact}\left[\varphi^{(0)}\right] = -\frac{1}{2}\sum_{\sigma,i,j}\int d^3r \int d^3r' \frac{\varphi_{i\sigma}^{0*}(r')\varphi_{j\sigma}^{0}(r')\varphi_{i\sigma}^{0}(r)\varphi_{j\sigma}^{0*}(r)}{|r-r'|}, \qquad (2.130)$$

where σ is the spin variable and i and j are other quantum numbers that correspond to given state. Since the corresponding XC potential (OEP [41,42]) and the kernel depend on the set of orbitals, to obtain the XC potential one needs to perform the functional differentiation of the energy (Equation (2.130)) by using the chain rule, which can be symbolically written as

$v^0_{XC\sigma}(r) = \frac{\delta E^{exact}_{XC}[\varphi^{(0)}]}{\delta n_\sigma(r)} = \frac{\delta E^{exact}_{XC}[\varphi^{(0)}]}{\delta \varphi^0_{j\sigma'}(r')}\frac{\delta \varphi^0_{j\sigma'}(r')}{\delta n_\sigma(r)} + \frac{\delta E^{exact}_{XC}[\varphi^{(0)}]}{\delta \varphi^{0*}_{j\sigma'}(r')}\frac{\delta \varphi^{0*}_{j\sigma'}(r')}{\delta n_\sigma(r)}$. Performing the differentiation and applying some other transformations in the resulting equation will lead to the following equation for $v^0_{XC\sigma}(r)$:

$$\sum_{\sigma,i,j}\int d^3r'\left[v^0_{XC\sigma}(r') - \Upsilon^0_{Xj\sigma}(r')\right]\varphi^0_{i\sigma}(r)\varphi^{0*}_{i\sigma}(r')\sum_{k\neq j}\frac{\varphi^0_{k\sigma}(r')\varphi^{0*}_{k\sigma}(r)}{\varepsilon_{j\sigma}-\varepsilon_{k\sigma}} + c.c. = 0, \quad (2.131)$$

where:

$$\Upsilon^0_{Xj\sigma}(r) = \frac{1}{\varphi^{0*}_{j\sigma}(r)}\frac{\delta E^{exact}_{XC}[\varphi^{(0)}]}{\delta \varphi^0_{j\sigma}(r)}. \quad (2.132)$$

The fist summation in Equation (2.131) is performed over the occupied states, while the last one—over all states. Since one cannot invert Equation (2.131) in order to obtain the explicit analytical expression for the XP potential (though the exact potential can be obtained numerically[43]), to get a feeling of the main features of the OEP potential one needs to transform the equation to a more convenient form by doing some approximations. The simplest one, the so called KLI approximation [44], is based on approximating the energy differences in this equation by the effective average value $\varepsilon_{j\sigma} - \varepsilon_{k\sigma} = \Delta\varepsilon$. In this case, the equation is significantly simplified:

$$v^{KLI}_{XC\sigma}(r) = \frac{1}{2n_\sigma(r)}\sum_{\sigma,i,j} n_{j\sigma}(r)\left[\Upsilon^0_{Xj\sigma}(r) + \left(\bar{v}^{KLI}_{Xj\sigma} - \bar{\Upsilon}^0_{Xj\sigma}\right)\right] + c.c., \quad (2.133)$$

with:

$$\bar{v}^{KLI}_{Xj\sigma} = \int d^3r \varphi^{0*}_{j\sigma}(r) v^{KLI}_{Xj\sigma}(r)\varphi^0_{i\sigma}(r). \quad (2.134)$$

While it is much easier to solve the KLI (Equation (2.133)) than the general OEP (Equation (2.131)), in practice some additional approximations in the KLI equation are often used. One of

them is to neglect the spatially-independent term under the integral $\left(\bar{v}_{XCj\sigma}^{KLI} - \overline{\Upsilon}_{XCj\sigma}^{0}\right)$, which gives the Slater XC potential:

$$v_{XC\sigma}^{Slater}(r) = \frac{1}{2n_{\sigma}(r)} \sum_{\sigma,i,j} n_{j\sigma}(r) \left[\Upsilon_{XCj\sigma}^{0}(r) + \Upsilon_{XCj\sigma}^{0*}(r)\right], \quad (2.135)$$

Further simplification is the approximation of the orbital charge density in the denominator of the last expression by the average value, which gives the global averaging method (GAM) XC potential:

$$v_{XC\sigma}^{GAM}(r) = \frac{1}{2N_{\sigma}} \sum_{\sigma,i,j} n_{j\sigma}(r) \left[\Upsilon_{XCj\sigma}^{0}(r) + \Upsilon_{XCj\sigma}^{0*}(r)\right]. \quad (2.136)$$

Using the differentiation chain rule in Equations (81), (83), and (84) as above, one can obtain the expressions for the KLI, Slater, and GAM XC kernels, correspondingly (actually, in the KLI case—the equation for the kernel). We present here the expressions for the Slater kernel:

$$f_{XC\sigma}^{Slater}(r) = -\frac{2\left|\sum_{j,\sigma} \varphi_{j\sigma}^{0}(r) \varphi_{j\sigma}^{0*}(r')\right|}{|r-r'| n_0(r) n_0(r')}. \quad (2.137)$$

As it follows from the results above, the three kernels contain the Coulomb singularity, which results in a rather good description of the exciton energies even in the GAM case.

CHAPTER 3: LINEAR TRANSITION METAL-DIPYRIDYLTETRAZINE CHAINS WITH ACTIVE METAL SITE

Creation, stabilization, characterization, and control of single atom transition metal (TM) sites may lead to significant advancement of the next-generation catalyst. We have performed density functional theory-based calculations of TM-dipyridyltetrazine (DT) chains in which TM atoms are stabilized and separated by the DT molecules. We found two types of geometries of TM-DT chains (planar and non-planar). Our calculations show that the formation energies of the chains are high (~2.0 to 7.9 eV), suggesting that these chains can be stabilized. Moreover, by calculating the adsorption energies of CO, and O_2 on the metal atom sites of the chains with planar configuration, we found that these molecules/atoms strongly bond to TM atoms Mo, Cr, Fe, V and Co occupying these sites, suggesting that these TM-DT chains are potential candidates for CO oxidation catalyst. Other chains with Au, Ag, Cu, and Ni form a non-planar structure. The adsorption energies of CO and O_2 on these metal centers with planar geometry, ranges from 1.0 to 4.0 eV. The O_2 molecule undergoes dissociation while adoption on V center and causes strong distortion to V-DT chain. We investigated the oxidation state of these metal centers using core level shift. For Pt and V, the calculated +2 oxidation state is consistent with the experimentally reported value.

3.1 Introduction

The conventional metal catalysts (nanoparticles or bulks) offer an abundance of active metal sites, with many different coordination numbers, using them in a controlled and well-ordered fashion for catalysis is challenging job. Recent theoretical and experimental studies have shown that sub nanometer-sized metal clusters can sometimes show better catalytic activity or selectivity than the

nanometer-sized particles [45-51]. The size effect on catalytic performance can be seen in chemically inert gold: upon downsizing bulk gold to nanoparticles or even to sub nanoclusters gold exhibits extraordinary catalytic performance in many heterogeneous reactions [45,52]. But although sub nanoclusters even smaller in size as compared to bulk still contain multiple active centers, they do not always afford the particular activity desirable for specific catalytic processes. The search for catalysts with well-defined and ordered single active centers is crucial both for understanding catalytic mechanisms and for improving the catalytic performance [53]. To make use of each metal atom, the most effective way is to downsize the metal particles and distribute their centers in a well-ordered array. Such is the ultimate goal of fine dispersion [54-57]. Single metal atoms on support surfaces provide a good opportunity to tune active sites and optimize the activity, selectivity, and stability of heterogeneous catalysts, offering the potential for applications in a variety of industrial chemical reactions [5]. B. Qiao *et. al.* synthesized and characterized a catalyst that consists of single Pt atoms uniformly dispersed on a high surface area of FeOx support . This catalyst showed extremely high activity for both CO oxidation and PROX reactions. The chemical reactivity of single Pt atoms is quite different from that of single Au atoms or cations on the same support [45,58,59]. The use of metal−organic complexes in surface catalysts is therefore of interest for creating well-defined and highly regular single-site centers [60]. Single-sites in many systems also show higher selectivity than typical heterogeneous catalysts [53]. The technique for forming systematically distributed discrete single-sites is to exploit on-surface metal–ligand coordination to produce metal–organic networks (MON) on a solid surface. The uniformity of single sites thus produced is of prime interest for designers of catalysts [53,61-64]. Recent experimental study has showen that creation and stabilization of well-defined single metal

site Pt (II) within tetrazine coordinated chains on Au (100) surface is possible [63]. The authors have also demonstrated that these redox-assembled chains are stable to 150 C°. Moreover, these chains may be used as model systems for exploring the coordination chemistry of single-site transition metals that hold potential for future applications in tandem catalysts [63]. However, it has been shown that Pt-centered chains are *not* chemically active [65]. The question that naturally arose is: might there be *other* TM centers that could form stable structures in coordination with DT, which would be more reactive than Pt-centers in Pt-DT chain structure?

As this chapter describes, We have screened many different transition metal atoms coordinated with DT using first-principles density functional theory (DFT), to check their propensity to serve as active sites for the adsorption of several molecules and atoms of interest. I first present the equilibrium structure of TM-DT chains. To check if the metal centers are chemically active in these TM-DT chains I then calculate the adsorption energies of molecules like CO, O_2 at the metal site of TM-DT chain. I am then able to address the following questions: Do any transition metals other than Pt [63] form sufficiently stable configuration? Do these metal centers play a role in surface reactions?

3.2 Calculation Details and Model System

We performed Ab initio calculations based on density functional theory (DFT) with the plane-wave and pseudopotential method implemented in the Quantum Espresso package [66]. The exchange and correlation energy and potential were calculated with the Perdew–Burke–Ernzerhof (PBE) parameterization [15] of the generalized gradient approximation (GGA). The electron wave function was expanded in a plane-wave basis set cut-off 60 Ry. A 3×1×1 Monckhorst–Pack grid

[22] was used for the k-points. A vacuum slab of 15 Å was used in the direction normal to the plane of TM-DT chain to ensure the absence of interlayer interactions in that direction. optB86b-vdW [67] functional are used to compare the adsorption energy values. The optB86b-vdW functional is a modified version of the vdW-DF [19], with an empirically optimized B86b-like exchange functional. Atomic charges were evaluated using the Bader analysis [29].

The model system is shown schematically in Figure 3.1. Each unit cell is composed of two metal centers (both are V, Cr, Mo, Fe, Co, Ni, Pd, Pt, Cu, Ag and Au) and two DT molecules. To get the equilibrium metal-metal (M-M) separation, we relaxed the system with various value of M-M separations to obtain formation energy as function of M-M separation, from which a third order polynomial fitting is used to determine the equilibrium separation. Here, formation energy (E_f) is defined as

$$E_f = \frac{1}{2}\{E_t - 2 \times (E_{mol} + E_{metal})\} \quad (3.1)$$

where E_t is the total energy in of the TM-DT chain, and E_{mol} and E_{metal}, are the energies of DT molecule, and metal atom, respectively.

For calculations of adsorption energies of CO and O_2 on metal site of TM-DT chain we have chosen the systems with planar geometrical configuration. Adsorption energy is defined as,

$$E_{ads} = E_{MOC+mol} - E_{MOC} - E_{mol} \quad (3.2)$$

Here $E_{MOC+mol}$, E_{MOC} and E_{mol} are the total energies of TM-DT chain with the adsorbed molecule, the isolated TM-DT chain and the isolated gas molecule (CO and O_2), respectively. The negative values of E_{ads} represent exothermic reaction which are favorable as the activation energy

barrier for these reactions to take place is smaller as compared to the endothermic reactions for reaction rates

To identify the chemical state of TM centers, we have performed the calculations by shifting one electron from the core level of each TM center to fermi level, and compare the shifted value of binding energy of core level with respect to the binding energy of core level in bulk of each TM center.

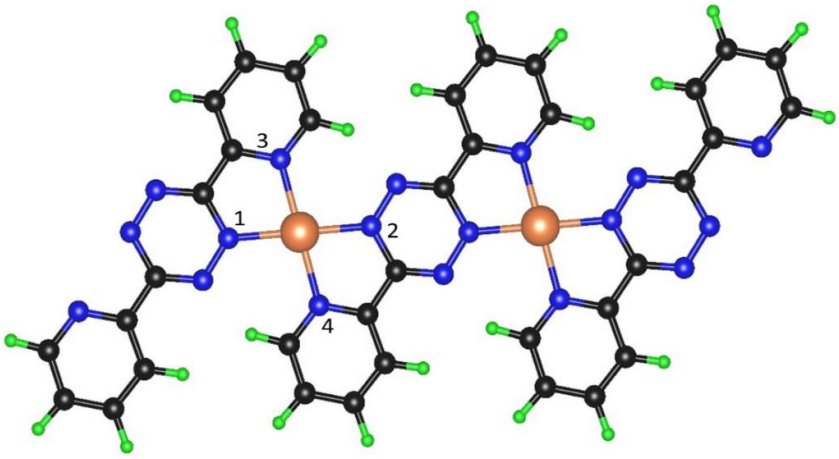

Figure 3.1: Schematic representation of TM-DT chain, used in the calculations. Large gold balls represent metal atom, black, blue, and green balls represent C, N and H atoms, respectively. The numbers 1-4 assigned to N atoms coordinated with metal atom are for reference.

3.3 Results and Discussions

3.3.1 Formation of TM-DT chains

Table 3.1 summarizes formation energies, magnetic phase, and geometry of all studied TM-DT chains under consideration. Note here that we have carried out DFT calculations in ferromagnetic (FM), antiferromagnetic (AFM) and non-magnetic (NM) state which enables us to determine the lowest energy configuration. For NM state, calculations were performed without considering spin

polarization, for FM state we assign parallel spin to both the metal centers with in the cell, while for AFM state we assign anti-parallel spin to the metal centers (spin up for first metal center and spin down for second metal center). For each chain we have considered these three magnetic configurations, and found that Mo-, Cr-DT chains in FM state has lowest energy, while V-DT chain has lowest energy in AFM state. All other TM-DT chains has lowest energy in NM state. By analyzing the geometries, we found that systems with low formation energies like Au, Ag, Cu and Ni form non-planar distorted structure, while systems having higher values of formation energies like Co, Cr, Fe, Mo, Pd, Pt and V form planar structure. Note that we have simulated all these system in gas phase.

In Figure 3.2 we showed the dependence of formation energy on the number of valence electron of metal centers. The TM with fully occupied *d*-orbital form non-planar structure like Au, Ag and Cu, while the TM with partially occupied *d*-orbital like Co, Cr, Fe, Mo, Pd, Pt and V form square planar structure. However, Ni with 8 electrons in the 3*d* state form a non-planar structure. We are interested in stable chain with planar structures for catalyst applications, thus we further investigate only planar chains. Here after we will discuss the properties of planar chains only.

Table 3.2 lists Bader charges of TM-DT, the Bader charge on each TM atom and the neighboring N atoms of the DT chain, show that TM atoms were oxidized, and the DT ligands are reduced. The occupancies of *d*-sub levels of metal atoms in TM-DT chain configuration is shown in Table 3.3. These occupancies are calculated by integrating the projection of total density of states on the *d*-orbitals of the metal atoms. The complete and partial occupancies of *d* orbitals of metal atoms dictate the favorability of adsorption of gas molecules like CO and O_2. By analyzing the binding energy shift of core level, we found that the core level 2*p* of V has shifted 0.66, which corresponds

to +2 oxidation states of V consistent with the experimental value [68,69]. the core level 4*f* of Pt has shifted 2.64 eV corresponds +2 oxidation state of Pt in Pt-DT chain consistent with the theoretical and experimentally reported value.[63,65].

Table 3.1: List of metal centers, the equilibrium Metal-Metal separation in units of Å, formation energies per ½ cell calculated in electron volts (eV), magnetic ground states and equilibrium geometrical structure.

Metal	M-M distance	Formation energy	Magnetic state	Structure
Au	6.824	-2.824	NM	Non-planar
Ag	7.127	-2.573	NM	Non-planar
Co	6.617	-6.899	NM	Planar
Cr	6.809	-5.589	FM	Planar
Cu	6.764	-4.138	NM	Non-planar
Fe	6.649	-6.132	NM	Planar
Mo	6.984	-6.127	FM	Planar
Ni	6.626	-6.059	NM	Non-planar
Pd	6.799	-4.842	NM	Planar
Pt	6.784	-6.761	NM	Planar
V	6.848	-7.996	AFM	Planar

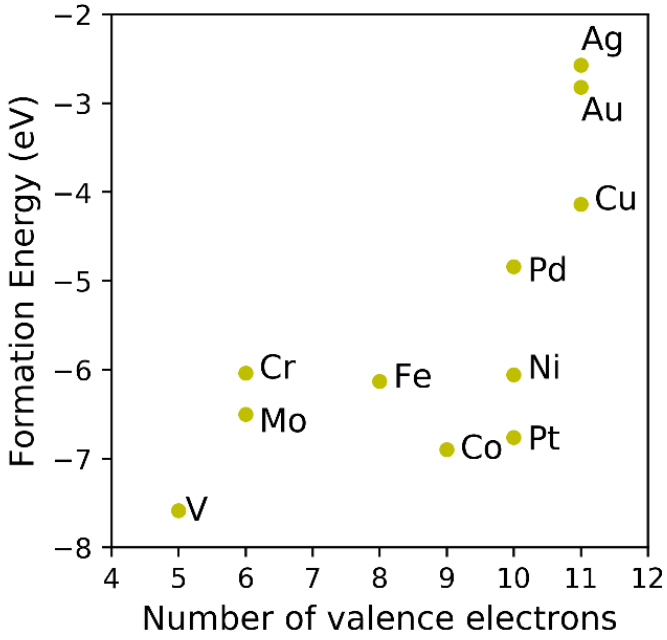

Figure 3.2: Formation Energies of Metal-Organic Chains in units of eV/ (1/2) cell, plotted against number of valence electrons of metal atoms.

Table 3.2: Bader charges on TM atoms and the neighboring N atoms of DT chain coordinated with metal center, electron lose is represented by negative sign and gain is represented by positive sign

Metal Center	Charge Lose (e)	N1	N2	N3	N4
Mo	-1.24	+0.36	+0.36	+0.23	+0.23
Cr	-1.22	+0.36	+0.36	+0.22	+0.22
Fe	-0.96	+0.29	+0.29	+0.14	+0.14
Co	-0.87	+0.25	+0.25	+0.16	+0.16
Pd	-0.66	+0.19	+0.19	+0.12	+0.12
Pt	-0.72	+0.22	+0.22	+0.11	+0.11
V	-1.18	+0.38	+0.38	+0.23	+0.23

Table 3.3: Occupancies of *d*-sub levels of metal centers in TM-DT chain

M	d_{z^2}	$d_{x^2-y^2}$	d_{zx}	d_{zy}	d_{xy}
Mo	0.94	0.70	0.99	1.00	0.94
V	0.88	0.55	0.47	0.74	0.92
Cr	0.95	0.62	0.98	0.97	0.95
Fe	1.76	0.75	1.11	1.54	1.80
Co	1.83	0.81	1.50	1.70	1.83
Pd	1.89	1.12	1.89	1.94	1.86
Pt	1.81	1.03	1.84	1.90	1.84

3.3.2 Adsorption of O_2 on TM centers

The calculated values of adsorption energies of O_2 on different metal center are shown in Figure 3.3. A higher (absolute) values of adsorption energy corresponds to a stronger bonding of adsorbed molecule with TM site.

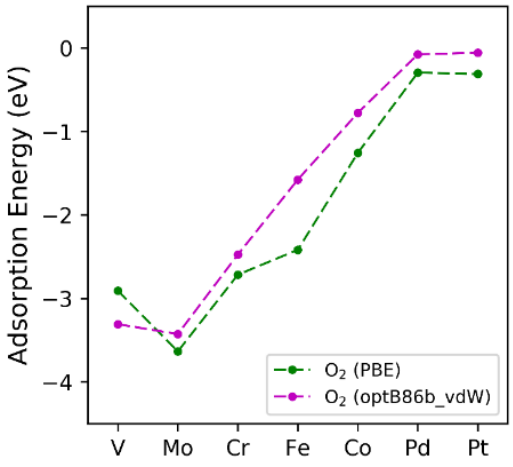

Figure 3.3: Adsorption Energies (Eads) of O_2 adsorbed on TM site of TM-chain

We analyzed the frontier orbitals of metal atoms and found that all the *d*-orbitals of Pd and Pt are completely occupied (Figure 3.13). The calculated adsorption energy of O_2 on Pd and Pt is less than 100 meV. The chain structure remains planar after O_2 adsorption, while the O_2 molecule resides on top of Pd and Pt well beyond the Pd-, Pt-O bond length. Figure 3.4 shows schematically the adsorption of O_2 on Pd, Pt site. The Pd-, Pt-O separation is 3.49, 3.76 Å respectively. In the Figure 3.4 b ,c we have also plotted the charge density difference, which shows that there is no hybridization taking place between the *d*-orbitals of metal center and the p-orbitals of O_2 molecule. Thus, we can conclude that these two metal centers are not chemically active for O_2 molecule, thus Pd-, PT-DT chains are not suitable candidates to be used as a catalyst for O_2 reduction-reaction.

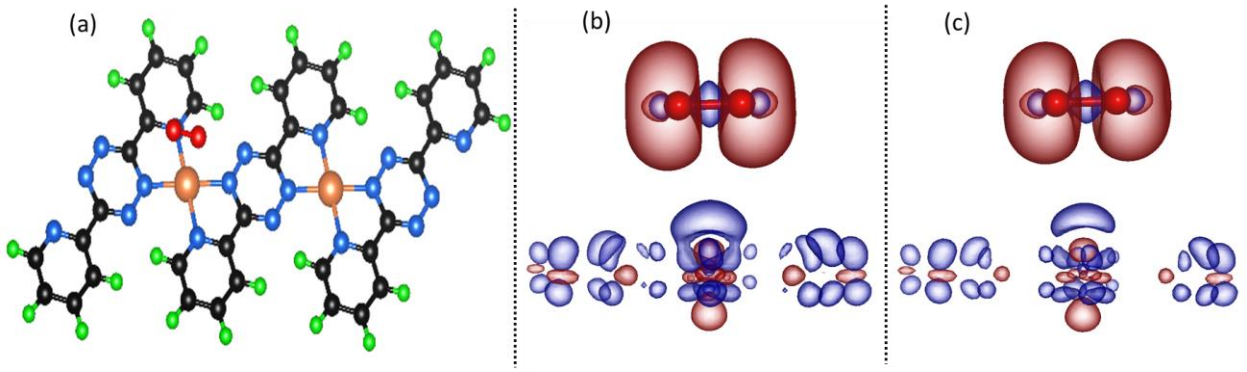

Figure 3.4: Schematic representation of (a) O_2 adsorption on Pd-, Pt-DT chain. Large gold balls represent Pd, Pt atom, black, blue, green, and green balls represent C, N, H and O atoms, respectively. The charge density difference (b) O_2-Pd-DT and (c) O_2-Pt-DT plot showing no chemical bond formation between Pd, Pt and O atoms. Red and blue iso-surfaces indicate electron accumulation and depletion regions, respectively. The iso-surface value is 0.001 e/Å^3.

The calculated absolute value of adsorption energy of O_2, 0.779 and 1.578 eV on Co and Fe site respectively. The charge density difference plot that these TM centers are making a chemical bond with O_2 molecule. In Figure 3.5 we plot schematically the preferred orientation of O_2 adsorption on Co and Fe site, the charge density difference plot shows that one of the O makes bond with the

metal center with relaxed Co-O bond length 1.89 Å and Fe-O 1.79 Å while Co-O-O and Fe-O-O angles are 117.8°, 121.3° respectively. The Adsorption of O_2 causes a small out of plane displacement ~ 0.12 Å to Co atom, while this out of plane displacement is ~ 0.47 Å to Fe atom. This out of plane displacement of metal center eliminates the planarity of chain.

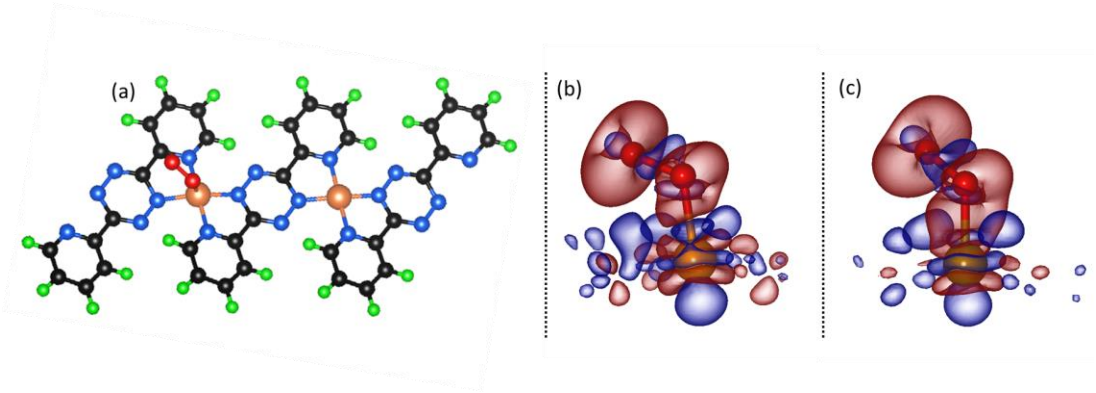

Figure 3.5: Schematic representation of (a) O_2 adsorption on Co-, Fe-DT chain. Large gold balls represent Co, Fe atom, black, blue, green, and red balls represent C, N, H and O atoms, respectively. The charge density difference (b) O_2-Co-DT and (c) O_2-Fe-DT plot showing chemical bond formation between Co, Fe and O atoms. Red and blue iso-surfaces indicate electron accumulation and depletion regions, respectively. The iso-surface value is 0.002 e/Å^3.

The calculated absolute value of adsorption energy of O_2, 2.476 and 3.428 eV on Cr and Mo site, respectively. We plot the charge density difference in Figure 3.6, which suggest that these TM centers are making a chemical bond with O_2 molecule, Figure 3.6a shows schematically the preferred orientation of O_2 adsorption on Cr and Mo site. The orientation of O_2 in adsorbed phase is parallel to the plane of TM-DT chain, while the orientation of O_2 was tilted out of plane in case of adsorption on Co-, and Fe-DT chain. Adsorption of O_2 causes a large out of plane displacement ~ 0.50 and 0.51 Å to Cr and Mo atoms respectively, thus distorts the planarity of the TM-DT chain.

The relaxed O-O bond length of O_2 molecule in adsorbed phase on Cr and Mo is 1.431 and 1.469 Å respectively. This stretched O-O bond suggest the weakening of O-O bond.

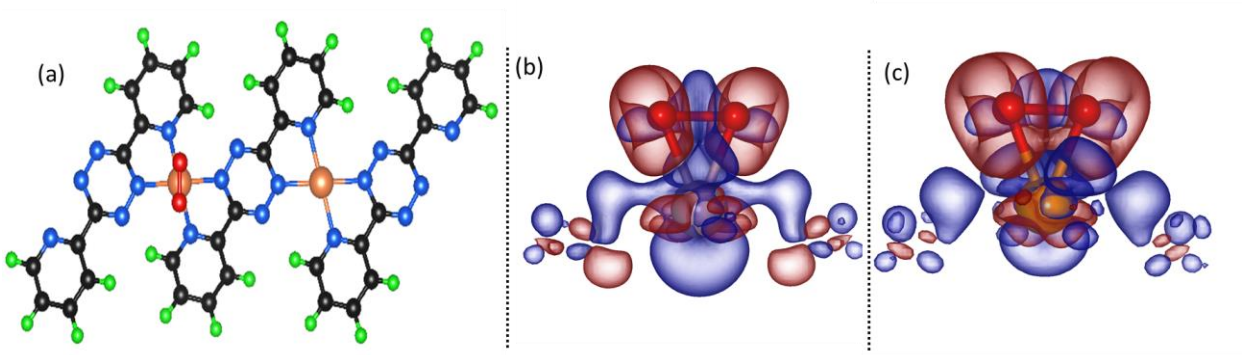

Figure 3.6: Schematic representation of (a) O_2 adsorption on Cr-, Mo-DT chain. Large gold balls represent Cr, Mo atom, black, blue, green, and red balls represent C, N, H and O atoms, respectively. The charge density difference (b) O_2-Cr-DT and (c) O_2-Mo-DT plot showing chemical bond formation between Cr, Mo, and O atoms. Red and blue iso-surfaces indicate electron accumulation and depletion regions, respectively. The iso-surface value is 0.002 e/Å^3.

We found that O_2 adsorption on V center cause structural distortion in the chain, O_2 adsorbs on V as a dissociated form and distorts the planarity of chain.

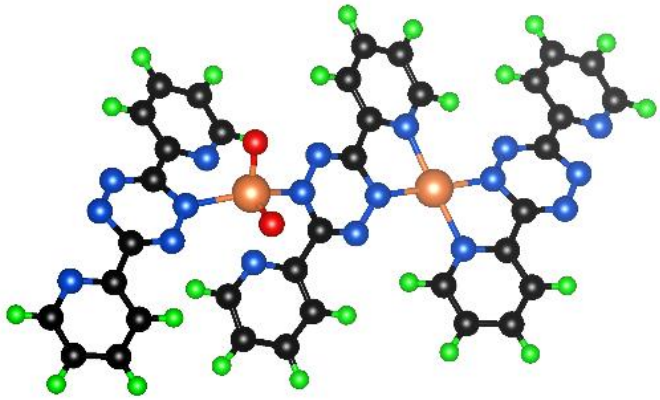

Figure 3.7: Schematic representation of O_2 adsorption on V-DT chain. Large gold balls represent V atoms, black, blue, green, and red balls represent C, N, H and O atoms, respectively.

By analyzing the adsorption of O_2 on metal sites of TM-DT chains we found three types of adsorptions. For Pd- and Pt-DT chains O_2 is physio adsorbed, with no overlapping of orbitals (no hybridization of Pd-, Pt orbitals with the orbitals of O_2) and the TM-O distance is not within the bond length of the Pd-, Pt-O bond length. The absolute value of adsorption energy shows that O_2 is interacting with the metal site weakly. This weak interaction is not affecting the planarity of chain structure. However, there is some charge redistribution occurs at TM site, such that there is depletion of charge at TM site while accumulation of charge at O_2 molecule. This polarity of charge is causing the weak electrostatic attraction between TM center and O_2 molecule. We found that O_2 is making chemical bond with Co and Fe such that O-O is oriented out of TM-DT plane. One of the O is making bond with TM while another O of the O_2 molecule is not interacting directly with the TM center. In case of Cr and Mo center O_2 is making chemical bond with TM center such that both the O atoms of the molecule are interacting with TM-center via hybridized bond. The absolute value of adsorption energy shows strong interaction of the adsorbates with the host system.

3.3.3 Adsorption of CO on TM centers

The calculated adsorption energy of CO on Pd and Pt is 23 and 79 meV respectively. The Pd- and Pt-C distance is 3.186, 3.372 Å respectively.

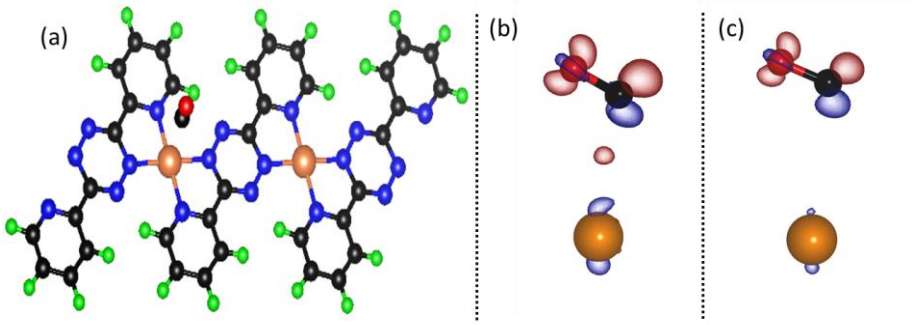

Figure 3.8: Schematic representation of (a) CO adsorption on Pd-, Pt-DT chain. Large gold balls represent Pd, Pt atoms, black, blue, green, and red balls represent C, N, H and O atoms, respectively. The charge density difference (b) CO-Pd-DT and (c) CO-Pt-DT plot showing no chemical bond formation between Pd, Pt and CO molecule. Red and blue iso-surfaces indicate electron accumulation and depletion regions, respectively. The iso-surface value is 0.001 e/Å^3

The calculated adsorption energies of CO on Co and Fe site is 0.946 and 1.719 eV respectively

Figure 3.9 shows schematically the orientation of the adsorbed CO molecule on Co and Fe site of the TM-DT chain. Adsorption of CO causes an out of plane displacement ~ 0.30 Å to both Co and Fe atom, thus distorts the planarity of the TM-DT chain.

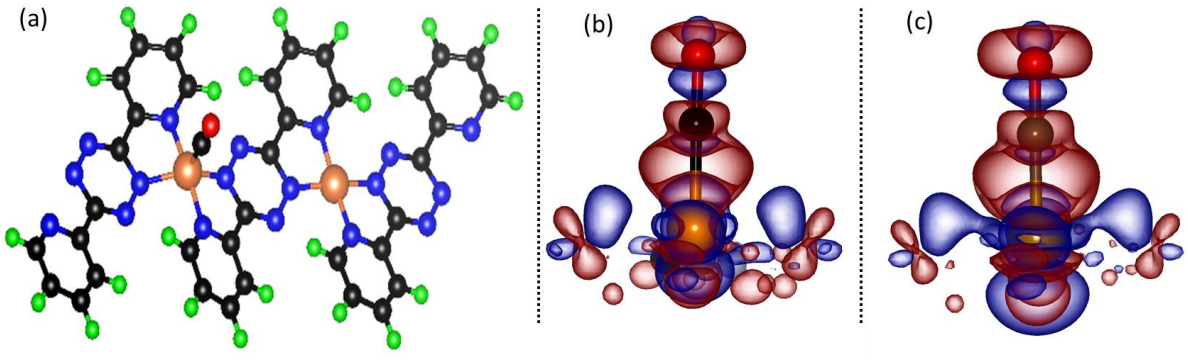

Figure 3.9: Schematic representation of (a) CO adsorption on Co-, Fe-DT chain. Large gold balls represent Co, Fe atom, black, blue, green, and red balls represent C, N, H and O atoms, respectively. The charge density difference (b) CO-Co-DT and (c) CO-Fe-DT plot showing chemical bond formation between Co, Fe and C atom of CO molecule. Red and blue iso-surfaces indicate electron accumulation and depletion regions, respectively. The iso-surface value is 0.002 e/Å^3.

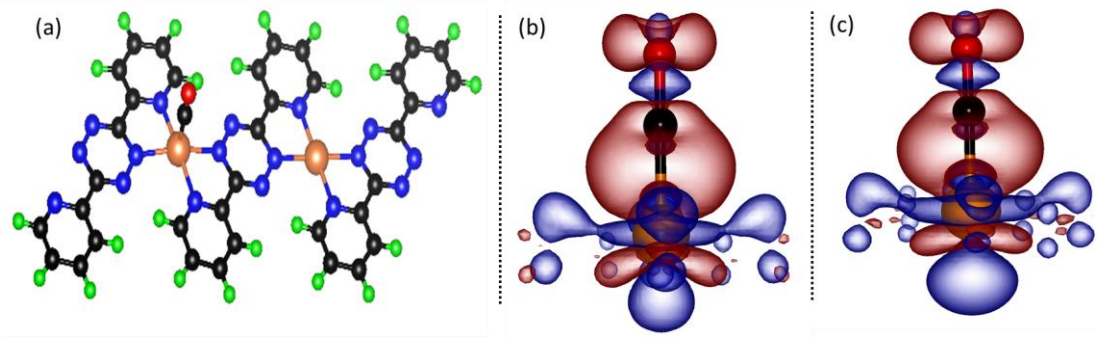

Figure 3.10: Schematic representation of (a) CO adsorption on Cr-, Mo-DT chain. Large gold balls represent Cr, Mo atom, black, blue, green, and red balls represent C, N, H and O atoms, respectively. The charge density difference (b) CO-Cr-DT and (c) CO-Mo-DT plot showing chemical bond formation between Cr, Mo, and C atom of CO molecule. Red and blue iso-surfaces indicate electron accumulation and depletion regions, respectively. The iso-surface value is 0.002 e/Å^3.

The calculated absolute value of adsorption energy of CO, 1.085 and 2.131 eV on Cr and Mo site respectively. Figure 3.10 shows schematically the orientation of the adsorbed CO molecule on Cr and Mo site of the TM-DT chain. Adsorption of CO causes an out of plane displacement ~ 0.29 and 0.31 Å to Cr and Mo atoms respectively, thus distorts the planarity of the TM-DT chain. The calculated absolute value of adsorption energy of CO, 1.38 eV on V site. Figure 3.11 shows schematically the orientation of the adsorbed CO molecule on V site of the V-DT chain. Adsorption of CO causes an out of plane displacement ~ 0.30 Å to V atom, thus distorts the planarity of the V-DT chain.

By analyzing the adsorption of CO on metal sites of TM-DT chains we found two types of adsorptions. For Pd- and Pt-DT chains CO is physio adsorbed, with no chemical bond formation between CO and the TM site, the TM-C distance is not within the bond length of the Pd-, Pt-C

bond length. The absolute value of adsorption energy shows that CO is interacting with the metal sites weakly.

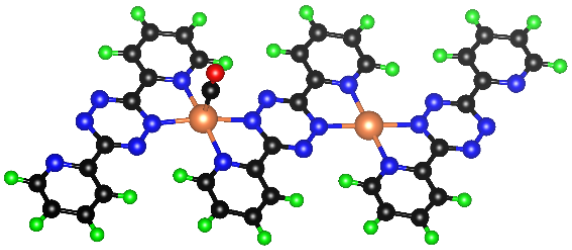

Figure 3.11: Schematic representation of CO adsorption on V-DT chain. Large gold balls represent V atoms, black, blue, green, and red balls represent C, N, H and O atoms, respectively.

Thus TM-DT chain retains its planarity while interacting with CO. We found that CO is making chemical bond with Mo, Cr, Co, and Fe such that CO is oriented out of TM-DT plane. In adsorbed phase of CO on TM site, C is making bond with TM center. The absolute value of adsorption energy shows strong interaction of the adsorbates with the host system.

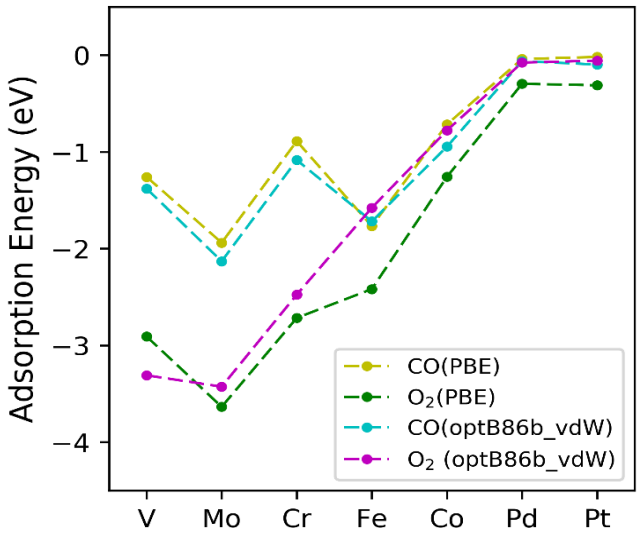

Figure 3.12:Adsorption Energies (Eads) of CO and O_2 adsorbed on different TM site of TM-DT chains. The adsorption energy has been calculated using two different functionals PBE and optB86b.

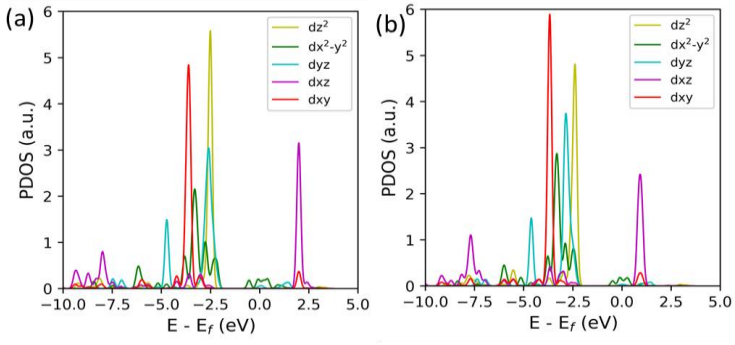

Figure 3.13: Projected density of states (PDOS) of (a) Pt, (b) Pd, d-state. Fermi energy is set at zero.

Before summarizing, the electronic structure of the metal center will be presented. We have presented the PDOS of TM *d*-orbitals, for the cases where TM forms square planar coordination with DT ligands. Figure 3.14 shows the PDOS of Mo *d*-state, and the change in electronic structure after the adsorption of CO and O_2 on Mo site. The *d* state of Mo shows spin polarization. Mo centered TM-DT chain has a magnetic moment of 2.88 μ_B per Mo atom. Due to spin polarization, each *d*-sub level splits into two energy levels for spin up and down states. The gap between these two levels of dz^2 (spin up and down) is ~2.5 eV. When CO is adsorbed on Mo, this gap reduces to ~0.20 eV (See Figure 3.14(b)). The *p* orbital of C is making hybridized bond with *dxz* of Mo. The adsorption of CO suppresses the spin polarization, the magnetic moment after CO adsorption reduces to 1.1 μ_B per Mo atom. The *p* orbitals of O_2 makes bond with *dxy* and *dxz* orbitals of Mo. The magnetic moment of O_2 adsorbed system is 1.9 μ_B per Mo atom.

The PDOS of Cr *d*-state, and the change in electronic structure after the adsorption of CO and O_2 on Cr top side are shown in Figure 3.15 . The *d* state of Cr shows spin polarization. Cr centered TM-DT chain has a magnetic moment of 3.22 μ_B per Cr atom. Due to spin polarization, each *d*-sub level splits into two energy levels for spin up and down states. The gap between these two

levels of dz^2 (spin up and down) is ~2.5 eV. The *p* orbital of C is making hybridized bond with *dxz* of Cr. The adsorption of CO suppresses the spin polarization, the magnetic moment after CO adsorption reduces to 2.37 μ_B per Cr atom. The p orbitals of O_2 on top of Cr makes bond with *dxy* and *dxz*. The magnetic moment of system is 1.97 μ_B per Cr atom.

Figure 3.16-3.17 shows the PDOS of Fe and Co *d*-state, and the change in electronic structure after the adsorption of CO and O_2 on Fe and Co top side. The *p* orbital of C is making hybridized bond with *dxz* and *dxy* of Fe and Co. The *p* orbital of O make bond with *dxz* and *dxy*.

Figure 3.18-3.19, shows the PDOS of Pd and Pt *d*-state, and the change in electronic structure after the adsorption of CO and O_2 on Pd and Pt top side. All the *d* states are buried deep inside the valence band except dx^2-y^2, however there is no significant overlap of states of adsorbates with the *d* states of Pt and Pd. Figure 3.20 shows the PDOS of V *d*-state, and the change in electronic structure after the adsorption of CO and O_2 on V side of V-DT chain. The *p* orbital of C is making hybridized bond with *dyz* of V. The *p* orbital of O make bond with dz^2 and *dxy*.

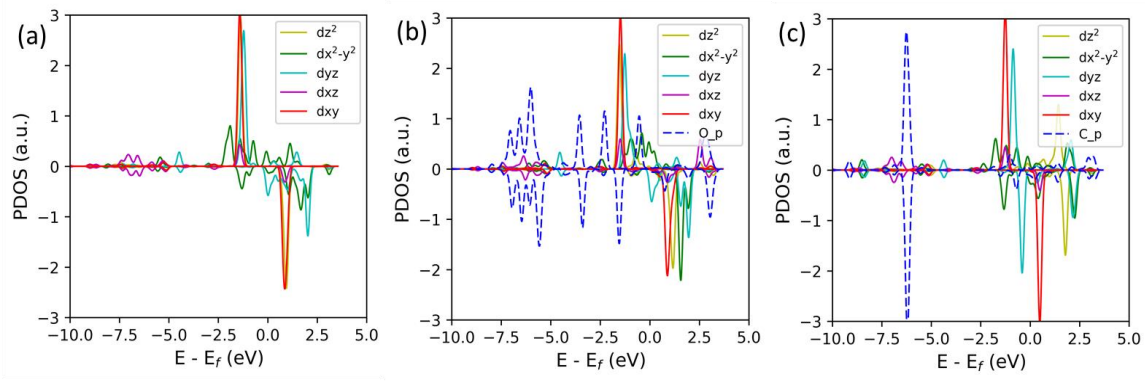

Figure 3.14: Projected density of states (PDOS) of (a) Mo-d state in Mo-DT chain, (b) Mo-d and C-p states in case of CO adsorbed on Mo site of Mo-DT chain and (c) Mo-d and O-p states in case of O_2 adsorbed on Mo site of Mo-DT chain, where blued dashed line represents p-state of C and O respectively. The positive (negative) values of PDOS show spin-up (spin-down) states.

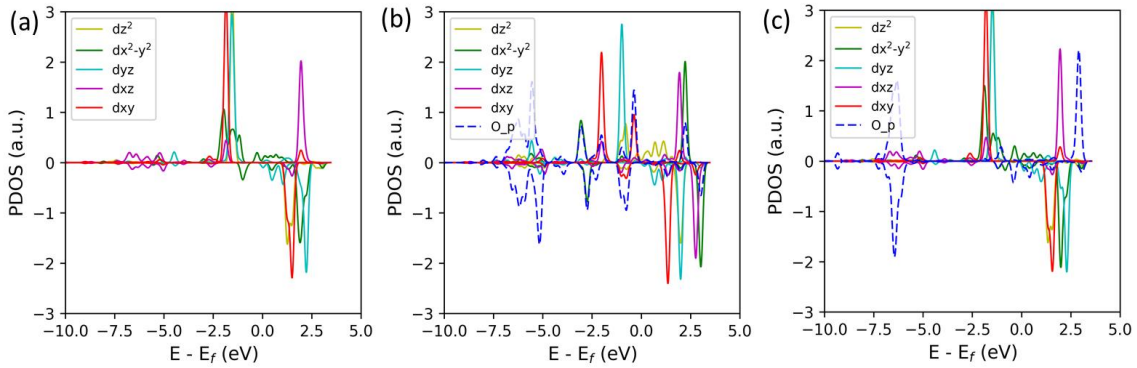

Figure 3.15: Projected density of states (PDOS) of (a) Cr-d state in Cr-DT chain, (b) Cr-d and C-p states in case of CO adsorbed on Cr site of Cr-DT chain and (c) Cr-d and O-p states in case of O_2 adsorbed on Cr site of Cr-DT chain, where blued dashed line represents p-state of C and O respectively. The positive (negative) values of PDOS show spin-up (spin-down) states

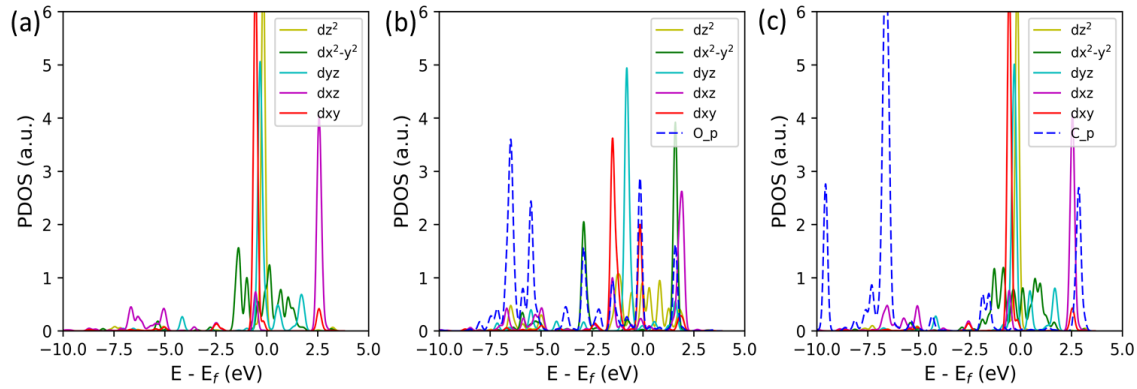

Figure 3.16: Projected density of states (PDOS) of (a) Fe-d state in Fe-DT chain, (b) Fe-d and C-p states in case of CO adsorbed on Fe site of Fe-DT chain and (c) Fe-d and O-p states in case of O2 adsorbed on Fe site of Fe-DT chain, where blued dashed line represents p-state of C and O respectively.

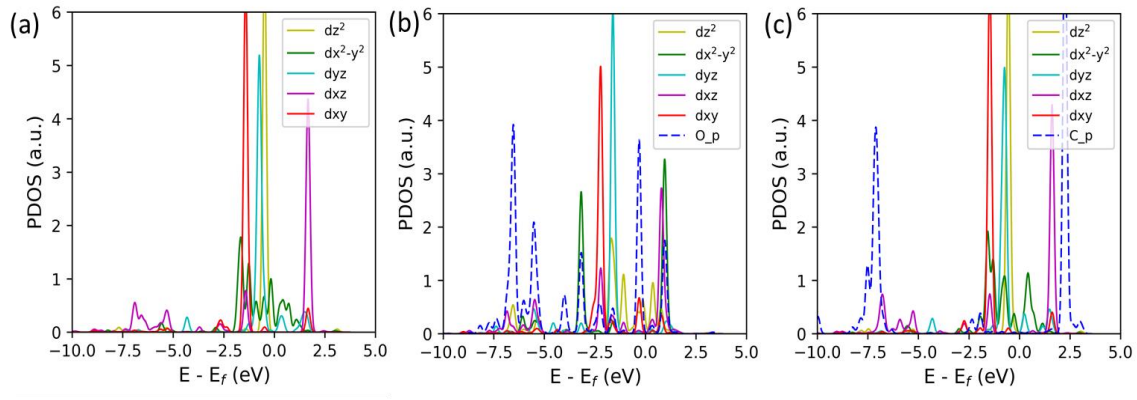

Figure 3.17: Projected density of states (PDOS) of (a) Co-d state in Co-DT chain, (b) Co-d and C-p states in case of CO adsorbed on Co site of Co-DT chain and (c) Co-d and O-p states in case of O_2 adsorbed on Mo site of Co-DT chain, where blued dashed line represents p-state of C and O respectively.

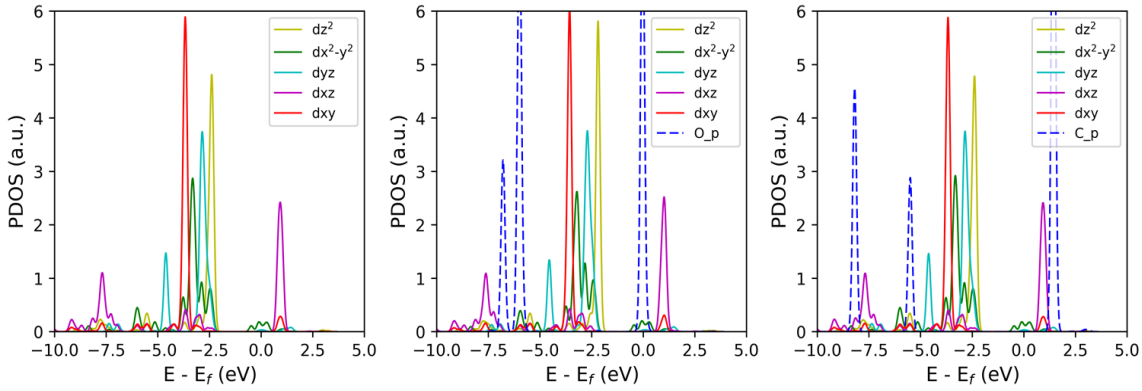

Figure 3.18: Projected density of states (PDOS) of (a) Pd-d state in Pd-DT chain, (b) Pd-d and C-p states in case of CO adsorbed on Pd site of Pd-DT chain and (c) Pd-d and O-p states in case of O_2 adsorbed on Pd site of Pd-DT chain, where blued dashed line represents p-state of C and O respectively.

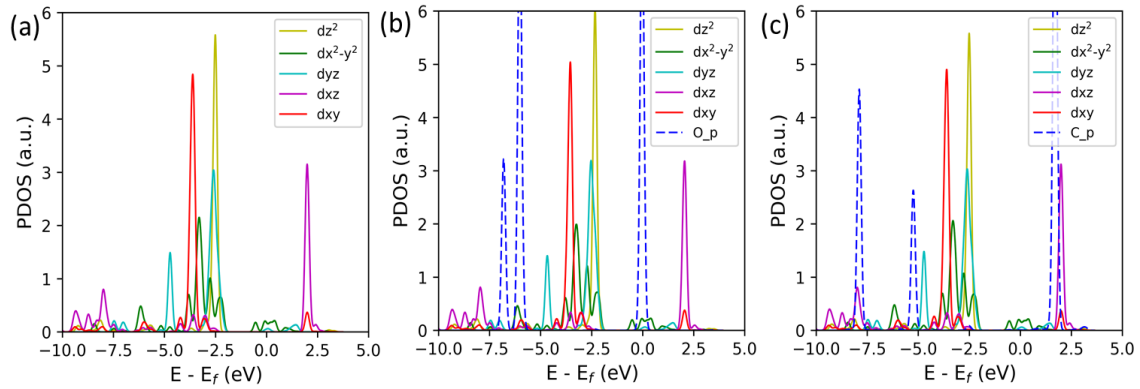

Figure 3.19: Projected density of states (PDOS) of (a) Pt-d state in Pt-DT chain, (b) Pt-d and C-p states in case of CO adsorbed on Pt site of Pt-DT chain and (c) Pt-d and O-p states in case of O_2 adsorbed on Pt site of Pt-DT chain, where blued dashed line represents p-state of C and O respectively.

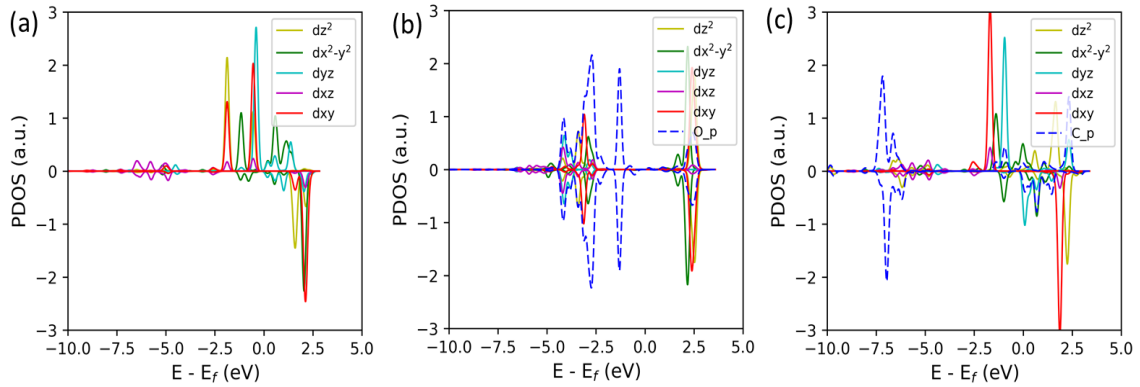

Figure 3.20:Projected density of states (PDOS) of (a) V-d state in V-DT chain, (b) V-d and C-p states in case of CO adsorbed on V site of V-DT chain and (c) V-d and O-p states in case of O_2 adsorbed on V site of V-DT chain, where blued dashed line represents p-state of C and O respectively

3.4 Discussion

Since the outer shells of Pd and Pt atom are complete, so no chemical adsorption of O_2 and CO occurs on top of these two metal centers. The weak interaction of adsorbates (O_2 and CO) with Pd-, Pt-DT chain is not affecting the chain structure, thus the Pd-, Pt-DT chain retain retains its

planarity. Figure 3.12 shows the comparison of calculated adsorption energies of O_2 and CO on each metal center. The Pd-, Pt-DT though forms chain structure with high formation energies, Pt-DT chains are stable even at higher temperatures [22] are not chemically active. This chemical inertness toward O_2 and CO molecule as discussed above suggest that these types of TM-DT chains are not candidate material to be used as catalyst for CO oxidation reaction. The Co-, Fe-DT chains show strong affinity toward O_2 and CO molecule. The binding energies of O_2 and CO is comparable on both Co and Fe sites, thus these types of TM-DT chains are good candidates for CO oxidation reaction. The Cr-, Mo-DT chains show strong affinity toward both O_2 and CO molecules, however the adsorption energy difference of O_2 and CO molecule on these metal centers is greater than 1.0 eV, thus poisoning the active metal site. The O_2 molecule undergoes a dissociative adsorption on V-DT chain. The adsorption energy difference of O_2 and CO on V site of V-DT chain is large enough. Thus V-DT chain is not a good candidate for CO oxidation reaction. However, V-DT chain is undergoing a chemical state change from +2 to +4 while reacting with O_2. For V-DT we have plotted the adsorption energy of O_2 on V site in molecular form. The values of calculated adsorption energies using two different functionals is different, but we can see the adsorption energies exhibit same trend for both used functionals. The key parameter we extract through our electronic structure calculations is the occupancy of *d*-orbital of metal center in TM-DT chain configuration, through which we can tune the chemistry of the TM-DT chains.

3.5 Summary

In summary, we have performed DFT calculations to screen TM-DT linear chains. The higher values of formation energies suggest that these TM-DT chains are stable. We have identified the

chemical states of metal centers in the TM-DT chains. The TM atoms donate charge to DT molecules, making them positively charged, resulting in non-zero oxidation state. The calculated adsorption energies show that both CO and O_2 adsorb strongly (chemical adsorption) on Mo, Cr, Fe, V and Co sites, and weakly (physical adsorption) on Pt and Pd sites. In light of the strong affinity of TM-DT toward O_2 and CO molecule and, the comparable value of adsorption energy of these two molecules in case of Co-, Fe- site, we conclude that Co-, Fe-DT chains can be used as a catalyst for CO oxidation reaction. The V center in V-DT chain is playing a role in reducing O_2.

CHAPTER 4: NON-LINEAR TM-BIS-PYRIMIDINE (BP) CHAINS WITH ACTIVE METAL SITE ON Au(111)

4.1 Introduction

This chapter describes our investigation of the structure and chemical properties of non-planar metal-organic chains. This investigation (which is ongoing) is motivated by the quest to discover how the chemistry of metal center can be tuned by different organic ligands. By using Bis-Pyrimidine (BP) as a linker we have been able to pin down the relationship between the reducing capacity of a given linker and the change in oxidation state of TM center. Analogously with the investigation described in chapter 3, in this chapter we will begin by investigating the structure of TM-BP chains using different TM atoms. After the initial screening of chain formation, magnetic ground state and charge analysis, we choose V-BP as a model system to study the effect of support (Au(111) surface) on structure and charge state of V-BP chain. We have shown that V-DT on Au(100) supports dissociation of molecular oxygen [68]. In this chapter I will be using atomic oxygen as a probe to compare the chemical activity of metal center.

4.2 Computational Method

We performed Spin-polarized density functional theory (DFT) simulations for gas phase V-BP metal-organic networks and for V-BP on the Au(111) surface using the Vienna Ab-initio Simulation Package (VASP) [70] employing the projector-augmented wave (PAW) [27] and plane wave basis set methods. We used DFT-D3 [18] corrections for accounting the van der Waals interactions. The energy cutoff for plane wave expansion was set to 500 eV. The minimum vacuum layer thickness is ~ 15 Å which is large enough to avoid the interaction between

neighboring images. Our simulation supercell for gas phase calculations consists of 2 BP molecules and 2 V atoms corresponding to the M:BP ratio of 1:1. We used 3×1×1 mesh in performing integration over the Brillouin zone for both gas phase as well as on support calculations, which is sufficient for the convergence of formation energy. For the system consisting of the BP ligands and V adatoms on the Au(111) surface, our supercell consists of 2 V atoms, 2 BP ligands, and 5 layer Au(111) slab, all together, we thus have 198 atoms in the supercell. During relaxation, the bottom three Au layers are held fixed at their bulk position. All structures are relaxed until all component acting on each ion reach a threshold of 0.01 eV/Å.

4.3 Results and Discussion

4.3.1 Molecular network formation

The model Bis-pyrimidine (BP) network is shown in Figure 4.1. The network is composed of 3 BP molecules and repeats in x-direction. To compare the reducing capacity of the molecule we used 2,2'-Biimidazole (H2bim) molecule and the H2bim network (Figure 4.2). We calculated the network formation energy using equation

$$E_f = \frac{1}{n}[E_{network} - n \times E_{mol}] \qquad (4.1)$$

$E_{network}$ is the total energy of BP, H2bim network, E_{mol} is the total energy of isolated BP, H2bim molecule in gas phase. The calculated value of formation energy is -0.24 and -1.24 eV respectively for BP and H2bim network. To quantify the charge transfer from molecule/ molecular network to or from Au(111) support, and ligand-support interaction we put these molecules and molecular networks on Au(111) support. We represent the molecules and molecular network on Au(111)

schematically in Figure 4.3 and 4.4. We have calculated the adsorption energy of these systems using the equation

$$E_{ads} = \frac{1}{n}\left[E_{network/Au(111)} - n \times E_{network} - E_{Au(111)}\right] \quad (4.2)$$

Where $E_{network/Au(111)}$ is total energy of BP, H2bim-Au111 system, $E_{network}$ is the total energy of BP, H2bim network in gas phase and $E_{Au(111)}$ is total energy of Au(111) slab. The calculated value of adsorption is -1.53 and -2.31 eV respectively for BP and H2bim/Au(111) complex.

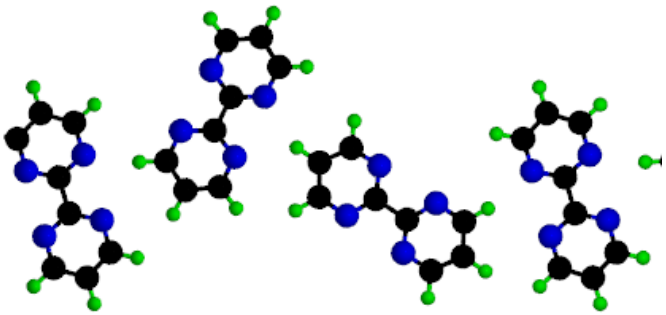

Figure 4.1: Schematic representation of Bis-pyrimidine (BP) network. The blue, black and green color balls represent N, C and H atom, respectively.

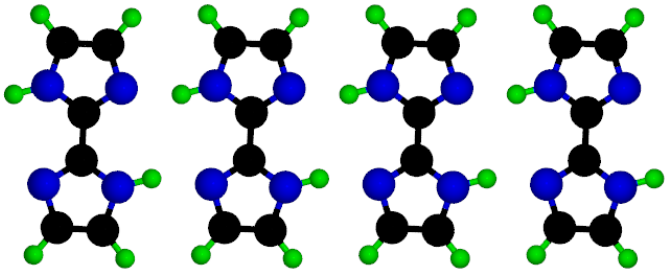

Figure 4.2: Schematic representation of 2,2'-Biimidazole (H2bim) network. The blue, black and green color balls represent N, C and H atom, respectively.

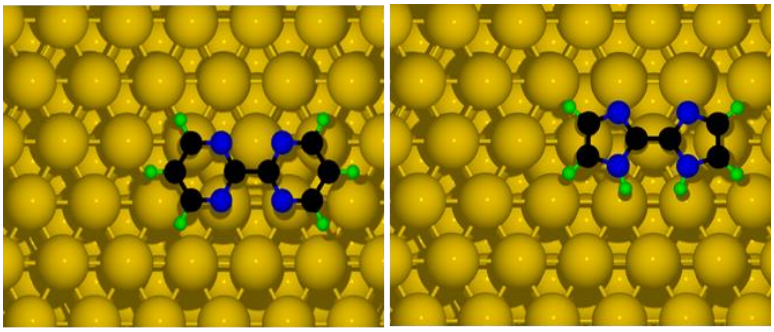

Figure 4.3: Schematic representation of BP molecule (a) and H2bim molecule (b) on Au(111) support. The blue, black, green, and gold color balls represent N, C, H and Au atoms, respectively.

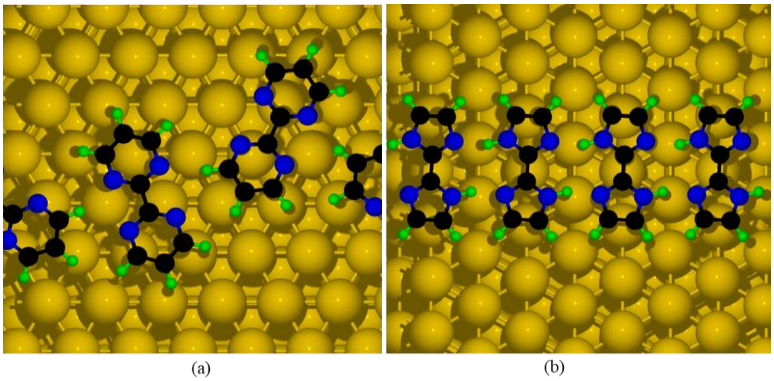

Figure 4.4: Schematic representation of BP network (a) and H2bim network (b) on Au(111) support. The blue, black, green, and gold color balls represent N, C, H and Au atoms, respectively.

The electron density redistribution analysis for bot BP and H2bim molecules on Au(111) is presented in Figure 4.5. The electron density difference is calculated using equation

$$\Delta\rho(z) = \rho_{mol/Au(111)}(z) - \rho_{Au111}(z) - \rho_{mol}(z) \qquad (4.3)$$

Where $\Delta\rho(z)$ is the plane (x, y) averaged electron density difference in the z-direction. $\rho_{mol/Au(111)}(z)$, $\rho_{Au111}(z), \rho_{mol}(z)$ are the plane averaged charge densities for optimized mol-Au(111) complex, Au(111) slab and molecules respectively. Electron density difference fluctuates from nearly zero at 4th layer (from bottom) on Au slab to accumulation region on 5th layer. There

is depletion region in between the molecule and the top of Au(111) slab. On the both BP and H2bim, the electron density difference is mostly -ve meaning that the molecules lose electrons and Au(111) slab gains electron. The charge density difference in case of molecular network (BP and H2bim) on Au(111) Figure 4.6 shows similar pattern of electron density redistribution. Comparison of the magnitude of plane averaged electron density redistribution plots we conclude that either isolated molecules or molecular network on Au(111) H2bim is more reducing as compared to BP.

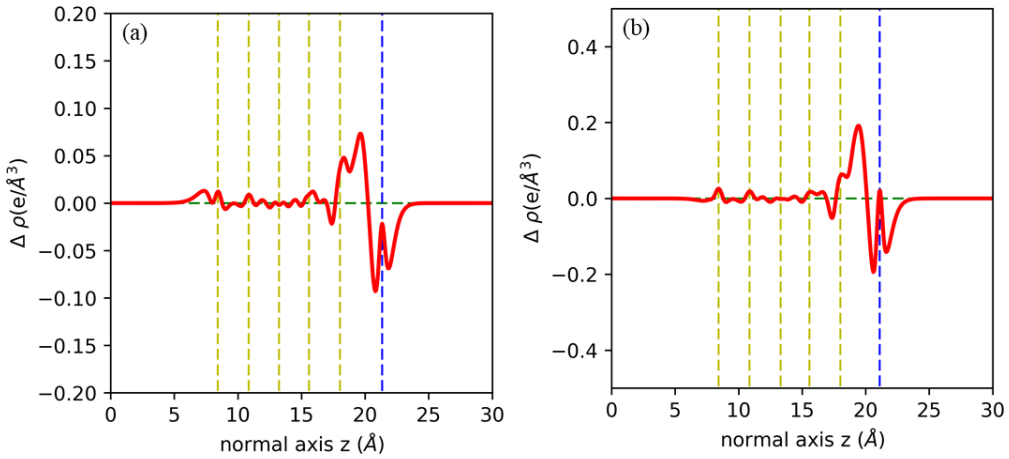

Figure 4.5: Edge-on view (yellow are five planes of Au slab) of plane-averaged electron density difference (vs. Au slab and gas phase BP (a) and H2bim (b) molecules), showing electron density depletion from the BP , H2bim plane (dashed blue line, far right) into top level of Au. z axis is normal to Au planes; bottom Au plane is at 8.4 Å. BP plane is ~ 3 Å from the top Au layer.

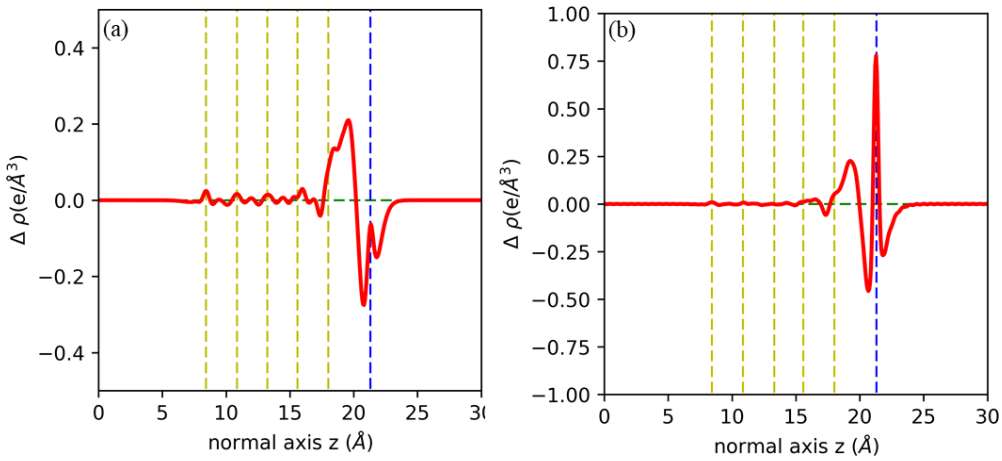

Figure 4.6: Edge-on view (yellow are five planes of Au slab) of plane-averaged electron density difference (vs. Au slab and gas phase BP (a) and H2bim (b) molecular network), showing electron density depletion from the BP, H2bim plane (dashed blue line, far right) into top level of Au. z axis is normal to Au planes; bottom Au plane is at 8.4 Å. BP plane is ~ 3 Å from the top Au layer.

4.3.2 Metal organic chain formation

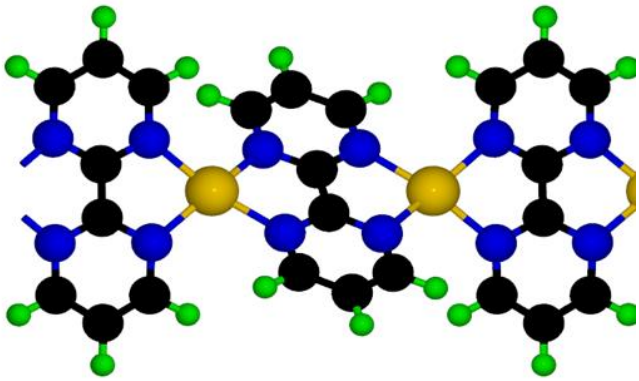

Figure 4.7: Schematic TM-BP network. The blue, black, golden, and green color balls represent N, C, TM, and H atoms, respectively.

In this section I will be comparing the formation energy of metal organic chain in a fourfold coordination with BP ligand with different TM as centers. The TM-BP chain is represented

schematically in Figure 4.7. The formation energy of TM-BP chains can be calculated using the equation

$$E_{form} = \frac{1}{2}\big(E(ML) - 2 \times E(L) - 2 \times E(M)\big) \qquad (4.4)$$

Where E(ML) is total energy of TM-BP chain, E(L) is the total energy of isolated BP molecule and E(M) is the total energy of TM atoms. The calculated values of formation energy for different TM atoms in TM-BP formation is shown in Figure 4.8 as a function of number of valence electrons. The calculated formation energy values show a trend of decreasing formation energy value for increasing number of valence electrons. We also compared the cohesive energy value of these used TM atoms. The comparison of cohesive energy value with the formation energy values suggest that for the TM atoms if the formation energy is higher than the cohesive energy, these TM atoms tend to form TM-BP chains as opposed to TM bulk formation or vis versa.

Our calculations further reveal the non-planar geometric structure of the species formed here. It is well established from molecular chemistry that the six membered ring of BP causes steric clash between neighboring ligands in M(bidentate)2 structures, leading to twisting of the two NMN planes defined by different bidentate ligands. This might conflict with the idea that surface complexes benefit from coplanarity of complex ring planes and the surface. Our calculation of a TM-BP chains in the gas phase (Figure 4.7) located a stationary state which was twisted ~ 32°. The twisted structure shows ferromagnetic ground state for V and Fe, and non-magnetic ground state for Sc and Zn. Although nonplanar, the trans angles NVN average 158°, thus leaving room for interaction with an arriving gaseous molecule.

In summary these chains, while not fully planar, offer reduced BP2- and oxidized TM with a structure suited for interaction with arriving reagent molecule. Changes to these conclusions as a result of these chains being calculated on an Au(111) surface are discussed later in this chapter.

Table 4.1: List of metal centers, the equilibrium M-M separation in units of Å, formation energies per ½ cell calculated in electron volts (eV), cohesive energy (eV), Bader charge (e) on M center, and magnetic ground states.

Metal Center	M-M distance	Formation energy	Cohesive energy	Bader charge on TM	Magnetic ground state
Sc	5.743	-6.57	4.12*	+1.69	NM
V	5.626	-6.20	6.03*	+1.25	FM
Fe	5.329	-5.20	4.87*	+0.99	FM
Zn	5.401	-2.24	1.12*	+1.17	NM

*[71]

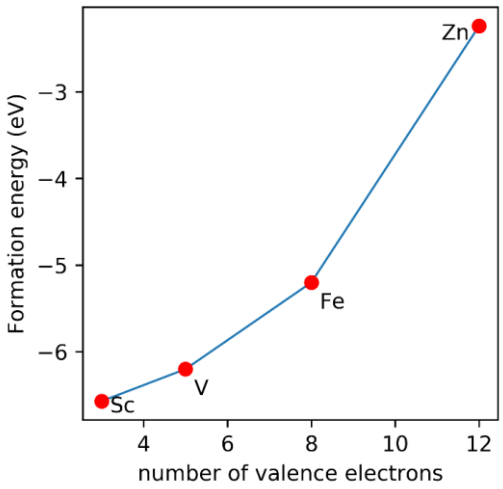

Figure 4.8: Formation Energies of M-BP chains in units of eV/ (1/2) cell, plotted against number of valence electrons of metal atoms.

For the interaction of metal centers with arriving atomic oxygen I have computed the adsorption energy of atomic oxygen on the metal site of these chains. The adsorption energy of atomic oxygen

on metal centers is presented in Table 4.2. The adsorption energy values are calculated using the equation

$$E_{ads} = \frac{1}{2}(E([OMBP]_2) - E([MPB]_2)) - \frac{1}{2}E(O_2) \quad (4.5)$$

Where $E([OMBP]_2)$ is the total energy of oxygen adsorbed complex, $E([MPB]_2)$ is the total energy of M-BP chain, and $E(O_2)$ is the total energy of molecular oxygen. The oxygen adsorption energy is highest in case of V and Sc, while oxygen makes a vertical bond with V and Sc. In case of Fe the Fe-O bond is tilted, and in case of Zn the interaction of Zn with oxygen is such that Zn lose one of the bonds with BP ligand. For comparison I presented the atom charge map for Fe-BP and V-BP chain as both chains form a magnetic ground state as opposed to the Sc-and Zn-BP chains.

Table 4.2:Adsorption energies of atomic oxygen, calculated in electron volts (eV)

Complex	Adsorption energy (eV)
ScBP	-3.77
VBP	-4.21
FeBP	-1.90
ZnBP	-1.94

The Bader charge analysis for V-BP and Fe-BP chain shows that V lose 1.25 e in V-BP formation, while Fe lose 0.99 e in Fe-BP formation. We have also computed the Bader charge on Sc-BP, Zn-BP and found that Sc is most oxidizing, and Zn is least oxidizing. The formation energy of Zn-BP is least among all suggesting a week Zn-BP coordination. The atom charge on adsorbed atomic oxygen is 0.65 e and 0.73 e for O-V-BP and O-Fe-BP, respectively. The Bader charge analysis is presented in Figure 4.9 and Figure 4.10 for V-BP and Fe-BP. The color code in Figure 4.9 and 4.10 represent blue for charge gain and brown for charge lose. The N atoms of the BP gains maximum charge, while C in CN2 of the ring lose maximum charge.

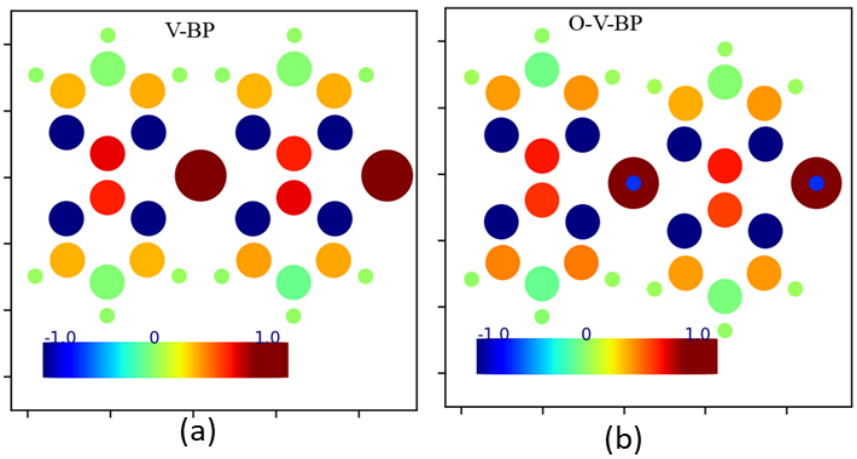

Figure 4.9: Bader charges on each atom of V-BP chain (a) and O-V-BP chain. Blue color represents electron accumulation and red color represents electron depletion.

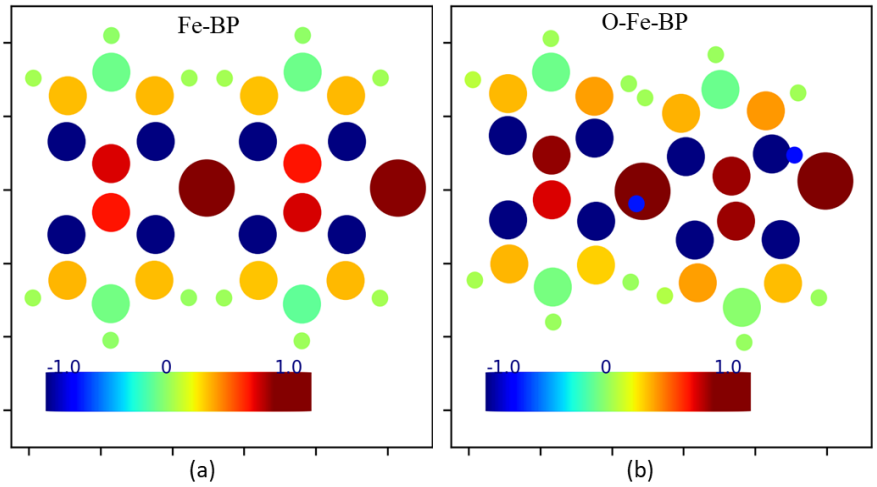

Figure 4.10: Bader charges on each atom of Fe-BP chain (a) and O-Fe-BP chain. Blue color represents electron accumulation and red color represents electron depletion.

4.3.3 Effect of Support on structure and charge state of V-BP

To study the effect of support on structure and charge transfer between V-BP chain and support I used Au(111) support. The Bader charges on top layer of Au(111) and the schematic representation of V-BP/Au(111) system is shown in Figure 4.11. After adsorption of V-BP chain on Au(111) support, V charge is increased to +1.4 e while in gas phase V-BP the charge on V was +1.25 e, and nitrogen are all -0.1 (less negative than without Au(111)), and carbons undergo largest (0.4 to 0.5) depletion of negative charge. All top layer Au closest to V gain negative charge (-0.14 to – 0.21), and they move out of that layer, towards V by ~ 0.2 Å, to V/Au distances of 2.57 Å, lower layers of Au gain no charge. The charge density redistribution is shown in Figure 4.12. and the plane averaged charged density difference is shown in Figure 4.13. Both charge density contour plot and plane averaged line graph show that charge redistribution is limited to the top layer of Au(111). As compared to gas phase V-BP non-planar chains, V-BP on Au(111) forms a quasi-planar structure. In sum, Au(111) accepts electrons from the highly reducing V-BP. While this means diminished

reducing power in the V-BP chain, the surface V-BP assembly retains reducing power, as is evident from observations with adsorption of O. The adsorption of O on V site also pulls V away from Au(111) surface and V-Au distance goes to 3.2 Å. The Bader charge profile on top layer of Au(111) after O adsorption on V-BP can be seen in Figure 4.14. The top layer Au closest to V gain negative charge (-0.12 e). The charge density redistribution plot (Figure 4.15) and plane averaged charge density difference plot (Figure 4.16) show that charged redistribution is limited to the top layer of Au(111) while depletion of charge on O-V-BP plane and accumulation of charge at V-BP and Au(111) interface site.

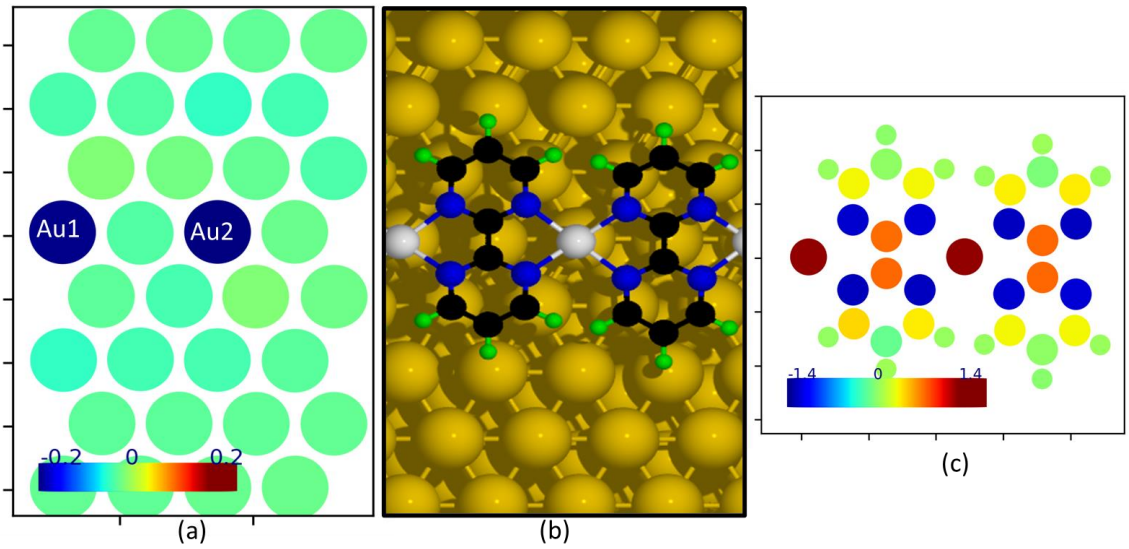

Figure 4.11: Bader charges on top layer of Au(111) (a) and schematic representation of V-BP chain on au(111) support(b) and Bader charges on V-BP chain (c) . The Au1 and Au2 are the Au atoms in direct coordination with V of V-BP chain. In (a) for visualization clarity I plot the Bader charge on the top layer Au(111) surface.

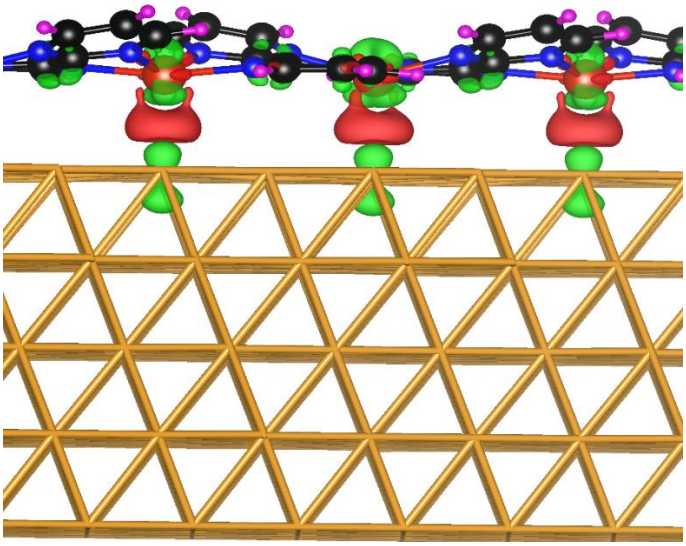

Figure 4.12: Charge density difference (red: accumulation, green: depletion) with BP chain superimposed (iso value 0.0005 e/Å^3).

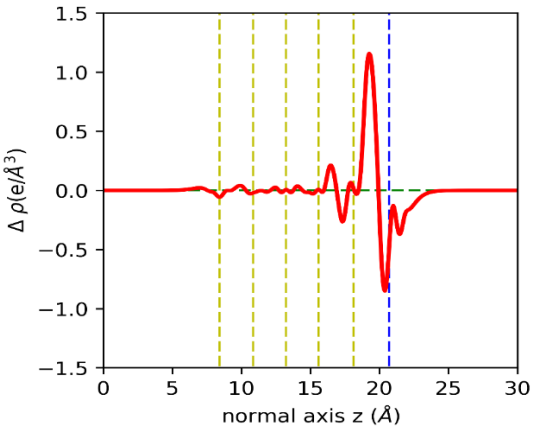

Figure 4.13: Edge-on view (yellow are five planes of Au slab) of plane-averaged electron density difference (vs. Au slab and gas phase V-BP chain), showing electron density depletion from the V-BP plane (dashed blue line, far right) into top level of Au. z axis is normal to Au planes; bottom Au plane is at 8.4 Å. V-BP plane is ~ 2.6 Å from the top Au layer.

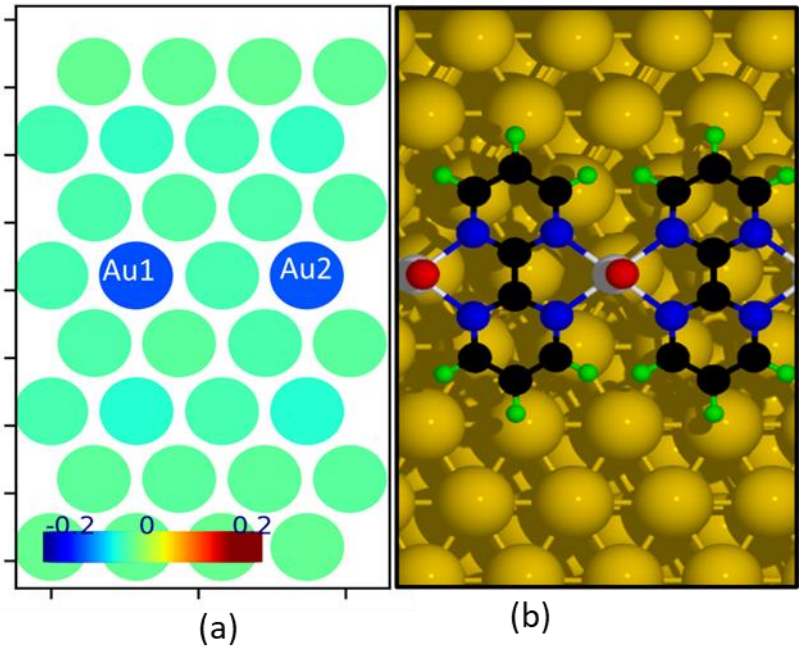

Figure 4.14: Bader charges on top layer of Au(111) (a) and schematic representation of O adsorption on V-BP chain on Au(111) support. The Au1 and Au2 are the Au atoms in direct coordination with V of V-BP chain. In (a) for visualization clarity I plot the Bader charge on the top layer Au(111) surface.

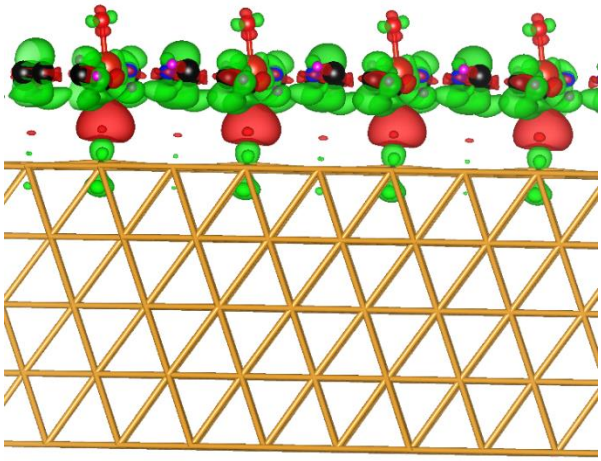

Figure 4.15: Charge density difference (red: accumulation, green: depletion) with BP chain superimposed (iso value 0.0005 e/Å^3).

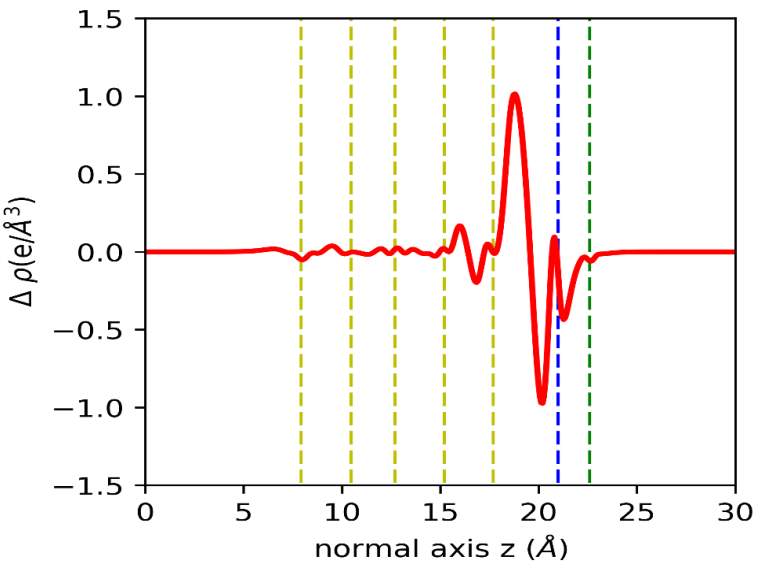

Figure 4.16: Edge-on view (yellow are five planes of Au slab) of plane-averaged electron density difference (vs. Au slab and gas phase O adsorbed V-BP chain), showing electron density depletion from the V-BP plane (dashed blue line, far right) into top level of Au. z axis is normal to Au planes; bottom Au plane is at 8.4 Å. V-BP plane is ~ 3.0 Å from the top Au layer

4.4 Summary

In sum, we have performed DFT calculations to screen TM-BP non-planar chains. The comparison of the cohesive energy values with the formation energy values suggest that the TM atoms tend to form TM-BP chains rather than TM bulk. The TM atoms donate charge to BP molecules making them positively charged, resulting in non-zero oxidation state. The calculated adsorption energies show that O adsorbs strongly on V, Sc, and Fe, and breaks the Zn-N bond of Zn-BP chain. Not only the effect of Au(111) support limited to the charge transfer from V-BP to top layer of Au(111), but the V-BP/Au(111) interaction converts the non-planar structure of V-BP into a quasi-planar structure

CHAPTER 5: REDOX-ACTIVE POLYMERIZATION OF SINGLE METAL ATOMS BY A KETONE FUNCTIONALIZED PHENANTHROLINE

5.1 Introduction

High selectivity is one of the key desired features for next-generation catalysts. In order to fully understand the active sites, metal sites of a well-defined chemical state and in highly regular structure must be stabilized on surfaces. In this chapter, we report the formation of single-site metal centers within phenanthroline (PDO) coordinated polymers, which are designed from 1:1 of PDO and transition-metal atoms (Table 5.1). This molecular design incorporates both redox activity and molecular self- assembly of single-site metal centers into thermally stable metal-ligand polymers . The functionalization of the phenanthroline core, with ketone, highlights the capability of the ligand to achieve redox activity during assembly into metal-ligand polymers. The ketone units and bi-dentate binding pockets allow formation of single-site metal centers with a well-defined chemical and structural state, for Pt as well as Fe and Cr [69]. While all three metals form the same polymer chain structure, combine with PDO, Fe and Cr more readily complex the ligand as compared to Pt. This difference raises interesting questions about the relative propensity of certain metals to interact with the ketone group. The thermally stable M-PDO serve as easily tuned model systems for single-site metal centers at surfaces that could be developed into support structures for future applications in catalysis [69]. In coordination with tetrazine-based ligand, on-surface Pt forms well-ordered metal-organic chains, and undergoes a chemical state change from Pt0 to Pt+2. [63,65]. A common challenge with the use of metals in traditional heterogeneous catalyst design is the tendency to form nanoparticles, which have a variety of local atomic coordination environments. It is for this reason that heterogeneous catalysts generally suffer from

poor selectivity compared to the well-defined inorganic metal-ligand complexes typical of homogenous catalysts.

The main goal of the study reported in this chapter is to develop transition metal centers with a well-defined oxidation state. These results could help design catalysts with chemically uniform reaction sites. We chose diketone-functionalized phenanthroline (1,10-phenanthroline5,6-dione, PDO) as ligand for two of its properties, both key to the achievement of this goal. First, its oxidative potential for stabilizing metal di-cations in two bidentate sites is desirable to produce a well-defined oxidation state of the coordinated metal centers. Second, the ligand's diverging geometry can lead to extended polymeric chains on the surface, thus producing highly uniform coordination environments for the metal centers. In this chapter, we demonstrate that the formation of PDO on any one of the metals under study (Sc, Ti, V, Cr, Mn, Fe, Ru, Pt) leads to a reaction that produces 1D polymer chains of oxidized metal sites and reduced ligands.

5.2 Computational Method

We performed Spin-polarized density functional theory (DFT) simulations for gas phase M-PDO metal-organic networks and for V-PDO on the Au(111) surface using the Vienna Ab-initio Simulation Package (VASP) [70] employing the projector-augmented wave (PAW) [27] and plane wav basis set methods. We used DFT-D3 [18] corrections for accounting the van der Waals interactions. The energy cutoff for plane wave expansion was set to 500 eV. The minimum vacuum layer thickness is ~ 15 Å which is large enough to avoid the interaction between neighboring images. We sampled the Brillouin Zone with 3×1×1 Monckhorst-Pack grid [22] for the K-points. Atomic charges were evaluated using the Bader analysis [29]

The model system is shown schematically in Figure 5.1. Each unit cell is composed of two metal centers (both are Sc, Ti, V, Cr, Mn, Fe, Ru, or Pt) and two PDO molecules. To get the equilibrium metal-metal (M-M) separation, we relaxed the system allowing the M-M separations to obtain the equilibrium separation. Here, formation energy (E_f) is defined as

$$E_f = \frac{1}{2}\{E_t - 2 \times (E_{mol} + E_{metal})\} \quad (5.1)$$

where $E_t$is the total energy in of the MOC, and $E_{mol}$and E_{metal}, are the energies of molecule, and metal atom, respectively.

For calculations of adsorption energies of CO and O on metal site of M-PDO chain we have chosen the systems with planner geometrical configuration. Adsorption energy is defined as,

$$E_{ads} = E_{MOC+mol} - E_{MOC} - E_{mol} \quad (5.2)$$

Here and $E_{MOC+mol}$, E_{MOC} and E_{mol} are the total energies of M-PDO chain with the adsorbed molecule, the isolated M-PDO chain and the isolated gas molecule (CO, O, N and O_2), respectively. The negative values of E_{ads} represent exothermic reaction which are favorable as the activation energy barrier for these reactions to take place is smaller as compared to the endothermic reactions for reaction rates

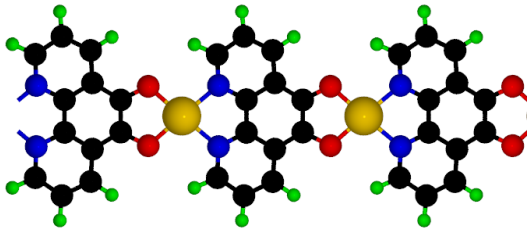

Figure 5.1: Schematic representation of M-PDO chains used in the calculations. Large gold balls represent metal atom, black balls represent C, blue balls represent N and green balls represent H atoms, respectively.

5.3 Results and discussions

5.3.1 M-PDO Chain formation

Figure 5.3 summarizes formation energies, of all studied M-PDO chains under consideration. By analyzing the geometries, we found that all systems form planar chain structure. Note that we have simulated all these system in gas phase. For comparison we listed the formation energies and cohesive energies of these TM atoms in their respective bulk formations (Table 5.1) clearly the absolute value of formation energy in TM-PDO chain formation is higher than the cohesive energy value indicting that all the listed TM prefer to form TM-PDO chains as compared to TM aggregates or cluster formation. Tetrahedral (Figure 5.2) V-PDO in the gas phase has VO2 and VN2 planes accurately orthogonal (89.9^{o}) and only slight distortion of the angle between C2 axes of two different PDO, at 169.9^{o}. There are no significant differences among VO or among VN distances from this distortion suggesting that the PES is soft to slight bending. Distances within the PDO are unchanged from those in the planar form, so the degree of charge transfer is not significantly changed

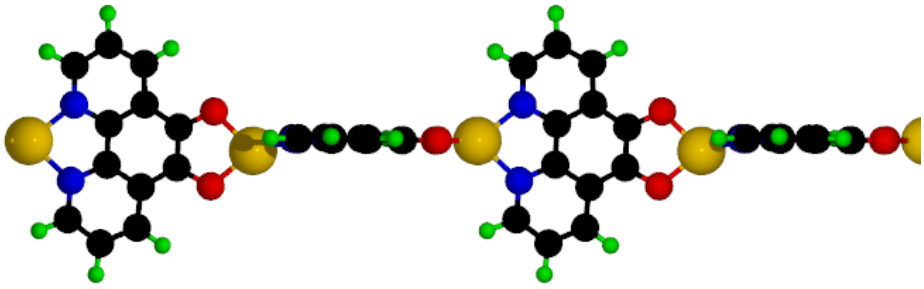

Figure 5.2: Schematic representation of M-PDO chains in tetrahedral geometry. Large gold balls represent metal atom, black balls represent C, blue balls represent N and green balls represent H atoms, respectively

Table 5.2 lists Bader charges of metal atoms in M-PDO chain structure. Atomic charges are never as large as formal metal oxidation state integers, but trends are useful in tracking changes in a periodic table series. These show vanadium to be the most reducing, Fe less and Pt least of all. Metalation of PDO adds negative charge to O, to N and to the C attached to those heteroatoms, but other carbons change negligibly. The atomic charges on each atom of M-PDO chain structure is represented in color code as shown in Figure 5.4.

Table 5.1: List of metal centers, the equilibrium M-M separation in units of Å, formation energies per ½ cell calculated in electron volts (eV), and magnetic ground states.

Metal Center	M-M distance	Formation energy	Cohesive energy	Magnetic ground state
Sc	8.14	-8.94	4.12*	AFM
Ti	8.03	-8.79	5.45*	AFM
V	7.94	-7.95	6.03*	FM
Cr	7.86	-7.02	4.00*	FM
Mn	7.73	-6.48	3.73**	AFM
Fe	7.68	-6.81	4.87*	FM
Ru	7.95	-7.03	6.67*	AFM
Pt	7.86	-7.37	5.50*	NM

*Ref[71], ** Ref[72]

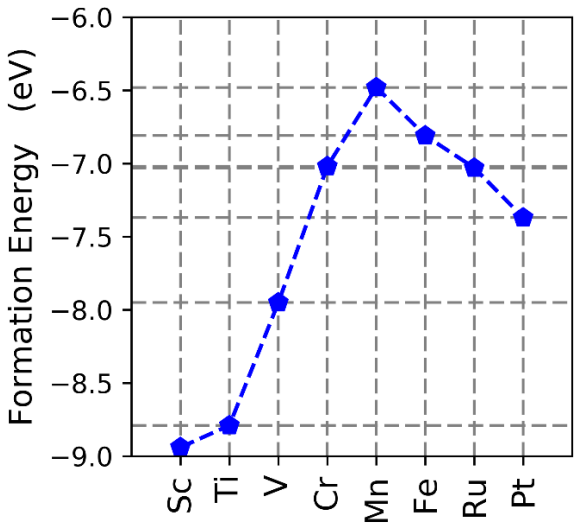

Figure 5.3: The calculated value of formation energies for various M-PDO chain structures

Table 5.2: Bader charges on Metal atoms of M-PDO chain and the O and N atoms of the ligand coordinated with metal atom.

Metal Center	Charge Lose (M)	Charge gain (N)	Charge gain (O)
Free		-1.17	-1.04
Sc	+1.76	-1.31	-1.13
Ti	+1.52	-1.22	-1.11
V	+1.38	-1.11	-1.24
Cr	+1.30	-1.24	-1.12
Mn	+1.34	-1.26	-1.07
Fe	+1.19	-1.27	-1.07
Ru	+1.07	-1.21	-1.05
Pt	+0.83	-1.16	-1.02

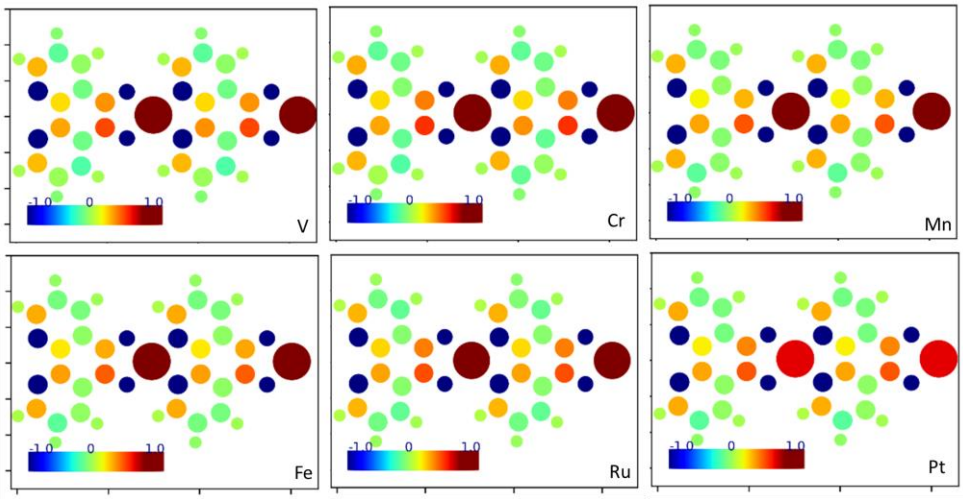

Figure 5.4: Bader atom charges on each atom of M-PDO chain, M=V, Cr, Mn, Fe, Ru, Pt

5.3.2 Magnetic properties of M-PDO chains

We have carried out DFT calculations in ferromagnetic (FM), antiferromagnetic (AFM) and non-magnetic (NM) states which enables us to determine the lowest energy configuration. For NM state, calculations were performed without considering spin polarization, for FM state we assign parallel spin to both the metal centers with in the cell, while for AFM state we assign anti-parallel spin to the metal centers (spin up for first metal center and spin down for second metal center). For each chain we have considered these three magnetic configurations, and found that V, Cr and Fe based M-PDO in FM state has lowest energy, while Sc, Ti, Mn and Ru centered chains have lowest energy in AFM state. Pt-PDO chain show nonmagnetic ground state. The local magnetic moment on each metal site and the neighboring N and O atoms is listed in Table 5.3. The calculated values show that unpair spin is mainly concentrated on metal site (see Figure 5.5) . Among all the studied M-PDO chains V, Cr and Fe-PDO form ferromagnetic ground states. The local magnetic moment on each of these metal atoms is 2.41, 3.47 and 2.01 $\mu_B/atom$ respectively. The Sc, Ti,

Mn and Ru-PDO chains AFM ground states. Here we refer the FM and AFM to the spin orientation of neighboring metal atoms. The spin orientation on neighboring metal atom parallel/anti-parallel is named as FM/AFM. The magnetic moment on Sc, Ti and Ru atoms is ± 0.19, ± 1.24, ± 3.14 and ±1.65 $\mu_B/atom$ respectively. In case of AFM the net spin on the neighboring ligands is anti-parallel.

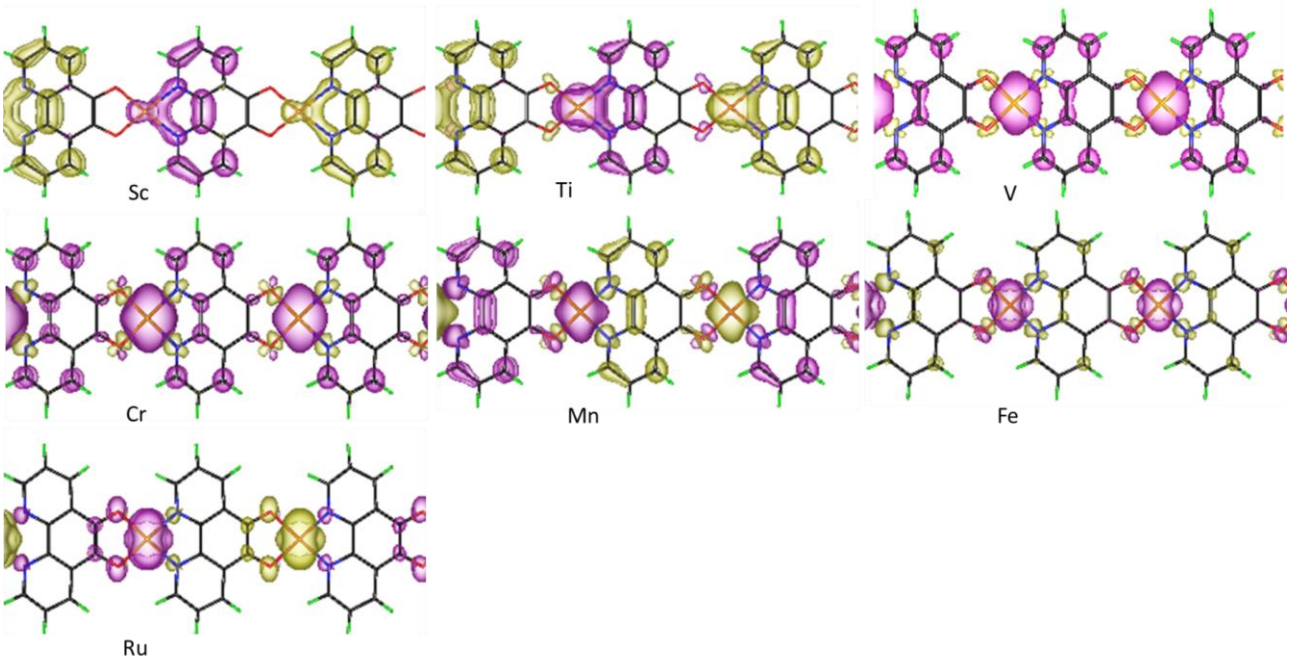

Figure 5.5: Spin density map of Sc, Ti, V, Cr, Mn, Fe and Ru-PDO chains, respectively. The magenta color represents majority spin density and yellow color represents minority spin density. The contour values are set to 0.002 e/Å^3

Our goal here is to establish the nature of bonding between elemental metal M and PDO, which has been shown to form linear chains. DFT calculation yielded stationary states for all M as planar and linear chain in the gas phase with two identical MO and two identical MN distances at each metal. Overall, the DFT evidence indicates that there are differences in charge transfer between

the M studied and PDO, but bond lengths within PDO are relatively insensitive to those, and atomic charges (Table 5.2) better reveal the incremental changes

Table 5.3: Local magnetic moment (μ_B) on Metal atoms in M-PDO chain formation, N and O atoms of the ligand coordinated with metal atoms.

Metal center	Magnetic moment/M	N(M)	O(M)
Sc	± 0.19	± 0.05	± 0.002
Ti	± 1.24	± 0.02	±0.02
V	2.41	-0.02	-0.04
Cr	3.47	-0.04	-0.02
Mn	± 3.14	± 0.06	± 0.003
Fe	2.01	-0.03	0.002
Ru	±1.65	±0.05	± 0.02
Pt	0.00	0.00	0.00

5.3.3 Effect of Au(111) support

The overall study reveals favorable thermodynamics for combining elemental M and PDO, and that those chains achieve additional stabilization from binding to Au(111) surface. In V-PDO/Au(111), gold atoms rise out of the surface plane, and V moves out if its N2O2 plane, all to form V-Au bonds. In V-PDO/Au(111), gold atoms nearby V show charge transfer from VPDO, consistent with the unusual ability of element gold to accept, not only donate electrons, the former when the surface metal/ligand addend is exceptionally electron rich as it is in V-PDO. The

alternative of tetrahedral N2O2 structure around V in the gas phase was sought and a tetrahedral structure was found lower in energy by 0.07 eV; this is a relatively minor penalty to pay when a planar structure is adopted on Au(111).

Atomic charges (Table 5.2) are never as large as formal metal oxidation state integers, but trends are useful in tracking changes in a periodic table series. These show vanadium to be the most reducing, Fe less and Pt least of all. Metalation of PDO adds negative charge to O, to N and to the C attached to those heteroatoms, but other carbons change negligibly.

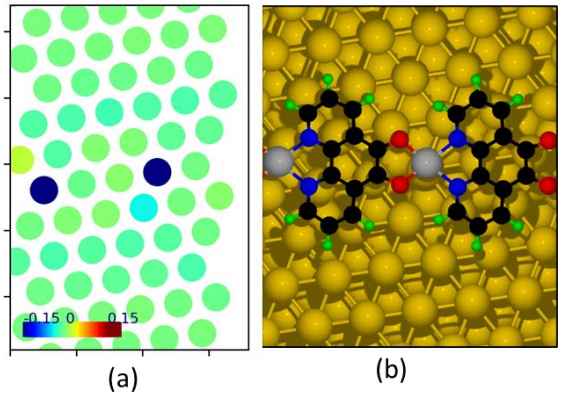

Figure 5.6: Bader charges on top layer of Au(111) (a) and schematic representation of V-PDO chain on Au(111) support. In (a) for visualization clarity I plot the Bader charge on the top layer Au(111) surface.

5.3.4 Reactions

We next moved to study possible atom and groups bound to these electron rich chains including again how changing metal can change interaction between chain and added moiety. We chose, as added groups, O, CO and CH2, to deal with extremes of oxidizing power (O), of pi back donation (CO) and of a carbene for its potential to effect catalytic conversion of olefins. Our goal is to learn the thermodynamics of formation of these, but also the nature of their bonding.

We want to test some of thermodynamic reactions like, $MPDO + \frac{1}{2}O_2 = OMPDO$, $MPDO + CO = OCMPDO, MPDO + \frac{1}{2}H_2CCH_2 = H_2CMPDO$. We have calculated the binding energy of the species O, CO and H_2C on MPDO using the following equations,

$$E_b(H_2C) = \frac{1}{2}(E[H_2C\text{MPDO}]2 - \text{E[MPDO]}2 - \text{E}[H_2C\ CH_2])$$

$$E_b(O) = \frac{1}{2}(E[O\text{MPDO}]2 - \text{E[MPDO]}2 - \text{E}[O_2])$$

$$E_b(CO) = \frac{1}{2}(E[OC\text{MPDO}]2 - \text{E[MPDO]}2 - \text{E[CO]})$$

Table 5.4: Binding energies of O, CO and H2C on MPDO

Complex	Binding energy (eV)
OVPDO	-4.58
OFePDO	-1.78
OCVPDO	-2.89
OCFePDO	-1.54
H2CVPDO	0.14
H2CFePDO	0.74

Adding two oxygen atoms per vanadium to the V(PDO) chain yields the first evidence for oxidation of PDO^{2-}. The most stable structure has two oxo (di-anionic oxide) groups in a *cis* arrangement on each vanadium (Figure 5.7). With negligible spin density on the metal (see Figure 5.8), and thus consistent with a d^0 configuration. One bond from vanadium to PDO oxygen has been totally lost and a second VN is lengthened by 0.3 Å (relevant molecular structures show that any bond trans to oxo is lengthened, as it is here), resulting in tetrahedral vanadium having four

ligand atoms at typical distances and one quasi bond. This is a typical coordination number for vanadium +5 with two terminal oxo ligands; those molecular species can be 5- and 6-coordinate, most often with bi- and tridentate ligands. The bond lengths in the PDO substructure of $V(O)_2$(PDO) are consistent with semiquinone form, as are the spin densities on selected atoms there. The PDO oxygen not bonded

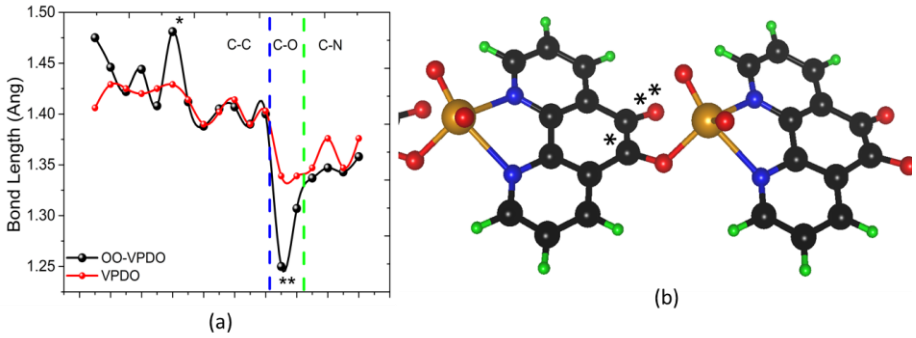

Figure 5.7: Comparison of bond lengths of VPDO vs OO-V-PDO chain (a) and schematic representation of OO-V-PDO chain(b). Large gold balls represent metal atom, black balls represent C, blue balls represent N and green balls represent H atoms, respectively

to vanadium takes on ketonic character, with a short C=O distance. The anionic (alkoxide) PDO^{1-} oxygen donates to vanadium. If two O atoms oxidize the V(PDO) by four electrons, it becomes of interest where three electrons will come from in the nitride NV(PDO). Alternatives, to achieve an octet at nitride nitrogen, N3-, are V(5+)PDO(2-) or V(4+)PDO(1-); the former has a d^0 configuration at V while the latter has d^1 vanadium, with unpaired spins on the radical PDO^{1-}. Geometry optimization of this species shows square pyramidal structure, mirror symmetric, with short VN at 1.595 Å. Distances within the PDO of NV(PDO) match those of a range of calculated AM(PDO) species (above) including OV(PDO), thus consistent with PDO(2-). The evidence is

that an arriving nitrogen atom only oxidizes V(PDO) by two electrons, and those come primarily from the initial V(2+). Residual spin density on the nitridyl nitrogen may forecast susceptibility

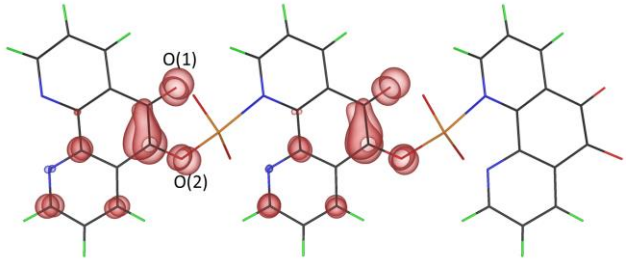

Figure 5.8: Spin density map of OO-V-PDO chain. The contour values are set to 0.005 e/Å^3

to hydrogen atom transfer reactivity. These results also reveal the strong resistance of PDO(2-) in V(PDO) to reducing arriving substrate; the reducing power resides primarily in the metal, augmented by the pi donation from N and O of the di-anionic chain-builder ligand.

5.4 Summary

In sum we have performed DFT calculations to characterize the M-PDO chains based on the geometry, chemical and charge state of different metals in coordination with PDO ligands. Overall DFT results based on comparison of energy of formation to the cohesive energy show that TM atoms prefer to adopt a fourfold coordination as MN2O2 with PDO ligand as opposed to forming metal bulk. The atomic charges show V be the most reducing, Fe less and Pt least of all. Metalation of PDO adds negative charge to O, to N and to the C attached to those heteroatoms, but other carbons change negligibly. In V-PDO/Au(111), Au atoms rise out of the surface plane, and V moves out if its N_2O_2 plane, in the process of forming V-Au bonds. In V-PDO/Au(111), Au atoms near V show charge transfer from V-PDO.

CHAPTER 6: COMPLEXATION OF Fe2 IN METAL-ORGANIC REDOX ASSEMBLY

6.1 Introduction

Single-site metal centers have generated interest for applications in heterogeneous catalysis for desirable high product selectivity. The strategies to achieve single-site centers (SSCs) include: single atom alloys [73-77], selective grafting [78], and 1D metal– ligand coordination networks [63,64,69] . The uniformity of active sites in metal organic complexes offer reactivity analogous to that of molecular catalysts while maintaining the practical benefits of traditional heterogenous catalysts. The ability of a ligands to finely tune the reactivity of a reaction is one of the major advantages of homogeneous molecular catalysts over typical heterogeneous systems. However, the extent of complexity and redox charge transfer that can be achieved in an on-surface coordination environment is not fully understood. To understand the metal organic complex formation, we used a new family of ligands with strong electron-accepting capacity and a flexible coordination environment. Our approach relies on the coordination of an organic ligand with elemental metal (Fe). Previous work has demonstrated the ability of systems to form highly ordered and regular single-site metal assemblies [63,64,69]. These assemblies have demonstrated the ability to facilitate higher selectivity as illustrated by the reaction of molecular oxygen with V-dipyridyl tetrazine (DPTZ) chains [68]

6.2 Objective

We aim to design a metal-organic system in which two metal centers would be close to each other, enabling the cooperative reactivity of these metals on a single molecular adsorbate. This arises

from a several examples, in molecular chemistry, where the reactivity of a complex depends on two metals cooperatively activating a substrate either in a bi-metallic complex or as two equivalents of a mono-metallic species [79-83]. On the other hand, there are few examples of bi-metallic complexes that have been observed on surfaces. The ability of Fe2 centers in metal–organic coordination networks to dissociate the bond of molecular oxygen as well as capture CO_2 has been demonstrated [84,85]. In order to mirror the successes of bi-metallic systems in molecular chemistry, our collaborators have designed and synthesized a tetra-aza-anthraquinone ligand (TAAQ, Figure 6.1 (a)) which in principle may host a metal at each of its four equivalent binding sites, and we have performed density functional theory based calculations on metal organic complexation.

As we discussed in chapter 3 , the tetrazine-based ligand, DPTZ has demonstrated on-surface redox-activity. However, DPTZ is only able to undergo a two-electron reduction, which limits the complexation to one metal per ligand. Some studies using a more oxidizing ligand, Bis-pyrimidinyltetrazine (BMTZ) have shown the ligand is able to undergo a three-electron reduction. However, even though BMTZ has multiple binding pockets, when exposed to excess V the ligand only coordinates one metal [64]. The key design feature of the ligand, TAAQ, is the ability to have multiple binding pockets. To fully utilize the available binding pockets, it was also essential to design the ligand with the capacity for multiple electron reduction so that it could fully utilize the pockets and achieve higher metal:ligand ratios than previously realized. The TAAQ ligand, due to their favorable redox properties, have also been used as a conductive linker in organic electronics [86,87]. In this chapter, I will present the DFT results on complexation of TAAQ with elemental Fe, leading to complex metal–organic chains. The formation of chains with irregular

structure, pointing to a variety of local coordination geometries. I will present the relative thermodynamics, local spin state of metal center and quantify the amount of charge it donates to the TAAQ ligand. I will also discuss the vibrational characteristics of TAAQ molecules in gas phase as well as on Au(111) and TAAQ 1-layer network in gas phase as well as on Au(111)

6.3 Computational details

We performed first-principles calculations based on density functional theory (DFT) as implemented in the VASP code [70] employing the projector-augmented wave (PAW) [27] method to treat the interaction between ionic core and valence electrons. We used the generalized gradient approximation (GGA) proposed by Perdew, Burke, and Ernzerhof (PBE) [15] together with the DFT-D3 correction[18] to describe the exchange-correlation of electron and to account for van der Waals interaction. The energy cutoff was set to 500 eV for the plane-wave expansion. All atoms were allowed to relax until the residual force on each atom is below 10^{-2} eV/Å. Our simulation supercell consists of 1 or 2 TAAQ molecules and several Fe atoms corresponding to the Fe:TAAQ ratio of 1:1, 2:1, and 4:1. The Fe atoms and TAAQ molecules form linear chains along x-direction. We separated the chains with their periodical image along y and z directions by vacuum gaps of about 15 Å . We used 3×1×1 mesh in performing integration over the Brillouin zone, which is sufficient for the convergence of formation energy. In case of TAAQ 1L-network on Au(111) we used a five layer of Au(111) slab. We obtained the interionic force constants using VASP [70], the frequencies of vibrations are obtained by diagonalizing the dynamical matrix [88].

We used DFT to simulate various Fe:TAAQ chain structures corresponding to different Fe:TAAQ ratios. Figure 6.2 shows 7 $Fe_n(TAAQ)_m$ formula unit of chain structures resulting from

our simulations. Here, n and m are the numbers of Fe and TAAQ, respectively, in a Fe_n:$TAAQ_m$ chain. The formation energy per formula unit is defined as

$$E_F = E_{Fe:TAAQ} - n \times E_{Fe} - m \times E_{TAAQ} \quad (6.1)$$

and the binding energy of Fe in the chain is defined as

$$E_B = \frac{1}{2}(E_{Fe:TAAQ} - n \times E_{Fe} - m \times E_{TAAQ}) \quad (6.2)$$

where $E_{Fe:TAAQ}$, E_{Fe}, and E_{TAAQ} are the total energy of one formula unit of Fe_n:$TAAQ_m$ chain, isolated Fe atom, and isolated TAAQ molecule, respectively.

6.4 Results

6.4.1 Complexation of Fe-TAAQ

We studied the complexation of TAAQ with elemental Fe, leading to complex metal–organic chains. The key features of the TAAQ, is the ability to have multiple binding pockets. We can utilize the pockets and achieve higher metal:ligand ratios. To provide an understanding of the non-uniform chain structure of Fe:TAAQ seen in STM [89], we performed periodic structure calculations using density functional theory for seven candidate Fe:TAAQ chain structures, representing 1:1, 2:1, and 4:1 Fe:TAAQ stoichiometry. In further support of metallic Fe being present vs. all the Fe complexed in the ligand, our calculations suggest that at high Fe:TAAQ ratio, iron atoms prefer forming metallic clusters on Au(111) to being in Fe4TAAQ. Once Fe atoms are deposited on the Au surface with the presence of TAAQ, Fe atoms either form Fe clusters or find TAAQ to form Fe-TAAQ complexes. Thus, the competition between binding energy of Fe on Au(111) and in Fe-TAAQ chains determines the formation of Fe-TAAQ chains. We found that

binding energy of Fe on the Au(111) surface ranges from -4.257 to -5.117 eV, corresponding to the case that Fe atoms form an adlayer on the Au(111) surface and that Fe atoms form big clusters (bulk like), respectively. Since the amount of Fe is small, the lower (absolute) value is more likely. Our results of various Fe:TAAQ ratio, suggests that thermodynamically one cannot create Fe-TAAQ species with higher than 2:1 metal:ligand ratio.

While 1:1 and 4:1 Fe:TAAQ ratio structures are straightforwardly designed, 2:1 species are not. Among 2:1 species, numerous optimized structures result in four-coordinate iron with highly distorted geometries. They are noteworthy in having nonplanar iron coordination geometry, between tetrahedral and planar, and with a narrow O-Fe-O angle (~72^{o}) and a very wide NFeN angle (~142^{o}), all constrained by ligand donor locations; they also demand considerable nonplanar distortion of the TAAQ ligand and have long Fe-N distances (2.04 and 2.10 Å). They differ only in the displacement of the ligand plane within the chain. For assembly Fe2TAAQ 4-Coordinate tilt, the ligand planes deviate 21^{o} from planarity to give parallel tilted (vs. coplanar) ligands while in contrast, in Fe2TAAQ 4-Coordinate up/down, they retain relatively planar, but results in an alternating “up/down” assembly. Geometry optimization starting from Fe2TAAQ structures with T-shaped Anti and Syn coordination environments led to these four coordinate Fe2TAAQ assemblies, again supporting the energetic importance of avoiding unsaturated (lower coordination number) iron. Figure 6.3 demonstrates this rearrangement to form a new Fe-N bond having very

similar, nearly equi-energetic 4-coordinate structures. Both final geometries yield linear chains.

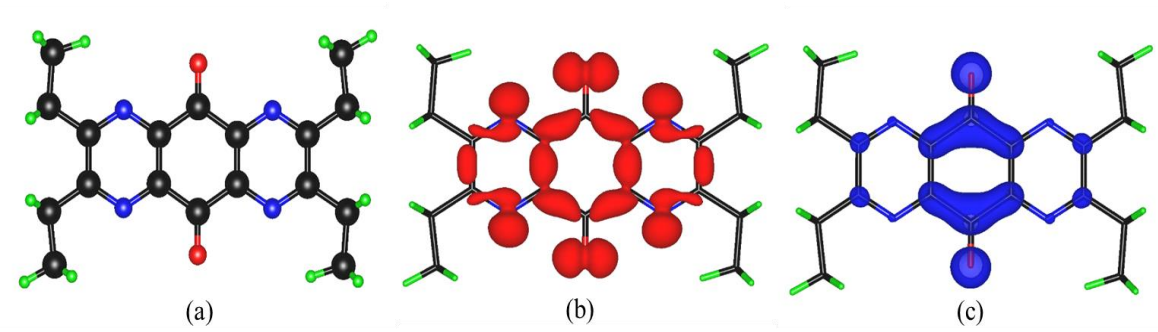

Figure 6.1: Schematic representation of (a) tetraethyltetra-aza-anthraquinone (TAAQ). The black, red, blue and green balls represent C, O, N, and H, atoms respectively. The red (b) and blue (c) color contours represent HOMO and LUMO respectively. The iso value is set to 0.005 e/Å^3

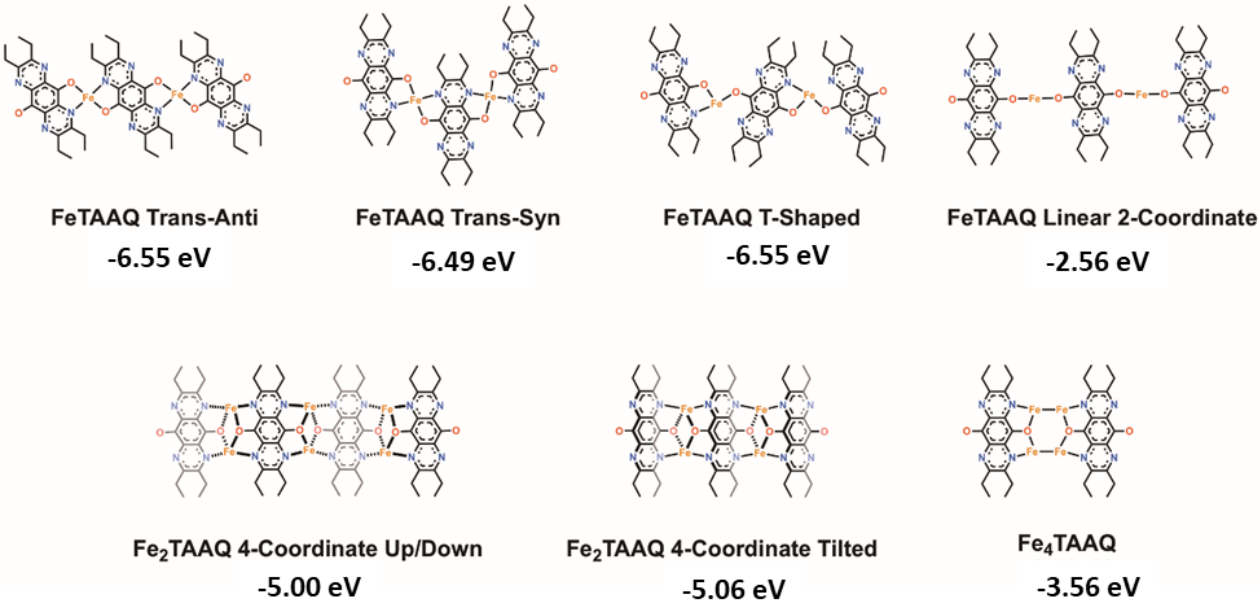

Figure 6.2: Candidate Fe-TAAQ binding structures with their DFT-calculated Fe binding energies.

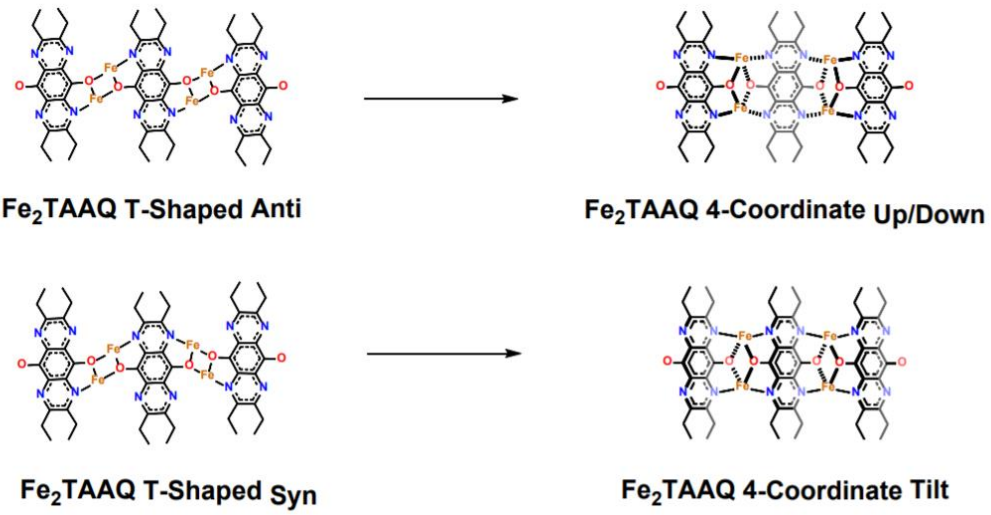

Figure 6.3: Structure transformation of 2:1 Fe:TAAQ species from starting geometry (left) to optimized structures (right).

Table 6.1: The calculated value of formation energy of Fe-TAAQ chain structures in gas phase, and Fe binding energy.

Coordination Chain	Formation energy (eV/mol)	Fe binding energy (eV/mol)
FeTAAQ Trans-Anti	-6.55	-6.55
FeTAAQ Trans-Syn	-6.49	-6.49
FeTAAQ T-shaped	-5.55	-5.55
FeTAAQ Linear 2-Coordinate	-2.56	-2.56
Fe_2TAAQ 4-Coordinate up/down	-9.99	-5.00
Fe_2TAAQ 4-Coordinate tilt	-10.13	-5.06
Fe_4TAAQ	-14.22	-3.56

6.4.2 Magnetic Properties of FeTAAQ chains

We performed spin polarized calculations to determine the magnetic ground state of Fe-TAAQ chains. In all calculations our simulation unit consist of 2 TAAQ ligands with 2 and 4 Fe atoms. By comparing the total energy of Fe-TAAQ in all possible spin orientations, we present the Fe-TAAQ chains with lowest energy in particular spin orientation. As can be seen in spin density map plot of Fe-TAAQ chains in Figure 6.4, the spin density is concentrated at Fe site in all cases. Chains with single Fe center the spin on one Fe atom is antiparallel to another Fe. However, chains with 2 Fe on site, in case Fe_2-TAAQ tilt spin on one Fe ais antiparallel to another Fe nearby. These two Fe atoms are connected via O atoms. In case of Fe_2-TAAQ up/down spin on one Fe is parallel to spin on another Fe. The spin on the two Fe atoms in direct coordination with each other in case of Fe_4-TAAQ is parallel, and antiparallel to the spin on Fe pair in coordination via O atoms. The calculated local magnetic moment on Fe atoms in each Fe-TAAQ chain is shown in Table 6.2.

Table 6.2: Calculated magnetic moment in units of $\mu_B/atom$ on Fe site of Fe-TAAQ chains.

Coordination Chain	Fe magnetic moment
FeTAAQ Trans-Anti	+1.91(-1.91)
FeTAAQ Trans-Syn	+1.96(-1.96)
FeTAAQ T-shaped	+1.96(-1.96)
FeTAAQ Linear 2-Coordinate	+3.174(-3.174)
Fe_2TAAQ 4-Coordinate up/down	+3.32(-3.32)
Fe_2TAAQ 4-Coordinate tilt	+3.34(-3.34)
Fe_4TAAQ	+3.35(-3.35)

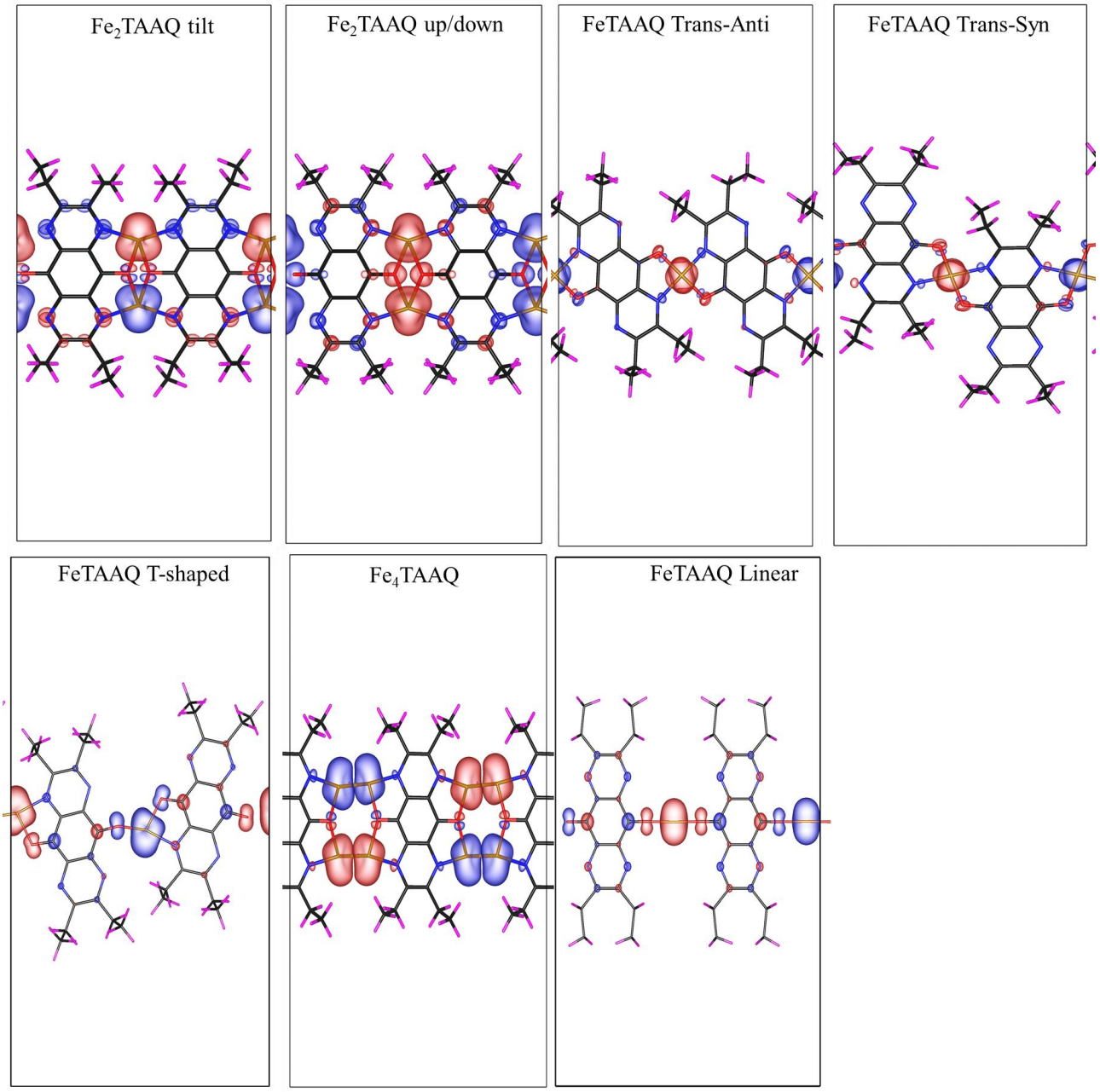

Figure 6.4: Spin density map of Fe-TAAQ complexes. The red color represents majority spin density and blue color represents minority spin density. The contour values are set to 0.005 e/Å^3

6.4.3 Charge Analysis of FeTAAQ chains

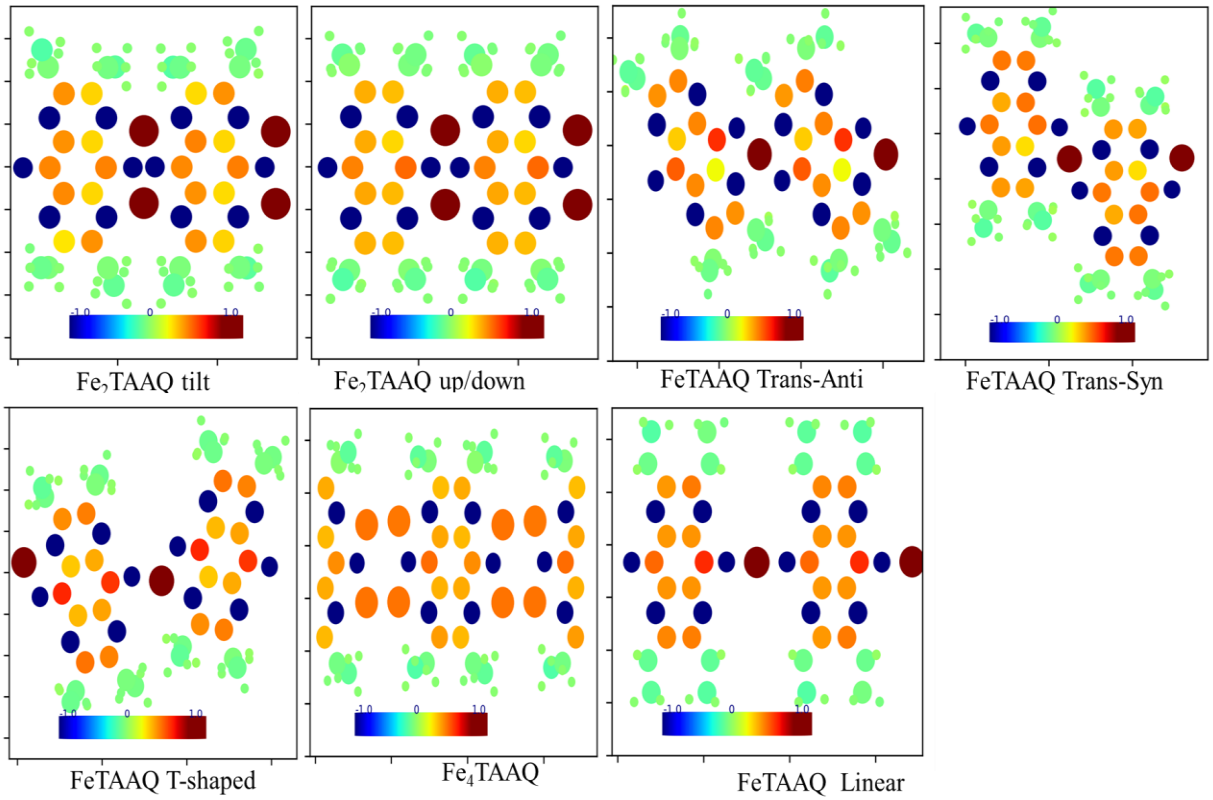

Figure 6.5: Atom charges on each atom of Fe-TAAQ chains.

We present the atom charges on each atom of all Fe_nTAAQ_m chains in Figure 6.5. The color code blue for charge gain and brown for charge lose shows that in all cases Fe lose charge and TAAQ gains charge. For comparison I presented the atom charge on Fe, N and O in Table 6.3. The charge on both N and O atoms in Fe_nTAAQ_m chain formation as compared to charge in case of free TAAQ ligand shows that both N and O gain charge while Fe lose charge. The amount of charge lose by Fe atom on average is ~ 1.15e in all cases however in case of Fe_4-TAAQ Fe lose on average ~0.58 e.

Table 6.3: Bader charges on Metal atoms of Fe-TAAQ chain and the O and N atoms of the ligand coordinated with metal atom

Coordination Chain	Charge (Fe)	Charge (N)	Charge(O)
Free		-1.15	-0.98
Fe_2TAAQ tilt	+1.14	-1.24	-1.09
Fe_2TAAQ up/down	+1.15	-1.24	-1.12
FeTAAQ Trans-Anti	+1.17	-1.19	-1.07
FeTAAQ Trans-Syn	+1.18	-1.17	-1.04
FeTAAQ T-shaped	+1.16	-1.26(-1.14)	-1.11
Fe_4TAAQ	+0.58	-1.24	-1.14
FeTAAQ Linear	+1.16	-1.18	-1.14

6.4.4 Vibrational spectroscopy of on-surface TAAQ complexation

To further investigate the changes in TAAQ in gas phase vs monolayer network formation on Au(111) we perform vibrational calculations based on finite displacement method for both TAAQ gas phase as well as TAAQ molecule and molecular monolayer network on Au(111). For TAAQ molecular crystal, the ketone C=O stretch mode is (see Figure 6.7) observed around 1682 cm^{-1}. For comparison I plot the IR spectrum of isolated TAAQ molecule, TAAQ molecular network (gas phase Figure 6.6), TAAQ molecular crystal and found that C=O stretch mode is observed around 1698 cm^{-1} in case of isolated TAAQ molecule, and 1687 cm^{-1} in case of TAAQ molecular network. The comparison with experimental high resolution electron energy loss spectroscopy

(HREELS) measurements were made ase shown in Figure 6.7. We can follow from Figure 6.7, that the calculated IR spectrum has a good match with the experimental HREEL curve for TAAQ molecular crystal. We also calculated the IR spectrum for TAAQ molecule on Au(111) support. The representative unit TAAQ on Au(111) is shown in Figure 6.8. We calculated the IR spectrum systematically by including the contribution of Au(111) support layer by layer to trace the effect of Au(111) support on IR spectrum on TAAQ molecule. The calculated IR spectrum (Figure 6.9) shows that the effect of Au(111) support is more to the low frequency < 500 cm^{-1} modes. We started the calculations by fixing the Au(111) support, and allow the molecule displacement, consequently we get the IR spectrum for the molecule (blue color in Figure 6.9). We than include the effect of Au(111) by allowing the Au(111) displacement layer by layer from top layer to the bottom layer and plotted corresponding IR spectrum by including the displacement of Au(111) layers. The value of C=O stretch mode is observed around ~1650 cm^{-1} for TAAQ molecule on Au(111). As compared to gas phase TAAQ the intensity of C=O substantialy reduced when TAAQ molecule (Figure 6.9) and also TAAQ molecular network (Figure 6.10) on Au(111).

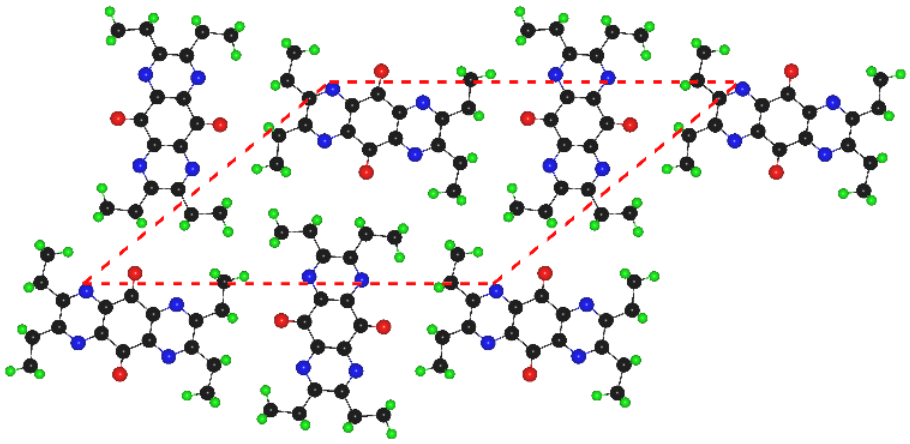

Figure 6.6: Schematic representation of TAAQ network. The black, red, blue and green balls represent C, O, N, and H, atoms respectively.

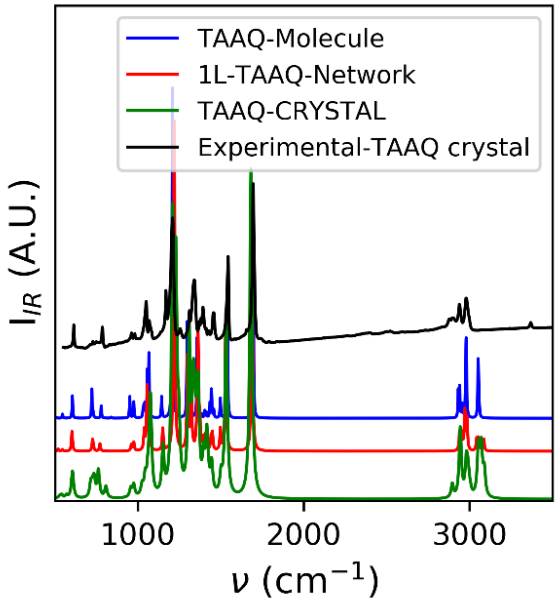

Figure 6.7: The infrared spectrum of TAAQ molecule (black), TAAQ network (red) TAAQ molecular crystal (green) and experimental (black) for TAAQ molecular crystal.

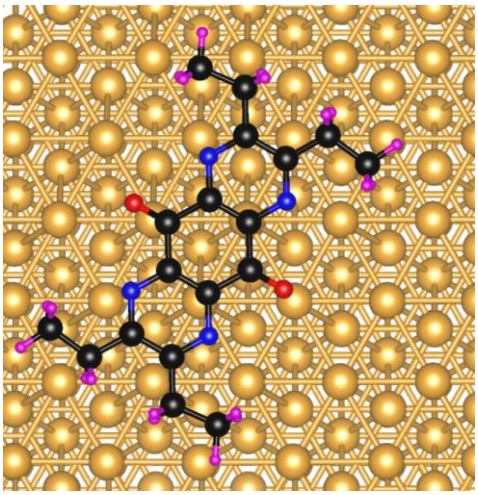

Figure 6.8: Top view of monolayer TAAQ molecule on Au111. The gold balls represent Au, black balls represent C, blue balls represent N and magenta balls represent H atoms, respectively.

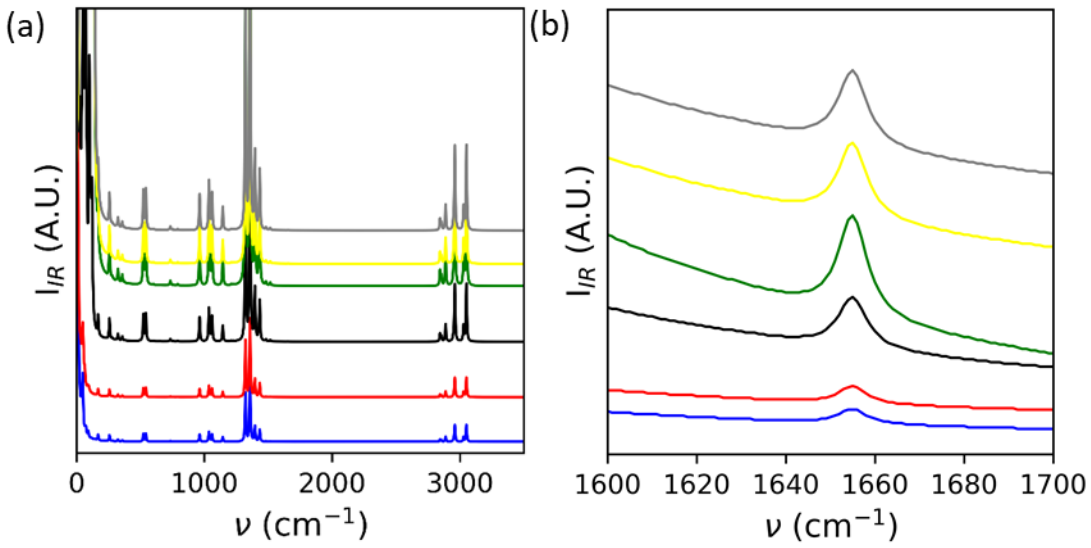

Figure 6.9: Calculated IR spectrum of TAAQ molecule on Au(111) support (a) and the zoom of C=O stretch mode in (b). The calculations are split (details in text). The blue line shows the IR of TAAQ molecule only, red color line represents the IR for TAAQ molecule with 1st layer of Au(111) support, black color represent IR of TAAQ molecule with top two layers of Au(111) support, green color represents the IR of TAAQ molecule with top three layers of Au(111) support, yellow color represents the IR of TAAQ molecule with top four layers of Au(111) support and gray color represents the IR of TAAQ molecule with all layers of Au(111) support.

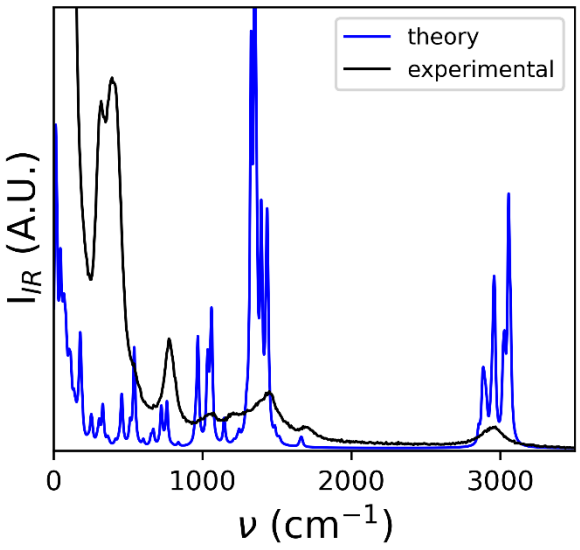

Figure 6.10: Calculated IR spectrum of TAAQ network on Au(111) support.

6.5 Summary

We have demonstrated the complexation between TAAQ ligand and iron. TAAQ functions as a redox-active ligand to form complex metal–organic structures. The TAAQ ligand is designed for greater reductive capacity and more metal binding pockets than are usually employed in metal–organic coordination networks. In the case of complexation with Fe, we find that this results in under-population of the binding pockets, due to the limited reduction capacity of the ligand. Rather than achieving uniform di-nuclear centers in straight coordination chains for which the ligands were designed, the abundance of binding pockets leads to multiple binding motifs with comparable energies and a disordered structure. The calculated IR spectrum of TAAQ gas phase and on support show good agreement with experimental results. We also showed that the effect of Au(111) support on IR spectra of TAAQ can be approximated by taking into account only top layer of Au(111) without losing and quantitative accuracy.

CHAPTER 7: EXCITED STATES IN HYDROGENATED SINGLE-LAYER MoS_2

Our calculations of the excitation spectrum of single-layer MoS_2 at several hydrogen coverages, using a Density-Matrix based Time-Dependent Density-Functional Theory (TDDFT) show that the fully hydrogenated system is metallic, while at lower coverages the spectrum consists of spin-polarized partially filled localized mid-gap states. The calculated absorption spectrum of the system reveals standard excitonic peaks corresponding to the bound valence-band hole and conduction-band electron, as well as excitonic peaks that involve the mid-gap charges. Binding energies of the excitons of the hydrogenated system are found to be relatively large (few tens of meV), making their experimental detection facile and suggesting hydrogenation as a knob for tuning the optical properties of single-layer MoS_2. Importantly, we find hydrogenation to suppress visible light photoluminescence, in agreement with experimental observations. In contrast, both Li and Na atoms transform the system into an n-doped non-magnetic semiconductor that does not allow excitonic states.

7.1 Introduction

Offering versatile electronic and optical properties, two-dimensional (2D) transition metal dichalcogenides (TMDCs) have attracted much interest. They exhibit attractive properties such as strong photoresponse and transition from indirect to direct band gap as the number of atomic layers decreases to one [90-92]. Furthermore, the bandgap of 2D TMDCs may be tuned quantitatively by varying the layer thickness and strain [93,94]. They may also show edge-structure dependent semiconducting-to-metallic transitions [95]. At the same time, adsorption of an alkali metal (K)

atoms has been shown to have significant influence on the catalytic properties of MoS_2 [96-99], while the exposure of Na to the MoS_2(0001) surface leads to expected n-type dopant shifts of the bands [100-102], which is to be contrasted with the effect of Co atoms on the electronic structure of WSe_2(0001) [102]. While Na atoms act as electron donors in MoS_2, Co atoms serve as electron acceptors (p-type) in WSe_2. These dopants dramatically modify the electronic structure of these materials, and thus their excitation spectrum (for example, by enhancing plasmonic properties through increased density of carriers). Hydrogenation was found to affect the structural, electronic, optical, magnetic and catalytic properties of 2D TMDCs [103]. It could also change the intrinsic n-doping to p-doping, at room temperature, and completely saturate sulfur vacancies in MoS_2 flakes [104]. Hydrogenation may also lead to a quench of the photoluminescence (PL) of single-layer MoS_2 [105]. The above properties are, of course, temperature dependent. For example, a 500 °C heat treatment restores the electronic and optical properties of the system by stimulating desorption of the hydrogen atoms [106]. Other 2D TMDCs, such as monolayer $MoSe_2$, have also responded to hydrogenation via a plasma treatment [106] inducing a charge transfer from hydrogen to $MoSe_2$ which changes the electronic and excitation properties of the system, resulting in a shift of the PL peak and a ~3-fold decrease of the electron mobility.

Significant advances in understanding some of the above properties of hydrogenated monolayer MoS_2 have been made through application of density functional theory (DFT). It was shown that electronic structure and magnetism of hydrogenated monolayer MoS_2 can be modified under uniaxial tensile strain [107]. Furthermore, magnetic properties of monolayer MoS_2 were found to depend strongly on hydrogen concentration and adsorption sites: adsorption at the center of the hexagonal ring with a relatively high concentration of H atoms produces itinerant ferromagnetism,

while adsorption on sulfur atoms with a low concentration of H atoms yields flat-band ferromagnetism [108]. Interestingly, in the latter case, it was found that the electrons are distributed on H and neighbor Mo and S atoms, while in the non-magnetic case they are mostly localized on the Mo atoms neighboring hydrogen. Another consequential finding is that hydrogenation significantly reduces diffusion barriers for Ni and S complexes and helps build stable conducting nanorods on MoS_2 [109]. DFT calculations have also shown [110] that the interaction of H with MoS_2 becomes more favorable with increasing hydrogen concentration. Absorption of a single H per 4×4×1 cell produces a mid-gap state approaching the Fermi level, and hence significantly increases the n-type carrier concentration and as result the system's electrical conductivity.

The interplay of spin-valley coupling, orbital physics, and magnetic anisotropy in several 2D TMDCs with a single adsorbed magnetic transition-metal (TM) atom was exploited by Shao *et al*. [111] to demonstrate that the spin-flip scattering rates in the systems depend strongly on the involved orbitals, since orbital selection rules define the kinetic exchange coupling between the adatom and the charge carriers. These findings point to potential spintronic application by tuning magnetic and spin transport properties via doping with TM adatoms. Quite remarkably, it was shown theoretically that another hydrogenated 2D material – single layer *h*-BN – demonstrates an oscillatory dependence of the bandgap on hydrogen concentration, making it possible to tune absorptive and emissive properties of the system [112]. DFT studies of adsorptive properties of monolayer TMDCs [113] have also shown that surface and interlaminar hydrogenations have different effects on electronic properties: in several systems surface hydrogenation induces magnetism and reduces the bandgap, but does not modify the semiconducting character of the monolayer, while interlaminar hydrogenation induces a semiconductor-to-metal transition.

Moreover, it has been shown theoretically that, akin to graphene, hydrogenation might significantly enhance the critical temperature and superconducting properties of 2D materials [114,115]. These results demonstrate a potential of hydrogen functionalization of TMDCs for use in electronic and magnetic devices.

In the experimental and theoretical results described above the excitation spectrum of hydrogenated MoS_2 plays a very important role. It is thus somewhat surprising that there is a lack of an *ab initio* study of the effect hydrogenation on the excitation spectrum of MoS_2. To provide this much needed microscopic understanding, we have performed a combined DFT and TDDFT study of the excitation spectrum of hydrogenated single-layer MoS_2 by paying special attention to changes in the excitonic properties as a function of coverage of hydrogen atoms. In addition, we analyze the electronic properties of single-layer MoS_2 under adsorption of two other atoms with a single s electron in the outer shell - Li and Na. As we shall see, only H as an adsorbate creates non-hybridized and well-isolated hydrogenic states within the bandgap, bringing forth new excitonic states that enrich the excitonic properties of pristine single-layer MoS_2.

7.2 Computational Details

We performed calculations based on DFT with the plane-wave and pseudopotential methods as implemented in the Quantum Espresso package [66]. We treated exchange correlation effects within the generalized gradient approximation in the form developed by Perdew–Burke–Ernzerhof (GGA-PBE) [15] and the local density approximation (LDA), as parameterized by Perdew and Zunger (LDA-PZ) [12]. We used ultrasoft pseudopotentials to describe the core-valence electron interactions. For spin-orbit coupling (SOC), we treated the core electrons fully relativistically. We

applied kinetic energy cutoffs of 60 Ry and 360 Ry, respectively, for calculations of valence electron wave functions and electron density. We used a 16×16×1, 6×6×1, 4×4×1 Monckhorst-Pack (MP) grid for k-point sampling of the Brillioun zone to generate a fine reciprocal-space grid for the 1×1×1, 3×3×1 and 5×5×1 cells, respectively. We optimized atomic positions and lattice parameters, until the residual forces converged to less than 0.01 eV/Å.

To calculate the excitonic binding energies we used the Density-Matrix TDDFT approach [33,38], in which the Kohn-Sham equation $\mathrm{i}\frac{\partial \Psi_{\vec{k}}(\vec{\mathrm{r}},\mathrm{t})}{\partial \mathrm{t}} = \mathrm{H}(\vec{\mathrm{r}},\mathrm{t})\Psi_{\vec{k}}(\vec{\mathrm{r}},\mathrm{t})$ is solved by using the following ansatz for the wavefunction: $\Psi_{\vec{k}}(\vec{\mathrm{r}},\mathrm{t}) = \sum_{\mathrm{l}} \mathrm{c}_{\vec{\mathrm{k}}}^{\mathrm{l}}(\mathrm{t})\varphi_{\vec{\mathrm{k}}}^{0\mathrm{l}}(\vec{\mathrm{r}})$, where $\varphi_{\vec{\mathrm{k}}}^{0\mathrm{l}}(\vec{\mathrm{r}})$ are the static DFT wavefunctions (l is the band index, k is the wave-vector) and $\mathrm{c}_{\vec{\mathrm{k}}}^{\mathrm{l}}(\mathrm{t})$ are their time-dependent coefficients. The sum in the ansatz is over all bands involved into the optical transitions. In this work, we use the two-band approximation which reduces the problem to finding bilinear combination of the c-coefficients that constitute the density matrix: $\rho_{\vec{\mathrm{k}}}^{\mathrm{lm}}(\mathrm{t}) = \mathrm{c}_{\vec{\mathrm{k}}}^{\mathrm{l}}(\mathrm{t})\mathrm{c}_{\vec{\mathrm{k}}}^{\mathrm{m}*}(\mathrm{t})$. Indeed, the elements of the density matrix define practically all properties of the system - the level occupancies (diagonal elements), electronic transitions (polarization), excitons (non-diagonal elements), etc. The density matrix elements satisfy the Liouville equation: $\mathrm{i}\frac{\partial \rho_{\vec{\mathrm{k}}}^{\mathrm{lm}}(\mathrm{t})}{\partial \mathrm{t}} = [\mathrm{H}(\mathrm{t}),\rho(\mathrm{t})]_{\vec{\mathrm{k}}}^{\mathrm{lm}}$, where $\mathrm{H}_{\vec{\mathrm{k}}}^{\mathrm{lm}}(\mathrm{t}) = \int \varphi_{\vec{\mathrm{k}}}^{0\mathrm{l}*}(\vec{\mathrm{r}})\mathrm{H}(\vec{\mathrm{r}},\mathrm{t})\varphi_{\vec{\mathrm{k}}}^{0\mathrm{m}}(\vec{\mathrm{r}})\mathrm{dr}$ are the matrix elements of the Hamiltonian with respect to the static wave functions (Kohn-Sham orbitals). From the valence (v) and conduction (c) bands one can derive the TDDFT Casida equation [116], in the Tamm-Dancoff approximation [117], for $\rho_{\vec{\mathrm{k}}}^{\mathrm{cv}}(\omega)$ that describes exciton states by using the linear form of the Liouville equation[33]:

$$\sum_{\vec{k}'}\left[\left(\varepsilon^{c}_{\vec{k}}-\varepsilon^{v}_{\vec{k}}\right)\delta_{\vec{k}\vec{k}'}+F_{\vec{k}\vec{k}'}\right]\rho^{cv}_{n,\vec{k}'}(\omega)=E_n\rho^{cv}_{n,\vec{k}'} \quad (7.1)$$

where $\varepsilon^{c}_{\vec{k}}$ and $\varepsilon^{v}_{\vec{k}}$ are the free electron and hole energies at the specific wave vector (providing their energy dispersion), $\rho^{cv}_{n,\vec{k}'}(\omega)$ is the N_k-component of the polarization vector (N_k is the number of points in momentum space), n numbers the excited state, and $F_{\vec{k}\vec{k}'}$ is the TDDFT effective electron-hole interaction:

$$F_{\vec{k}\vec{k}'}=\int d\vec{r}_1 d\vec{r}_2 \varphi^{0c*}_{\vec{k}}(\vec{r}_1)\varphi^{0v}_{k}(\vec{r}_1)f_{XC}(\vec{r}_1,\vec{r}_2)\varphi^{0v*}_{\vec{k}'}(\vec{r}_2)\varphi^{0c}_{\vec{k}'}(\vec{r}_2) \quad (7.2)$$

defined by the exchange-correlation (XC) kernel $f_{XC}(\vec{r}_1,\vec{r}_2)$. To obtain the excitonic binding energies, we solve Eq. (1) using both the long-range (LR) and Slater XC kernels[38], as implemented in the BEE code that we have developed [33,40]. We use periodic boundary conditions along x and y-axis and added a 15 Å vacuum along z-axis to eliminate the interaction between the model 2D system and its periodic images. To simulate the system with different concentrations of H, Li and Na coverage we used 1×1×1, 3×3×1, and 5×5×1 size supercells, which gave us three adsorbate coverages - full, 1/9, and 1/25, respectively.

The LDA-PZ eigenenergies and $\varepsilon^{a}_{\vec{k}}$ and eigenfunctions $\varphi^{0a}_{\vec{k}}(\vec{r})$ are used to construct and solve the exciton eigenenergy equation (Eq. 7.1). The solution of Eq.(1) was obtained for the k-point set for the irreducible Brillouin zone. An approach similar to the above when applied to calculate the exciton and trion binding energies in several TMDCs produced results in reasonable agreement with experimental observations [32].

Once the electronic spectrum and the exciton eigenenergies E_n and the corresponding (N_k-component) eigenvectors $\rho^{cv}_{n,\vec{k}}$ were found by solving Eq. (7.1), we calculated the absorption spectrum in the usual manner:

$$A(\omega) = -\mathrm{Im}\frac{1}{\pi}\sum_n \frac{f_n}{\omega - E_n + i\delta}. \qquad (7.3)$$

In Eq. (7.3) the summation is performed over excited states n between the initial state valence $-$ band and final conduction $-$ band states; f_n is the oscillator strength of the transition [116,118]:

$$f_n = \frac{2}{3}E_n\left|\vec{d}_n\right|^2, \qquad (7.4)$$

where

$$\vec{d}_n = \langle 0|\vec{r}|n\rangle = \sum_{\vec{k}}\sqrt{\frac{2E_n^0}{E_n}}\rho^{cv}_{n,\vec{k}}\ \ \vec{d}^{vc}_k \equiv \sum_{\vec{k}}\sqrt{\frac{2E_n^0}{E_n}}\rho^{cv}_{n,\vec{k}}\ \left\langle \varphi^{0v}_k(\vec{r})\middle|\vec{r}\middle|\varphi^{0c}_k(\vec{r})\right\rangle \qquad (7.5)$$

is the transition dipole moment from the ground (0) to the excited state n and E_n^0 and E_n are, respectively, the energies the excited state calculated within DFT and TDDFT, respectively. The summation in Eq.(7.5) is performed over N_k points the irreducible zone obtained using the grid scheme as described above and corresponds to all possible vertical transitions from the valence to the conduction band. Finally, in Eq.(7.3) we used $\delta = 0.1$. We calculated both TDDFT and DFT absorption spectra (in DFT case one puts in Eq. (7.5) $E_n \to E_n^0$) and for $\rho^{cv}_{n,\vec{k}}$ – the eigenvectors obtained by solving Eq.(7.1) at $F_{\vec{k}\vec{k}'} = 0$).

The emission spectra were obtained from the absorption spectrum $A(\omega)$ by multiplying it by the Planck factor [119]:

$$E(\omega) = \frac{4\pi\omega^4}{e^{\frac{\omega-\Delta}{T}}-1} A(\omega)\,, \qquad (7.6)$$

where Δ is the optical gap in the system (the difference between the energy of lowest-excited state and the energy at the top of valence band) and for temperature we used a representative temperature $T = 0.01eV$ (i.e., of order of room temperature). The spectrum at lower temperatures will be similar, but with more narrow peaks.

To sketch the spatial charge distributions of the electron and the hole comprising the exciton, we used the fact that the excited charge density can be expressed in term of the DFT wave functions and Liouville matrix elements as:

$$\delta n(\vec{r},t) = \sum_{k<k_F} \left(\left|\Psi_{\vec{k}}(\vec{r},t)\right|^2 - \left|\Psi_{\vec{k}}(\vec{r},0)\right|^2 \right)$$

$$= \sum_{k<k_F} \left(\rho_{\vec{k}}^{cv}(t)\varphi_{\vec{k}}^{0c}(\vec{r})\varphi_{\vec{k}}^{0v*}(\vec{r}) + \rho_{\vec{k}}^{vc}(t)\varphi_{\vec{k}}^{0v}(\vec{r})\varphi_{\vec{k}}^{0c*}(\vec{r}) + \rho_{\vec{k}}^{cc}(t)\varphi_{\vec{k}}^{0c}(\vec{r})\varphi_{\vec{k}}^{0c*}(\vec{r}) \right). \qquad (7.7)$$

The first and second terms above correspond to excitation and deexcitation processes, respectively, and the third to the charge in the conduction band. The change of the charge density due to creation of the exciton in state n is:

$$\left|\Psi_{X,n}(r)\right|^2 = \sum_{k<k_F} \rho_{n,\vec{k}}^{cv} \varphi_{\vec{k}}^{0c}(\vec{r})\varphi_{\vec{k}}^{0v*}(\vec{r}). \qquad (7.8)$$

For clarity in visualization of the calculated exciton charge distribution (for n=1), we plotted individual contributions of the electron and hole charges as $\sum_{k<k_F} \rho_{1,\vec{k}}^{cv} \varphi_{\vec{k}}^{0c}(r)\varphi_{\vec{k}}^{0v*}(0)$ and $\sum_{k<k_F} \rho_{1,\vec{k}}^{cv} \varphi_{\vec{k}}^{0c}(0)\varphi_{\vec{k}}^{0v*}(\vec{r})$ (i.e., by fixing the electron or the hole coordinate to be zero), correspondingly.

7.3 Results and Discussion

In this section, we summarize the results of our calculations and their analysis. We first focus on the electronic structure of the pristine and hydrogenated single-layer MoS_2. This is followed by considerations of the binding energy of the excitons in Sec. 7.3.2. In Sec. 7.3.3 we discuss the calculated absorption and emission spectra of the systems of interest which provides a connection with the observed PL data and finally in Sec. 7.3.4, we examine the details of the charge distribution related to the excitons being investigated. Our conclusions are summarized in Sec. 7.4.

7.3.1 Electronic structure of pristine and hydrogenated single-layer MoS_2

For pristine and hydrogenated single layer MoS_2, shown schematically in Figure 7.1, after ionic relaxation, we found the optimized lattice constant to be 3.124 and 3.186 Å, with LDA and PBE, respectively, in a good agreement with previous calculations [120]. The direct bandgap at the K point is ~ 1.78 eV and 1.66 eV for LDA-PZ and GGA-PBE, respectively which is also in agreement with previously reported theoretical [121,122] and experimental values [93,123] (though, in the experimental case the agreement is accidental, since the measured gap is defined by excitonic states). The band structure obtained using the PBE optimized lattice constant of single-layer MoS_2 is shown in Figure 7.2.

Hydrogenation leads to a significant modification of the band structure. We varied the number of H atoms from dilute limit (1/25) to full coverage. For full hydrogen coverage, the system is in the metallic regime as evident from the band structure in Figure 7.3(a) and the projected DOS are shown in Figure 7.4(a). At low coverages (hydrogen concentrations 1/9 and 1/25) the system

remains gapped and the electronic band structure includes partially-occupied spin-polarized mid gap states – occupied spin-up states and empty spin-down states (Figure 7.5).These spin-polarized states are present in the dilute limit of the hydrogen concentration and are stable at least up to concentration ~10%.

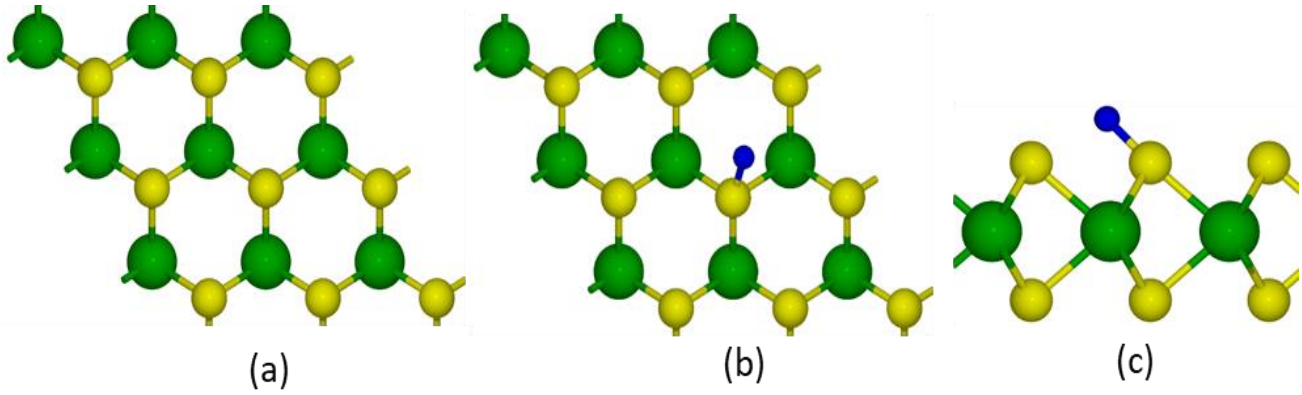

Figure 7.1: Schematic representation of (a) pristine, top view and (b) top view and (c) side view of hydrogenated MoS_2 used in the calculations. Large green balls represent Mo atoms, yellow balls represent S atoms , and blue balls represent H atoms, respectively

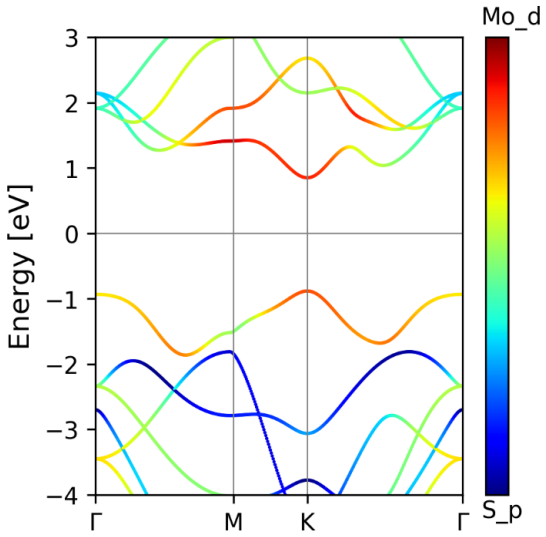

Figure 7.2: Calculated band structure of pristine single-layer MoS_2 obtained by using GGA-PBE. The blue and red colors represent the contribution of the S-p and Mo-d orbitals, respectively.

In the case of fully hydrogenated MoS_2, the system is in a paramagnetic metallic state. One can give the following reasoning for the above differences in the spin polarizations of the systems. While in the unpolarized case of full coverage the hydrogen atoms adsorb "vertically" on S atoms, for partial H coverage, the angle between the H-S bond and MoS_2 plane is smaller than 90 degrees (tilted H-S bonds, see Figure 7.1(c)). This difference in bonding results in different spin-state occupancies. Namely, for full-coverage the H 1s- and S $2p_z$-charges involved in the bonding and antibonding hybridized levels include only the z-components of the orbitals, while in the tilted case the hybridized states include also p_x and p_y orbitals of the sulfur atoms. As a result, there is a lower contribution of z-component of the orbital momentum of the H-S subsystem in the partially-covered case as compared to that of full coverage. Such a decrease of the orbital momentum of the H-S subsystem is compensated by an increase of its spin, i.e. in the partially covered system one obtains hydrogen states with a finite spin.

We have also performed corresponding calculations with adsorbed Li and Na atoms and found the systems to be in a paramagnetic metallic state at all values of adatom concentration (see Figure 7.3(b), 7.3(c), 7.6(a) and 7.6(b), and also Refs.[124,125]). A possible reason for this is the larger radius of the s-orbitals of Li and Na that is responsible for stronger hybridization of these states with those of MoS_2, and hence their delocalization, and diminished effects of spin-polarization.

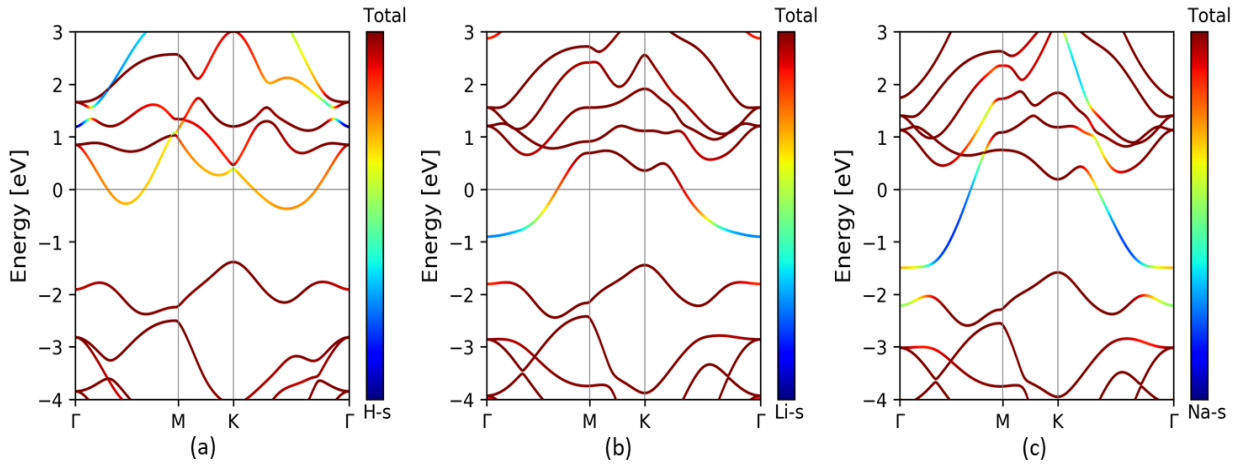

Figure 7.3: Band structure of MoS2 fully covered with (a) hydrogen (b) lithium (c) sodium, calculated using GGA-PBE. The blue shades represent the contribution of the H, Li, Na-s states and red those of Mo and S orbitals. Here and in Figs. 7.5 and 7.6, the horizontal black lines mark the Fermi energy.

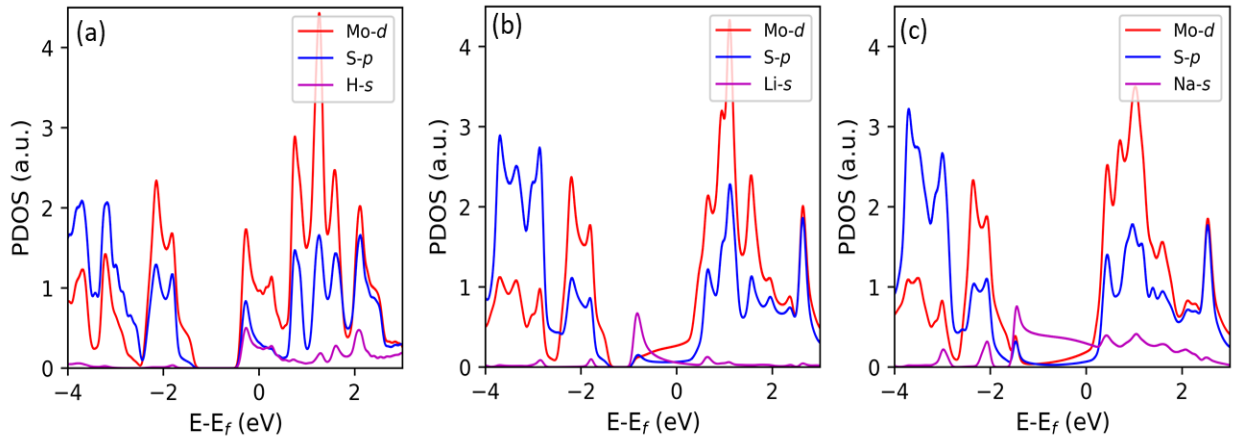

Figure 7.4: Projected density of states (PDOS) of MoS2 fully-covered with (a) hydrogen, (b) lithium and (c) sodium atoms. The results are obtained with GGA-PBE.

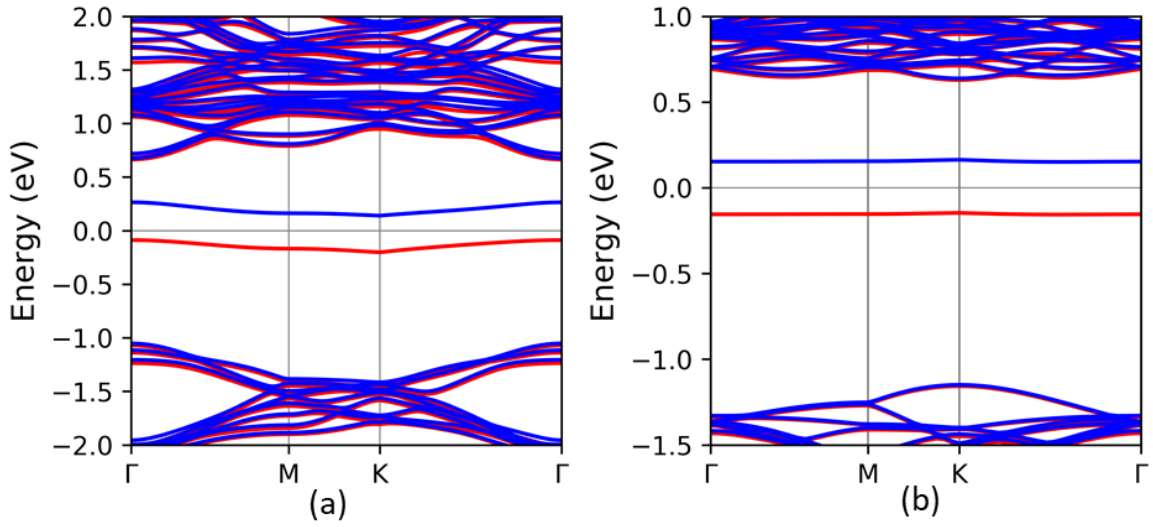

Figure 7.5: Band structure of hydrogenated MoS2 at (a) 1/9 coverage and (b) 1/25 coverage obtained with GGA-PBE. Spin-up and spin-down states are shown in red and blue colors, correspondingly

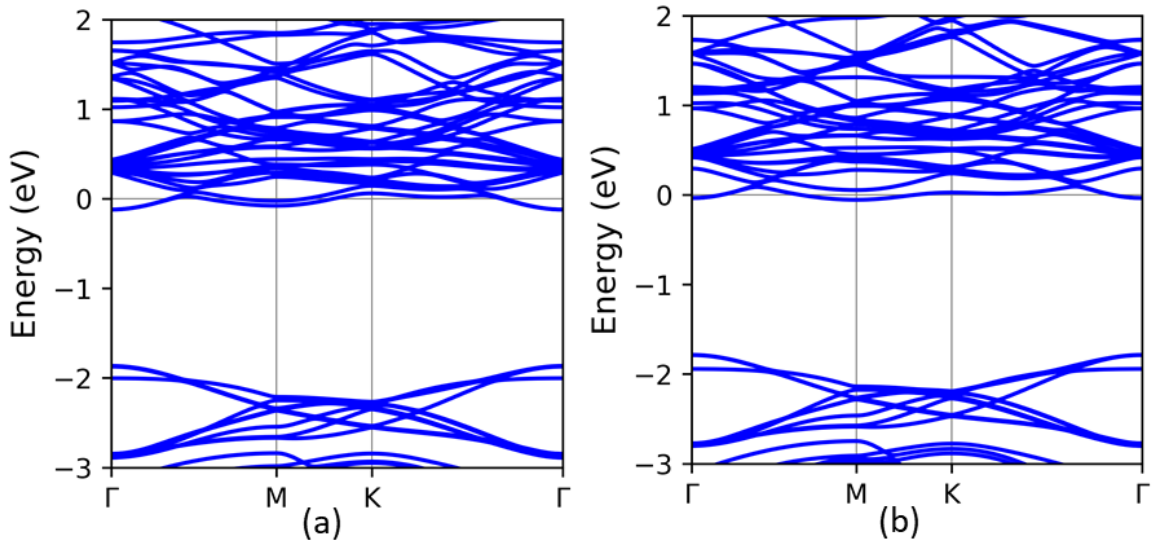

Figure 7.6: The same as in the previous figure in the case of MoS2 for 1/9 coverage by Li (a) and Na (b) atoms.

7.3.2 Binding energies of excitons

In the pristine system, excitons are formed by conduction-band electrons and valence-band holes (Figure. 7.7). The excitonic binding energy ~1.067eV obtained with the Slater XC kernel is of the same order of magnitude (albeit 2 times larger) when compared with experimental data (0.22-0.57eV) [126,127]. In the case of hydrogenated systems, the variety of excitonic states is much richer. As shown schematically in Figure 7.8, one may expect bound states of electrons and holes formed by both MoS_2 and hydrogen bands. Solving Eq.(7.1) for the combinations of electron and hole bands in Figure 7.8, we find that the corresponding binding energies are noteworthy, especially for the lower (1/25) coverage (see Table 7.1).

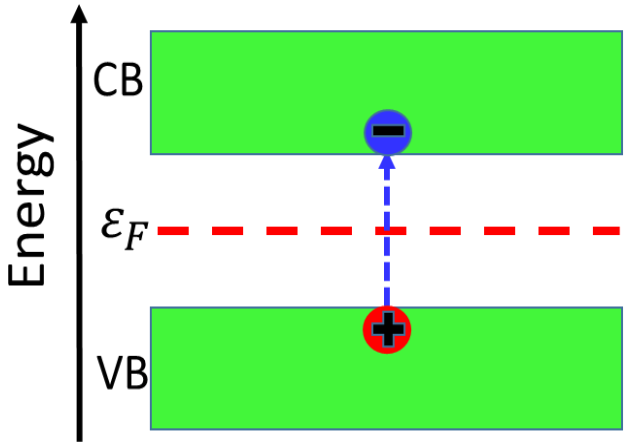

Figure 7.7:Schematic representation of e-h pair forming the exciton in the non-hydrogenated system.

Smaller binding energies of the "standard" B exciton for the higher (1/9) coverage can be traced to enhanced screening effects arising from H electrons, and smaller binding energy of the hydrogen-state exciton, i.e. by hybridization of the "excitonic" hydrogen states with those of the surrounding H atoms resulting in weakened electron-hole interaction. The strongest binding

energy and the strength (i.e. probability of the transition to the corresponding exciton state, defined by Eq. (7.4)) was found for the C exciton, in which both electron and hole are localized on hydrogen atoms. This can be related to the local character of the charges that form the exciton. As mentioned above, the strength of this state decreases with increasing coverage. Another important result is the enhanced strength of the mixed excitonic states A and B at 1/9-coverage due to larger hybridization of the hydrogen and MoS_2 states at higher coverages (when the hydrogen electrons are more spread out over the surface).

Table 7.1: The calculated exciton binding energies in meV and the corresponding dipole strengths, using the BEE code, for two coverages of hydrogen. The different types of excitons (A-D) are defined in Figure. 7.8. The dipole strengths are given in units of the strength.

	1/25 Coverage			1/9 Coverage		
Exciton	Slater	LR	Strength	Slater	LR	Strength
A	-63.708	-61.346	0.05	-2.406	-1.885	5
B	-57.016	-57.009	1	-1.126	-0.679	1
C	-82.592	-97.578	47	-26.771	-40.25	27
D	-57.043	-57.053	0.1	-1.054	-0.834	6

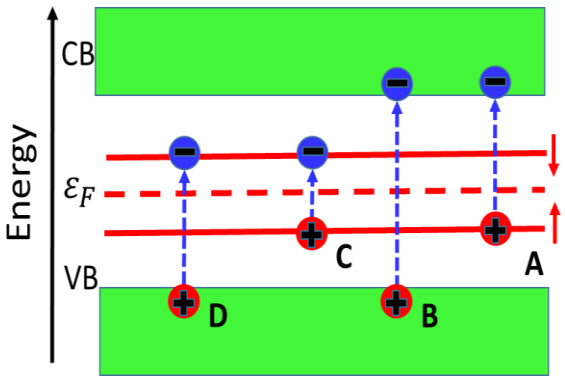

Figure 7.8: Schematic representation of possible excitonic states in the hydrogenated system.

7.3.3 Absorption and emission spectra

In Figure 7.9, we plot the absorption and emission spectra for the pure and the 1/25 hydrogenated MoS_2 in the two-band approximation, as obtained using both DFT and TDDFT (Slater XC kernel), to highlight the difference. (In the hydrogenated case, the bands are the occupied and unoccupied mid-gap hydrogen bands).

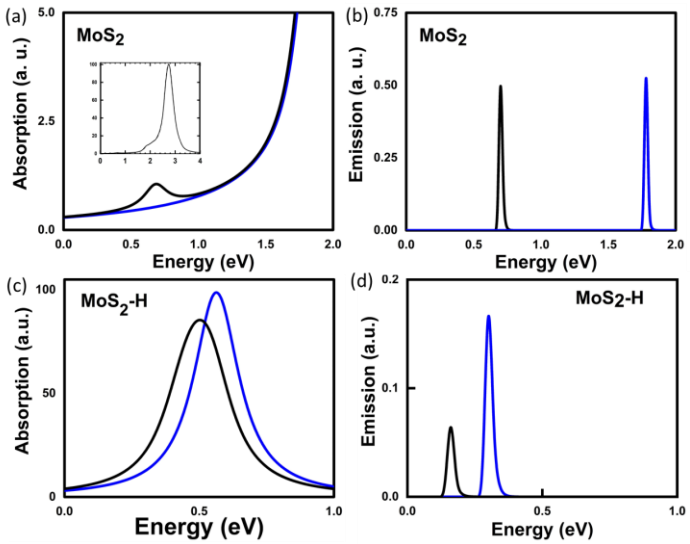

Figure 7.9: Comparison of TDDFT (black curves) and DFT (blue curves) results. Top row: absorption (a) and emission (b) spectra of single-layer MoS_2 . Bottom row: absorption (c) and emission (d) spectra of the MoS2-H system with 1/25 hydrogen coverage.

As expected the DFT optical spectra (Figure 7.9) does not account for the presence of excitons, because of deficiencies in DFT with regard to exchange-correlation effects and because it is a theory suitable mainly for the system in its ground state. Both absorption and emission spectra are missing the excitonic contribution. What is more important here is that the emission spectrum of the hydrogenated system is in the infra-red frequency range (the peak of the spectrum is at ~0.15 eV), while in the pristine system it is in the visible range (taking into account the fact that the DFT electronic bandgap 1.78 eV is ~1eV smaller than the experimental one [126]). The quench of the visible photoluminescence in single-layer MoS_2 after hydrogenation is in agreement with experimental observations [101].

7.3.4 Exciton charge distribution

For visualization of the size of the excitonic states, we have calculated charge distributions for the electron and hole states that form the valence-conduction and hydrogen-band excitons B and C (the "standard" and the strongest-bound excitons, see Figure 7.8) at different coverages. The results shown in Figure 7.10 find the size of the excitons to be several angstroms for both cases. Importantly, the electron and hole that form the hydrogen-band exciton are not localized on the same atom (Figure 7.10(a) and 7.10(b)).

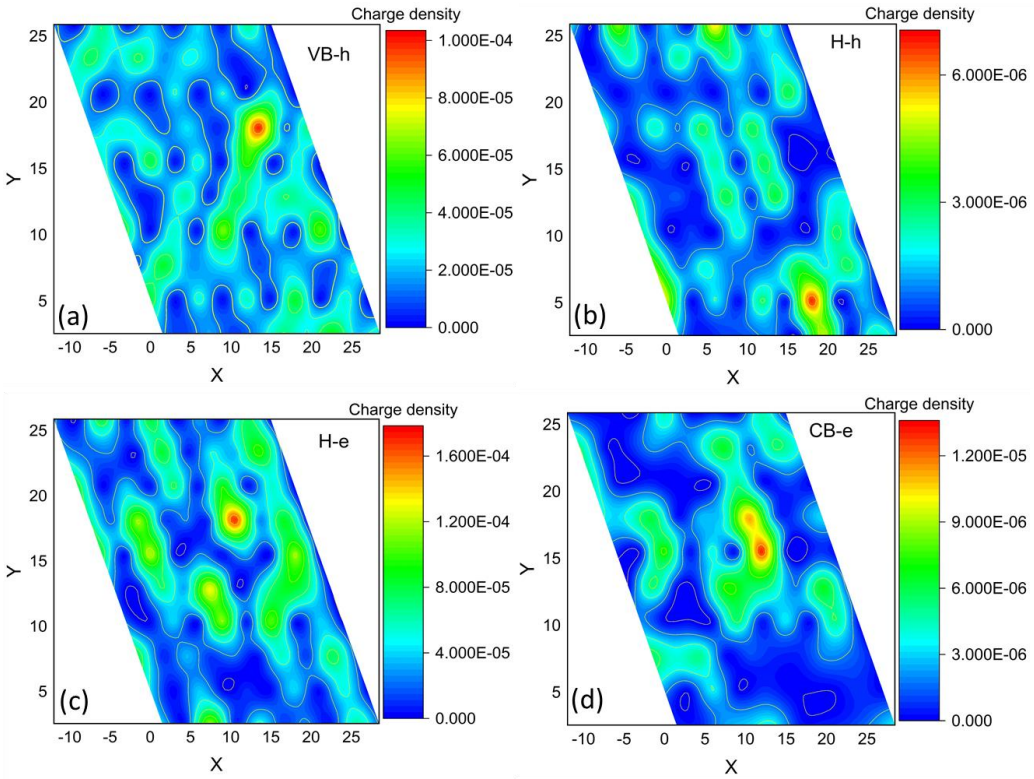

Figure 7.10: The distribution of the hole (h) and electron (e) charges for the lowest energy excitonic states formed by different band charges: (a) top valence band (VB-h), two hydrogen (initially one occupied); (b) H-h and one empty; (c) H-e bands; and (d) bottom conduction band (CB) states for the 1/25 hydrogen density. The charge densities in (b) and (c) correspond to exciton C and those in (a) and (d) to exciton B defined in Fig.7.8. The lateral dimensions of the super cell, X and Y, are in Å.

7.4 Conclusions

We have studied electronic and excitonic properties of hydrogenated single-layer MoS_2, at three coverages, using a combined DFT and TDDFT approach. Our calculations show that for partial hydrogen coverage the system acquires spin-polarized mid gap states, and at full coverage transforms into a paramagnetic metal. The situation is very different with other s-orbital adsorbates - Li and Na – which produce a metallic regime at all coverages. We trace the difference in behavior to a weaker hybridization of H electrons with each other and MoS_2 states, owing to the smaller

radius of the H-s wave function, compared to those of Li and Na, which produces localized mid-gap hydrogen states (flat bands).

We have further demonstrated that these spin-polarized states play a very important role in the absorption and excitonic properties of the system, resulting in a dominating hydrogen excitonic state with infrared absorption and emission, in contrast to the visible spectra exhibited by pure MoS_2. This result is in agreement with experimental data [101]. The existence of a mid-gap excitonic state in a hydrogenated 2D TMDC which has relatively large binding energy and long lifetime (large dipole strength) is an important finding by itself, one that may have applications in energy harvesting technologies.

CHAPTER 8: ULTRAFAST CHARGE DYNAMICS AND PHOTOLUMINESCENCE IN BILAYER MoS_2

Our examination of the interplay of ultrafast charge dynamics and electron-phonon interaction in bilayer MoS_2 provides a microscopic basis for understanding the features (two peaks) in the emission spectrum. We demonstrate that while the initial accumulation of excited charge occurs at and near the Q point of the two-dimensional Brillioun zone, emission takes place predominantly through two pathways: direct charge recombination at the K point and indirect phonon-assisted recombination of electrons at the K valley and holes at Γ hill of the Brillouin zone. Analysis of the wave vector dependencies of the electron-phonon interaction traces the higher energy peak to phonon-assisted relaxation of the excited electrons from the Q to the K valley in the conduction band. Our results thus reveal the importance of ultrafast charge dynamics in understanding photoemissive properties of a few-layer transition-metal dichalcogenide. These calculations are based on time dependent density functional theory in the density matrix formulation.

8.1 Introduction

Transition metal dichalcogenides (TMDCs) form a layered structure with strong in-plane and weak out-of-plane interaction [128,129]. As is now well known, in TMDCs such as MoS_2, $MoSe_2$, WS_2 and WSe_2 the bandgap that changes from indirect to direct as the thickness of the TMDC reduces to that of a single layer, making it suitable for applications in transistors, photodetectors and electroluminescent devices [93,126,129-134]. Single-layers of the above mentioned TMDCs, in particular of MoS_2, have received significant attention also because of their extremely high

photoluminescence (PL), a band gap that lies in the visible spectrum, and strong binding energy of excitons [93,126].

Bilayer molybdenum disulfide is also a system with remarkable characteristics. It has even higher electron mobility and density of states, as compared to single-layer, showing great potential for DC and high-frequency electronic applications [135], and with Bernal stacking, sensitive to electric field. Bilayer MoS_2 also demonstrates strong PL [126,136-139], and similar to the monolayer, it has strongly bound (~100-300 meV) excitonic states [140-143]. However, unlike the single layer, bilayer MoS_2 displays two distinct peaks in the PL: one at an energy below (~1.6 eV) and the other at the same energy (~ 1.9 eV) as that for the single layer [126,141]. While the peak around 1.9 eV, emerging from the direct band gap in single layer MoS_2, remains unchanged for the bilayer, the dependence of the lower energy peak, corresponding to the indirect band gap, has been the subject of several investigations [141,144] in which the nature of stacking and twist angle between the two layers has been varied [141]. These studies confirm the existence of weak interlayer tunnel coupling and strong intralayer electrostatic coupling [144], typical of the TMDCs. They also point to tunability of the interlayer coupling by twisting the layers relative to each other, providing one more avenue for manipulating the optoelectronic properties of few layer MoS_2. Transport [145], emissivity [146], and electronic [147] properties may be tuned by pressure, and Berry curvature, and spin and valley Hall effects, may be manipulated by an applied electric field [148]. With promising optoelectronic applications, the characteristics of the charge carriers and their bound forms, excitons, biexcitons and trions have been examined [149-152]. The role of characteristic vibrational modes [153-155] and electron-phonon coupling [155] in controlling the

optical properties on few layer TMDCs has also been the subject of intense research and debate (see also [143] and references therein).

More germane to this work, analysis of properties at the picosecond timescale of a few-layer MoS_2, showed [156] that nonradiative relaxation mechanisms dominate the carrier dynamics in the system, leading to the speculation that dynamical processes such as valley charge redistribution will come into play before radiative emission. In fact, application of bias voltage was found to drive charges between different band minima [136], resulting in sub-room temperature dissociation of trions which, for the single-layer are stable at room temperature. Although the timescale of involved dynamical processes was not discussed by Kümmell et al. [136], the above results suggest that bias voltage can be a knob for tuning exciton and trion emission through transfer of charge between the layers. In related theoretical work a phenomenological model was proposed [157] to analyze the picosecond valley depolarization dynamics under an external electric-field. Tight binding models have also been applied to examine inter-subband transition rates in e- and h-doped systems [158].

Illustrative as the above experimental and theoretical studies have been in exposing the band structure, vibrational dynamics, and optical properties of 2L MoS_2, they have not tracked the microscopic processes responsible for the emissive properties of 2L MoS_2. In particular, the following questions have not been addressed: What is the effect of electron-phonon coupling on the intervalley charge dynamics at ultrafast time scales? What are the contributions of the different valleys to the emission spectrum? Answers to these questions would provide a systemic understanding of the response of 2L MoS_2 to an ultrafast (femtosecond) pulse, which would in turn help manipulate system properties for potential ultrafast applications. With the above in mind,

we have applied time dependent density functional theory (TDDFT) in the density matrix formalism to examine the temporal evolution of excited charges in the presence of electron-phonon interaction and their impact on the emission spectrum. To isolate the effect of electron-phonon interactions, we have neglected electron-electron and electron-hole interactions (i.e. excitonic effects are ignored), whose inclusion would have small quantitative effect and will not change the main conclusions in this work. We calculate phonon dispersion curves and the electron-phonon coupling constant using density functional perturbation theory (DFPT), within the harmonic approximation. We then include electron-phonon interaction phenomenologically in the Liouville equation via additive many-body scattering terms, in the spirit of semiconductor Bloch equations [152]. The details of computational methods are provided in section 8.2. For completeness, the calculated electronic structure is summarized in section 8.3. Results for the electron-phonon coupling coefficients are discussed in section 8.4, and that for the relaxation of excitations are presented in section 8.5, while the calculated emission spectra are presented in section 8.6. Our conclusions are summarized in section 8.7.

8.2 Theoretical and Computational Methods

8.2.1 Calculations of Electronic Structure

We performed calculations based on DFT with the plane-wave and pseudopotential methods as implemented in the Quantum Espresso package [66]. We treated exchange correlation effects within the generalized gradient approximation in the form of Perdew–Burke–Ernzerhof (GGA-PBE) [15], and used ultrasoft pseudopotentials to describe the core-valence interactions. As already mentioned, 2L MoS_2 is a material with van der Waals inter-layer interaction, whose

contribution we included using the vdW-DF2 method [20]. To mimic single-layer and bilayer, we applied periodic boundary conditions along x and y-axis and added a 15 Å vacuum along z-axis to eliminate any interaction of the system with its periodic image. For calculations of the bulk system we used two MoS_2 formula units (12.37 Å thickness) and applied periodic boundary conditions along all three coordinate axes. Side and top view of the bilayer are presented schematically in Figure 8.1. We described the valence wave functions, and electron density by plane-wave basis sets with kinetic energy cutoffs of 60 Ry and 360 Ry, respectively. We sampled the first Brillouin zone with a 14 × 14 × 14 Monkhorst-Pack grid for the bulk system and 14 × 14 × 1 grid for the single and bilayer systems. We optimized atomic positions and lattice parameters, until the residual forces converged to less than 0.01 eV/Å.

Note that at the outset we include spin-orbit coupling (SOC) by treating the core electrons fully relativistically. These SOC calculations are essential for identifying the splitting at the Brillouin zone edge and at the top of the valence band for the single layer. We thus quantified the splitting (between the spin-up and spin–down bands) of valence band edge at the K point to be 150 meV, in good agreement with the experimental value of 141 meV [159], and verified that they display opposite spin ordering at K and K' points. For the remaining calculations we chose not to distinguish the spins of the excited electrons and thus did not include SOC in the results that are presented below. The effect of SOC on the observables of interest here is negligible, and not worth the extra computational cost.

8.2.1 Calculations of the phonon spectrum and electron-phonon coupling coefficients

We used density functional perturbation theory (DFPT) as implemented in the Quantum Espresso code [66], to first calculate the dispersion of the phonons across the Brillioun zone. For calculations of phonon frequencies, the residual forces were converged to less than 0.0001 eV/Å. Next, we calculated the electron-phonon coupling coefficients using the DFT results for the ground-state atomic and electronic configurations, the corresponding wave functions and band structure, and the calculated phonon dispersion. The quantities of interest are the electron-phonon scattering coefficients given by

$$g_{\vec{q}v}(\mathrm{k,i,j}) = \left(\frac{\hbar}{2M\omega_{\vec{q}v}}\right)^{1/2} \left\langle \psi^{i}_{\vec{k}} \middle| \frac{dV_{SCF}}{d\hat{u}_{\vec{q}v}} . \hat{\epsilon}_{\vec{q}v} \middle| \psi^{j}_{\vec{k}+\vec{q}} \right\rangle \qquad (8.1)$$

which correspond to the scattering of electron from state i (momentum $\vec{k}$) to state j (momentum $\vec{k}+\vec{q}$) due to absorption (emission) of phonon with mode index v and momentum $\vec{q}(-\vec{q})$. In Eq. (8.1) M is atomic mass; $\psi^{i}_{\vec{k}}$ and $\psi^{j}_{\vec{k}+\vec{q}}$ are the electronic wavefunctions for the initial and final states, respectively; $\frac{dV_{SCF}}{d\hat{u}_{\vec{q}v}}$ is the gradient of the self-consistent potential with respect to the atomic displacements induced by the phonon mode ($\vec{q}$,v) with frequency $\omega_{\vec{q}v}$ and polarization vector $\hat{\epsilon}_{\vec{q}v}$. With the above definition of $g_{\vec{q}\nu}(\vec{k},\mathrm{i,j})$, one can obtain the phonon line widths:

$$\gamma_{\vec{q}\nu} = 2\pi\omega_{\vec{k}\nu} \sum_{\mathrm{i,j}} \int \frac{d^3k}{\Omega_{BZ}} \left| g_{\vec{q}\nu}(\vec{k},\mathrm{i,j}) \right|^2 \delta(\varepsilon^{i}_{\vec{q}} - \varepsilon_F) \delta\left(\varepsilon^{j}_{\vec{k}+\vec{q}} - \varepsilon_F\right), \qquad (8.2)$$

where Ω_{BZ} is the volume of the first BZ, $\varepsilon^{i}_{\vec{q}}$ is the energy of the electron in the state (band) i and with momentum $\vec{q}$, and ε_F is the Fermi energy. This brings us to the electron-phonon coupling constant for the corresponding phonon mode ν with the wave vector q:

$$\lambda_{\vec{q}\nu} = \frac{\gamma_{\vec{q}\nu}}{\pi\hbar N(\varepsilon_F)\omega^2_{\vec{q}\nu}} \quad (8.3)$$

where $N(\varepsilon_F)$ is the electron DOS at the Fermi level. Using the results for the coupling constant (8.3) and phonon dispersion ω_{qv}, one can obtain the isotropic Eliashberg spectral function:

$$\alpha^2F(\omega) = \frac{1}{2}\sum_\nu \int \frac{d^3q}{\Omega_{BZ}} \omega_{\vec{q}\nu}\lambda_{\vec{q}\nu}\delta\left(\omega - \omega_{\vec{q}\nu}\right). \quad (8.4)$$

8.2.2 Time dependent excited state charge densities and emission spectra

Input from above DFT calculations form the basis for the code based on Density-Matrix Time Dependent Density Functional Theory (DM -TDDFT) [33,40] that we used to calculate excited state charge densities and the emission spectrum. However, as mentioned above the exchange-correlation kernel was set to zero. Details of the calculations of the time-dependence of the excited charge density may be found in the APPENDIX A and in Ref [160] (in which the formalism is given for the more general spin-polarized case).

To study the effect of electron-phonon coupling on excited-charge dynamics we solved the density-matrix Liouville equation with the scattering term (Bloch equations for semiconductors):

$$\frac{\partial\rho_k^{lm}(t)}{\partial t} = [H,\rho]_K^{lm}(t) \equiv \sum_n \left(H_k^{ln}(t)\rho_k^{nm}(t) - \rho_k^{ln}(t)H_k^{nm}(t)\right) + \left(\frac{\partial\rho_k^{lm}}{\partial t}\right)_{scatt}, \quad (8.5)$$

where

$$H_k^{ml}(t) = \int \psi_k^{m*}(r)\hat{H}(r,t)\psi_k^l(r)dr \quad (8.6)$$

are the matrix elements of the Kohn-Sham Hamiltonian with respect to the static DFT wave functions, and $\left(\frac{\partial\rho_k^{lm}}{\partial t}\right)_{scatt}$ are the scattering terms whose details are provided in the SI. Recall that the inherent relationship between the wavefunction and density matrices follows from the time

dependent Schrodinger equation $i\frac{\partial\Psi_{\vec{k}}(\vec{r},t)}{\partial t} = H(\vec{r},t)\Psi_{\vec{k}}(\vec{r},t)$ when one uses the ansatz $\Psi_{\vec{k}}(\vec{r},t) = \sum_l c_{\vec{k}}^l(t)\psi_{\vec{k}}^l(\vec{r})$, where $\psi_{\vec{k}}^l(\vec{r})$ and $c_{\vec{k}}^l(t)$ are the static DFT wavefunctions and time-dependent coefficients, respectively (l is the band index, k is the wave-vector). the problem then reduces to finding the coefficients $c_{\vec{k}}^l(t)$, or their bilinear combination $\rho_{\vec{k}}^{lm}(t) = c_{\vec{k}}^l(t)c_{\vec{k}}^{m*}(t)$, the density matrices, which satisfy the Liouville equation.

The strength of the transition dipoles corresponding to the photon-induced electronic transitions was calculated from the dipole moment $\vec{d}_{\vec{k}}^{lm}$:

$$\left|\vec{d}_{\vec{k}}^{lm}\right|^2 = \left|e\int \psi_{\vec{k}}^{l*}(\vec{r})\vec{r}\psi_{\vec{k}}^{m}(\vec{r})dr\right|^2. \quad (8.7)$$

The electron-phonon coupling terms defined in Eqs. (8.1) - (8.3) were used to calculate the scattering terms in the TDDFT Bloch equations from the many-body Bloch equations derived for the electron-phonon part of the Hamiltonian $H_{e-ph} = \sum_{l,\vec{k},\vec{q},\nu}\hbar g_{\vec{q}\nu}a_{\vec{k}+\vec{q}}^{l+}a_{\vec{k}}^{l}\left(b_{\vec{q}}^{\nu} + b_{-\vec{q}}^{\nu+}\right)$ (a and b are the fermion and phonon operators, correspondingly, l and ν are the electron and the phonon band indices and $\vec{k},\vec{q}$ are momenta. For more details, we refer the reader to the SI and to Ref. [152].

We next calculated the absorption spectrum: $A(\omega) = \frac{\omega}{n_b c}\mathrm{Im}[\epsilon_{mac}(\omega)]$, where c is speed of light, n_b is the background refractive index, and

$$\epsilon_{mac}(\omega) = 1 - 4\pi\chi_{KS}\left(\vec{k}\to 0,\omega\right), \quad (8.8)$$

is the macroscopic dielectric function related to the Kohn-Sham DFT susceptibility χ_{KS} as below:

$$\chi_{KS}(\vec{k},\omega)=\frac{1}{V}\sum_{\vec{k}'}\sum_{j=1}^{\infty}\sum_{l=1}^{\infty}\frac{\left(f^{l}_{\vec{k}+\vec{k}'}-f^{j}_{\vec{k}'}\right)}{\omega+\varepsilon^{j}_{\vec{k}'}-\varepsilon^{l}_{\vec{k}+\vec{k}'}+i\delta}\int d^{3}r\psi^{j*}_{\vec{k}'}(\vec{r})\vec{r}\psi^{l}_{\vec{k}+\vec{k}'}(\vec{r})$$

$$\times\int d^{3}r'\psi^{l*}_{\vec{k}+\vec{k}'}(\vec{r}')\vec{r}'\psi^{j}_{\vec{k}+\vec{k}'}(\vec{r}'). \qquad (8.9)$$

In Eq. (8.9), $\varepsilon^{l}_{\vec{k}}$ and $\psi^{l}_{\vec{k}}(\vec{r})$ are the Kohn-Sham DFT eigenenergies and eigenfunctions, $f^{l}_{\vec{k}}$ is the Fermi factor for the corresponding DFT state; and j and l are the (valence and conduction) band indices. In the results below we have included two valence and two conduction bands in the summations in Eq. (8.9). Further details may be found in Ref [38].

The emission spectrum is then obtained by simply multiplying the absorption spectrum $A(\omega)$ by the Planck factor [161]:

$$E(\omega)=\frac{4\pi\omega^{4}}{e^{\frac{\omega-\Delta}{T}}-1}A(\omega), \qquad (8.10)$$

where Δ is the optical gap in the system and the temperature is taken to be $T=0.01\text{eV}$, a value of order of room temperature. Furthermore, we have incorporated the nonequilibrium excited charge density in the calculation of the emission spectrum. This is accomplished by multiplying the expression on the right-hand side of Eq. (8.10) by the total excited state charge density, at the time of interest, with energy $\hbar\omega$ (at 400 fs in Figures 8.5(a) and 8.5(b) below). The rationale for doing so follows from the physics of lasers [162]: the probability of emission from the state with given energy is proportional to the number of excited atoms that have this energy.

8.3 Electronic Structure of bilayer MoS_2

In these single-layer TMDCs, the crystal structure is determined by just the lattice constant 'a'. Our PBE calculations for the lattice constants for the bulk, bilayer, and single-layer MoS_2 are 3.173 Å, 3.172 Å, and 3.170 Å, respectively. Using these optimized lattice constants, we have calculated the electronic band structure of bulk, bilayer, and single-layer MoS_2, along the lines connecting high-symmetry points of the Brillouin zone (BZ), which are displayed in Figure 8.2 .

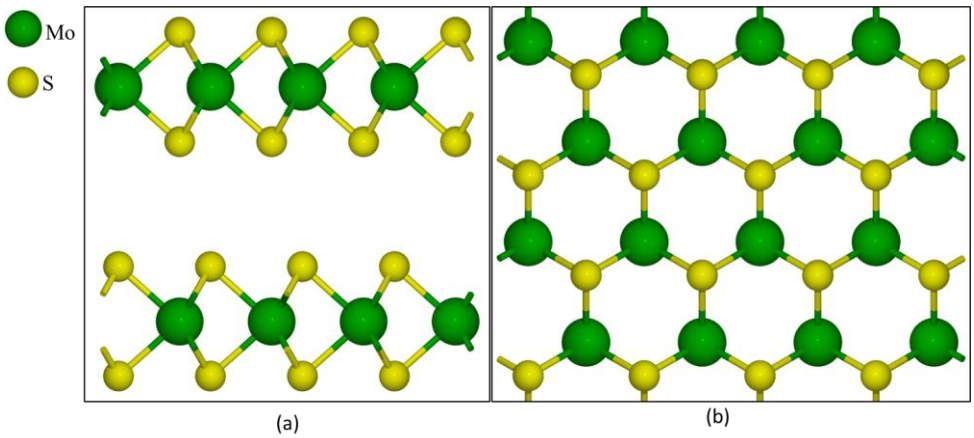

Figure 8.1: Schematic representation of bilayer MoS_2: (a) side view and (b) top view

The calculated band structure of all three systems (Figure 8.2) are in good agreement with previous reports[163-166]. Our calculated electronic density of states (DOS) and the projected density of states (PDOS) on Mo-*d* and S-*p* orbitals for these three systems presented in Figure 8.3, show that the top of valence band and bottom of conduction band are contributed mainly by Mo-*d* orbitals, with a strong hybridization of Mo-*d* and S-*p* orbitals. The valence band tail in PDOS of bulk systems diminishes in case of bilayer and ultimately vanished in case of the single layer. This is because the valence band edge at Γ moves toward lower energy in case of bilayer and single layer, compared to that in the bulk, as we can see in Figure 8.2 . The band structures also show

that bulk and bilayer MoS_2 are indirect band-gap semiconductors with the valence band maximum (VBMAX) and conduction band minimum (CBMIN) located at the Γ and Q points of the BZ, respectively.

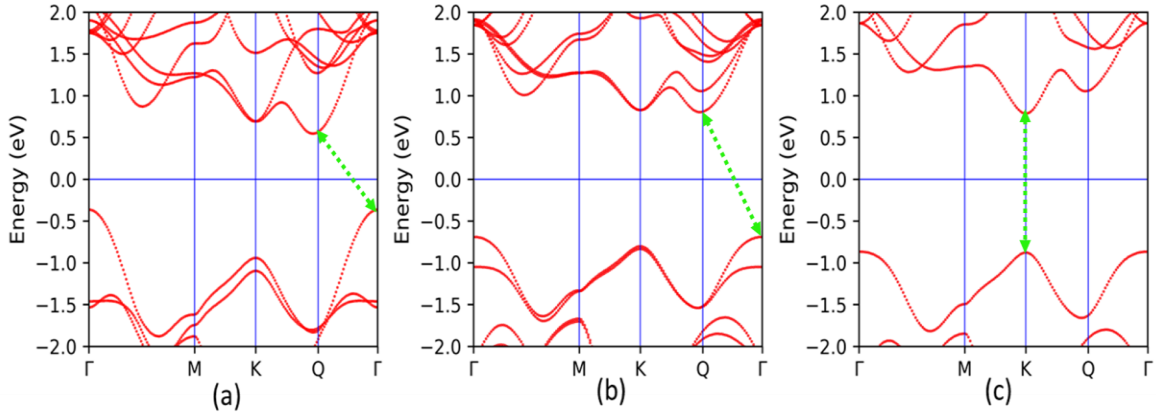

Figure 8.2: Band structure of (a) bulk (b) bilayer (c) and single-layer MoS_2. Fermi level (horizontal blue line) is set to zero. The green dotted line shows the indirect gap for both the bulk and bilayer, and direct band gap for single-layer cases

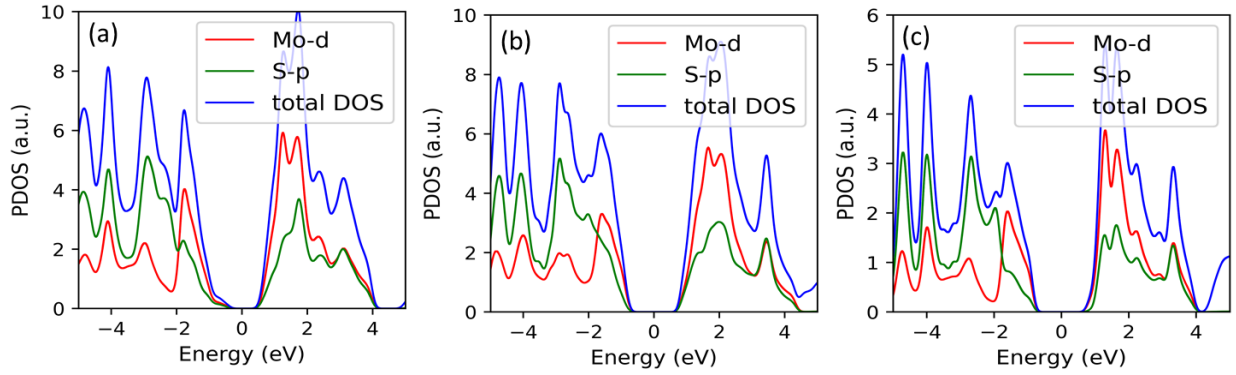

Figure 8.3: Total and Projected Density of States of (a) bulk, (b) bilayer and (c) single-layer MoS_2. The blue lines represent total density of states; green and red lines represent the projected density of states of S-p and Mo-d orbitals, respectively.

We also note that it is evident in Figure 8.2 , that the conduction band valley at the Q point starts shifting toward higher energy and the valence band hill at Γ point shifts toward lower energy, as

the thickness of the model system changes from bulk to two layers, while the valence band hill at the K point shifts toward higher energy. Note that for the single layer, the VBMAX and CBMIN are both located at the K point. From our calculations we find that the direct K→K gap for single-layer MoS_2 is 1.66 eV and the indirect Γ→ Q gaps for bulk and bilayer MoS_2 are 0.92 and 1.49 eV, respectively.

8.4 Electron-Phonon Coupling Coefficients for Bilayer MoS_2

We used the relaxed structure of bilayer MoS_2 presented above to calculate phonon dispersion curves for bilayer MoS_2 which are plotted in Figure 8.4 (a).

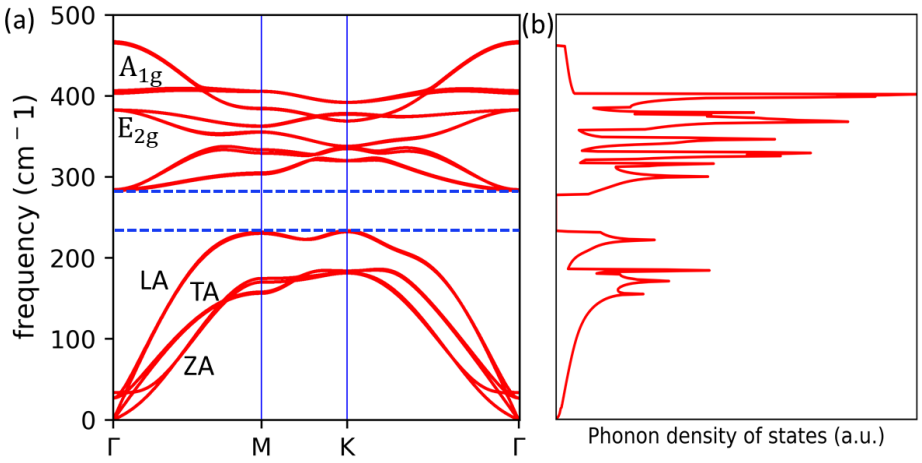

Figure 8.4: Phonon dispersion for bilayer MoS_2 (a) and phonon density of states (b) The horizontal dashed lines in (a) show the separation/gap of low frequency and high frequency phonon branches.

The features seen in Figure 8.4 (a) are in general agreement with previous reports [155,167,168]. In bilayer MoS_2, there are three acoustic branches: one longitudinal acoustic (LA), one transverse acoustic (TA), and one flexural acoustic (ZA). The LA mode reaches a value of 235 cm^{-1} at M point, and 245 cm^{-1} at K point. We note that there are no degeneracies at the M and K points, and

the two crossings of the LA and TA branches just before and after the M point. The high-frequency optical modes are separated from the low-frequency modes by a gap of 41 cm^{-1}. We have drawn two horizontal blue dashed lines in the dispersion curve (Figure 8.4 (a)) to show the gap. In Figure 8.4 (a) the in-plane and out of plane vibrational modes are represented by E_{2g} and A_{1g}. with ω_{qv} from the calculated phonon dispersion curves in Figure 8.4, and using Eq.(8.1) to (8.3) above, we calculated the phonon band index-dependent phonon linewidths and electron-phonon coupling coefficients that are summarized in Figure 8.5.

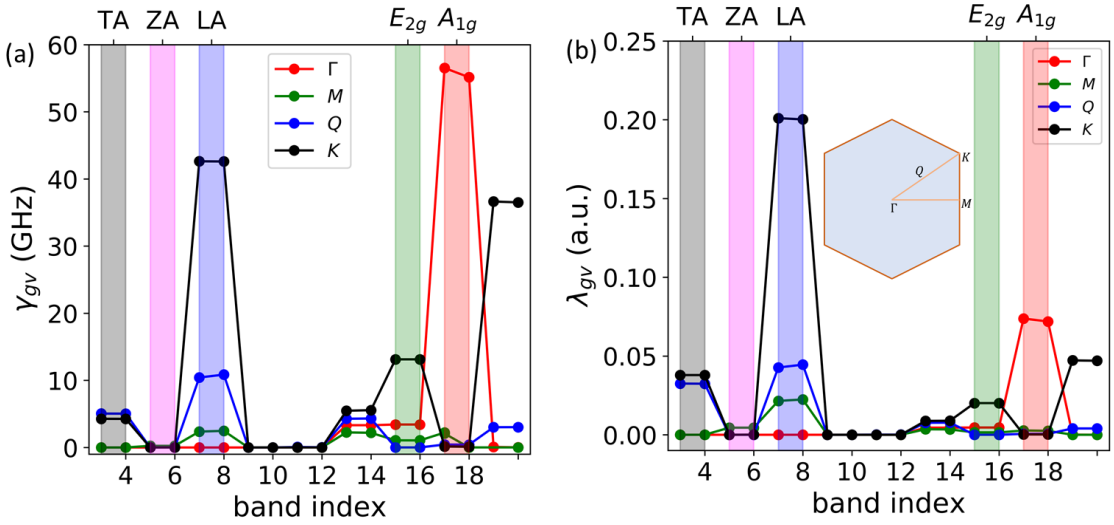

Figure 8.5: Calculated band index dependent phonon linewidths (a) and electron-phonon coupling constant (b) for the phonon bands at the special k-points of the two dimensional Brillioun zone (insets), for bilayer MoS_2.

The largest contribution to the linewidth comes from the A_{1g} mode at the Γ point. As for the electron-phonon coupling, it is the LA mode at the K point that is most dominant, this is followed by the contribution from A_{1g} mode at the Γ point. From the results in Figure 8.5 (a), we can also infer the lifetimes of the contributing phonon modes are longer than 16 ps, which means that their

effect would be very meaningful in our analysis charge dynamics of the system in the hundreds of femtosecond time scale. Our results for the total and band-resolved $\alpha^2 F(\omega)$ (Eliashberg function) shown in Figure 8.6 (a) and (b) are reflective of similar trends in the phonon DOS (Figure 8.4 (b)), demonstrating that phonons with energies 350-400 cm^{-1} (43-50 meV) play a dominant dole in the dynamics of the system.

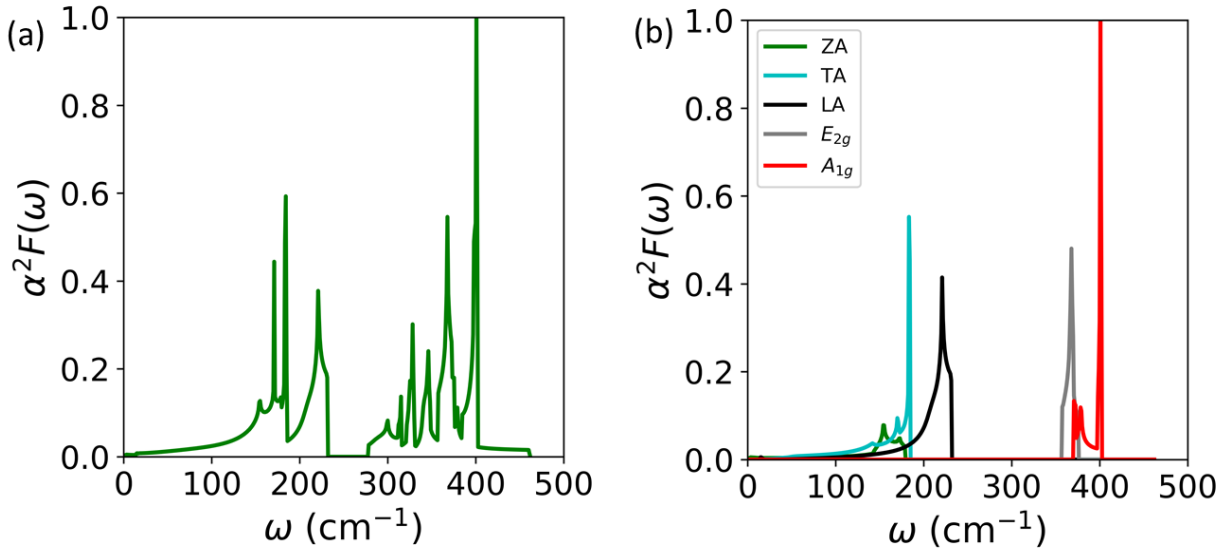

Figure 8.6: Eliashberg spectral function $(\alpha^2 F(\omega))$ for bilayer MoS_2: (a) contribution from all modes, (b) modes resolved contributions.

To compare the phonon properties of bilayer and single-layer MoS_2, in Figure 8.7 we present the results for the phonon linewidths and electron-phonon coupling constants and in Figure 8.8– the results for the Eliashberg function for the single-layer system. From Figure 8.7, it follows that in the single-layer case, the K- and Γ-momenta phonon modes are not dramatically distinguished from the other k-point modes, contrary to the bilayer case. As we show below, a strong electron-phonon coupling at phonon momentum K is responsible for a strong indirect emission in the

bilayer system. Comparison of the Eliashberg functions in the two systems (Figure 8.6, 8.8) shows that while in the bilayer case A_{2g} phonons (frequency ~400cm^{-1}) play dominant role in the coupled electron-phonon system, in the monolayer case TA (~180cm^{-1}) is the dominant phonon band. On the other hand, the combined contribution of the ZO_1 and ZO_2 modes to the Eliashberg function in the single-layer system gives the second sharp peak at ~400cm^{-1}, similar to the case of bilayer.

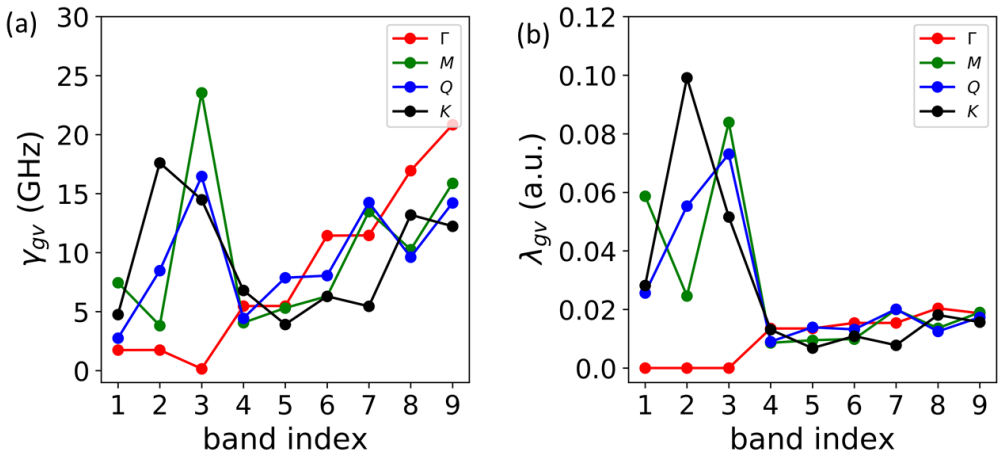

Figure 8.7: Calculated phonon linewidths for single layer MoS_2 (a) and electron-phonon coupling constant (b) for different bands and k-points. In the insets, the used k-points are defined

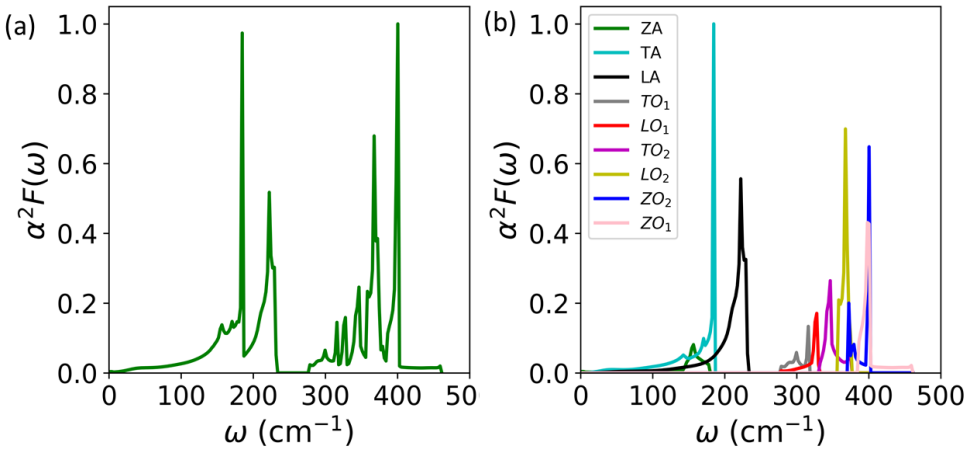

Figure 8.8: Eliashberg spectral function ($\alpha^2F(\omega)$) for single layer MoS_2: (a) contribution from all modes, (b) modes resolved contributions

5. Electron-Phonon Mediated Relaxation of Excitation in Bilayer MoS_2

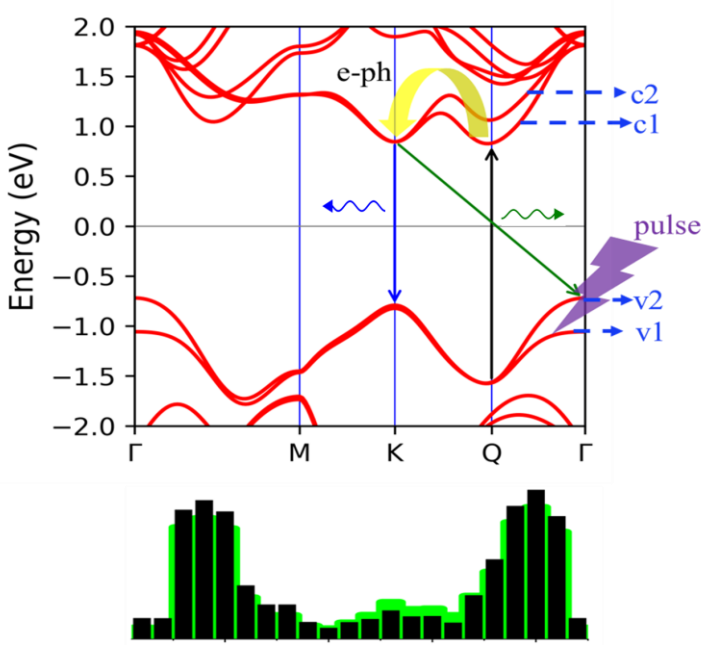

Figure 8.9: Top: Schematic representation of excitation and recombination processes that lead to photoluminescence. Bottom: relative excited charge accumulated initially after the pulse (black) and after dynamics (green) with k-points in the Brillouin zone.

To get a physical insights into the excitation and emission process of the system at hand, we first calculated the momentum-resolved density of the pumped charges excited from the two top valence bands (labeled v1 and v2 in Figure 8.9) to the two lowest conduction bands (labeled c1 and c2 in Figure 8.9) in the case of a 100 fs pulse with an electric field magnitude 1V/Å, using Eq. (8.5) and with no electron-phonon interaction for the set of k-points shown in Figure 8.9. Also, we calculated the excited charge density for the same set of k-points at longer times (400 fs) after the electron-phonon scattering effects are taken into account (see Figure 8.10 and the discussion below). The results for both charge densities are shown in bottom Figure 8.9. The pulse excites the electrons from the valence to the conduction bands through vertical transitions (photon momenta are very small). As one can see from Figure 8.9 (black columns), the amount of the

"pumped" excited charge is maximum between Q and Γ point of the BZ, which can be explained by a combination of two factors: high valence-bands DOS along these k-points (the bands are almost flat) and a relatively shorter separation, between the valence and conduction bands, compared to that at other k-points. The high density of the excited charges in another part of the BZ – between Γ and M points – can be explained similarly. The results for the time dependence of the excited charge density at different k-points that correspond to the total pumped charges in Figure 8.9 are shown in Figure 8.10 (a). We normalized the charge densities at all k-points to the same saturated (after 200 fs) value for a better visualization of their difference once electron-phonon interaction is taken into account. We then calculated the excited state occupancies by including the electron-phonon scattering term in Eq. (8.5). As shown in Figure 8.10 (b), the occupancies at most of the k-points start to decrease after 200 fs, as electron-phonon coupling starts to play a role in scattering electrons out of the Q valley into the K valley. We can see that the originally highest-populated Q-valley gets significantly depopulated with electron-phonon interaction, in contrast to what happens in the K-valley. The "final" excited charge density at different k-points is shown in the bottom of Figure 8.9 (green columns). We also include a schematic representation of the electron relaxation due to electron-phonon interaction in the top panel of Figure 8.9. The energy required to move an electron from Q valley to K valley of conduction band can be estimated by the energy difference of these two valleys, ~ 40 meV. Recall from the analysis of the phonon spectrum that the effective (average) phonon energy is also about 40 meV (see Figure 8.4 (b) for the phonon DOS). Indeed phonons that populate this energy range must be responsible for the inter-valley charge transfer. Thus, we conclude here that electron-phonon coupling is the main source of depopulation of excited state occupancies at points other

than K valley. At the K point, the major contribution to electron-phonon coupling arises from the low frequency longitudinal acoustic modes (see Figure 8.5 (b)) which do not affect the occupancy of the excited state. It is important to note that an inter-valley electron and hole dynamics was reported in work [27] in the case of five-layer MoS_2. Similarly, to our results, the inter-valley transitions happen at a few hundred-fs timescale. However, due to a different band order, transition happen from K- to Q-valley (electrons) and from K- to Γ-valley (holes).

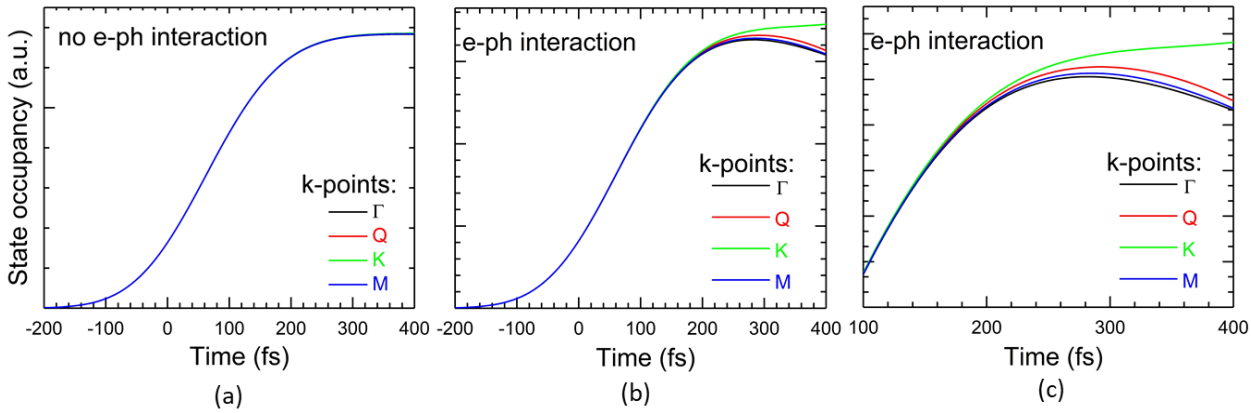

Figure 8.10: The occupancies of conduction band at special k-points (Γ, Q, K and M) of Brillouin zone as a function of time. The state occupancies are plotted for the cases (a) without including electron-phonon interaction and (b) with electron-phonon interactions. In Fig (c) zoomed long-time occupancies from (b) are shown.

8.5 Calculated Emission Spectrum of Bilayer MoS_2

The calculated emission spectra calculated using TDDFT without and with the electron-phonon dynamics taken into account are shown in Figure 8.11 We can see that the spectrum obtained before the electron-phonon scattering-induced charge redistribution (Figure 8.11 (a)) has one dominating peak related to indirect emission attributed to the $K \rightarrow \Gamma$ transitions. The direct K-valley emission is reflected in a relatively weak shoulder in the spectrum. On the other hand, using

TDDFT in the case of re-distributed charges we obtained a two-peak emission spectrum, as shown in Figure 8.11 (b). The lower energy peak corresponds to indirect $K \rightarrow \Gamma$ transition while the peak toward higher energy corresponds to the direct K-valley transition. Transformation of the shoulder into a pronounced peak in the emission is related to an enhanced charge density in the K-valley due to the electron-phonon scattering (bottom Figure 8.9). As it follows from Figure 8.5 (b), the strongest contribution to the electron-phonon scattering comes from the LA phonon bands with momentum K. Thus, the indirect emission peak is formed mostly by electron transitions $K \rightarrow \Gamma$, i.e. from the K-valley in the conduction band that has an extra charge due to phonon-assisted charge transfer from Q to the K valley. Interpreting the emission spectrums as calculated using TDDFT, we note that the emission spectrum as calculated with TDDFT + electron-phonon scattering gives a rather good agreement with experiment regarding the position of the emission peaks found in Ref. [126](Figure. 3) and Ref.[139] (Figure. 6). An extra small peak found in Ref. [126] may come from higher-energy exciton recombination. The difference in the relative magnitude of the peaks in Figure 8.11 (b) are probably the result of the approximation that the probability of the emission transition is proportional to the amount of the excited charge density in the given valley (we take the charge density at maximum time used in the calculations (400 fs, Figure 8.10), which is still a transient time, i.e. the population of the valley can still change during total electron-phonon equilibration. It is important to stress that the emission peaks in this work come from the inter-band recombination of free electrons and holes, not exciton recombination. However, since the exciton binding energies for the different valleys are smaller than the corresponding bandgaps, the two-peak emission spectrum in Figure 8.11 (b) will not change dramatically when the emission is caused by exciton recombination.

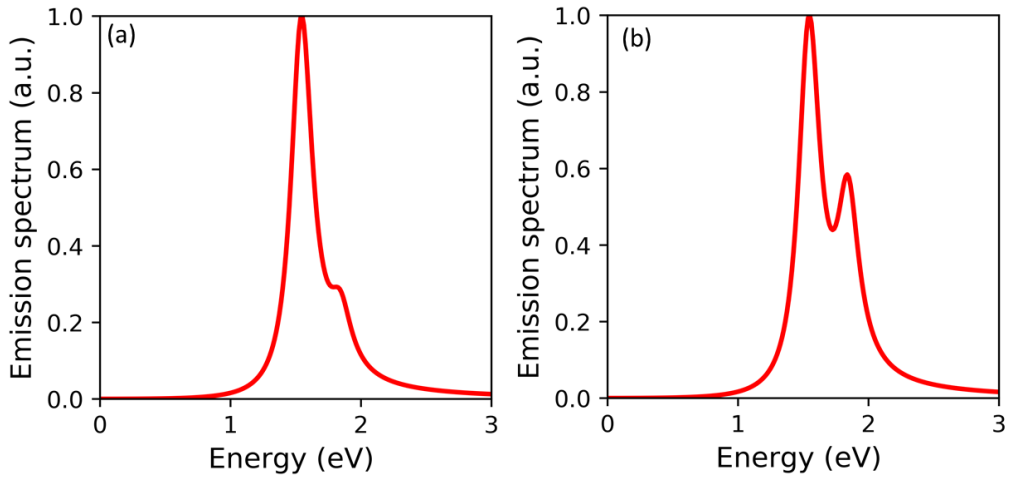

Figure 8.11: Emission spectrum of 2L MoS_2 calculated by using TDDFT without (a) and with electron-phonon interactions included (b). The lower energy peak in emission corresponds to indirect emission, while the higher energy peak corresponds to direct emission.

8.6 Conclusions

Our investigation of the ultrafast excited charge dynamics and emission spectrum of bilayer MoS_2 demonstrate that electron-phonon interaction leads to transfer of electrons from the lowest-energy non-direct-gap Q valleys to the direct-gap K-valleys. This results in photoluminescence spectrum with peaks that correspond to the direct (K valley) and non-direct (LA phonon-assisted K to Γ valley) transitions. The emission spectrum obtained without the inclusion of intervalley dynamics consists of a single peak that corresponds to an indirect emission. The appearance of the second peak with the inclusion of electron-phonon interaction, demonstrates that the latter plays an important role in the ultrafast charge dynamics and photoluminescence in 2L MoS_2. The next step is to establish the contribution of the electron-electron and electron-hole interaction, including exciton effects, into the ultrafast dynamics and emission of the system. Work in this direction is in progress.

CHAPTER 9: CONCLUSION

In this dissertation, I have explored the structural and catalytic properties of metal organic chains both in gas phase and on Au(111) support, using a quantum-mechanical approach, based on density functional theory (DFT). The results presented here provide not only understanding of the properties of metal organic chains but also guidelines for designing novel metal organic complexes for catalytic applications. I have also explored the excitation and optical properties of hydrogenated single-layer and clean bilayer MoS_2 using methods based on DFT, TDDFT and the Liouville equation. Below is a chapter-wise summary of specific conclusions.

In Chapter 3, I describe a detailed screening study of the electronic structure, structural, magnetic and chemical properties of TM-dipyridyltetrazine (DT) based on first-principles DFT. On the basis of structural analysis, we exclude the systems with non-planar coordination. In order to focus on the chemical activity of quasi square-planar structures, we computed the adsorption energies of CO and O_2 and categorized the possible complexes for CO and O_2 reaction.

In Chapter 4, I explore the effect of ligand Bis-Pyrimidine (BP) on chemical state of metal centers in a non-planar metal organic chain formation. I also describe the effect of Au(111) support on the geometry and charge state of V-BP: The Au(111) support alters the non-planar geometry of V-BP and draws charge from V-BP chain. While this means diminished reducing power in the V-BP chain, the surface V-BP assembly retains reducing power, as is evident from observations on the adsorption of O.

In Chapter 5 I present DFT calculations on Metal- Phenanthroline (M-PDO), which both in gas phase and on Au(111) reveal chains with planar MO_2N_2 coordination environment. Both lengths

within PDO of M-PDO complex compared to those in isolated PDO, indicate that the repeating unit in the chains is best considered as M^{2+} PDO^{2-}. Atomic charges reveal decreasing charge transfer from M from to V, to Fe to Pt. V-PDO on Au(111) is calculated to have a planar structure when Au closest to V moves out of the Au surface (towards V) and V moves even further out of the N_2O_2 plane (towards Au) creating a typical V-Au single bond.

In Chapter 6, we clarify the complexation between tetra-aza-anthraquinone (TAAQ) ligand and Fe. TAAQ functions as a redox-active ligand to form complex metal–organic structures. In the case of complexation with Fe, we find that this results in under-population of the binding pockets, due to the limited reduction capacity of the ligand. Rather than achieving uniform di-nuclear centers in straight coordination chains for which the ligands were designed, the abundance of binding pockets leads to multiple binding motifs with comparable energy and disordered structure. We further characterize the TAAQ by carrying out vibrational spectroscopy calculations on gas-phase molecule, gas phase molecular network and both molecule and molecular network on Au(111). We investigate the effect of Au(111) support on calculated IR spectrum of TAAQ molecule and TAAQ monolayer network .

In Chapter 7 we present our study of electronic and excitonic properties of a hydrogenated single-layer MoS_2 system using a combined DFT and TDDFT approach. The existence of a mid-gap excitonic state in a hydrogenated single layer MoS_2, which has relatively large binding energy and long lifetime (large dipole strength) is an important finding by itself, one that may have applications in energy-harvesting technologies.

In Chapter 8 we describe our application of density functional theory in combination with the Liouville equation to examine ultrafast charge dynamics in bilayer MoS_2. We find that electron-phonon interaction has a strong effect on the calculated emission spectrum. Our results thus show the importance of ultrafast charge dynamics in understanding photoemissive properties of a few-layer transition-metal dichalcogenide.

I employed modern quantum-mechanical methods and powerful computational techniques to illustrate a mechanism by which selected metal-organic chains with single and multiple metal centers can be designed so as to control the chemical state of the metal center by using organic lingand with different reducing capabilities. This design principle can thus guide experimental discoveries and industrial applications. I also provide a detailed description of how hydrogenation can be used as a knob to tune the excitation and optical properties of single-layer MoS_2. The study of the interplay between ultrafast charge dynamics and electron-phonon coupling helps in understanding the phonon-assisted intervalley charge dynamics and thus the interpretation of the emission spectrum in 2L MoS_2

APPENDIX A: SUPPLIMENTRY INFORMATION

The Liouville equations and the electron-phonon scattering terms

The density matrix satisfies the Liouville equation:

$$i\frac{\partial\rho_k^{lm}(t)}{\partial t} = [H,\rho]^{lm}(t) \equiv \sum_n \left(H_k^{ln}(t)\rho_k^{nm}(t) - \rho_k^{ln}(t)H_k^{nm}(t)\right) + \left(\frac{\partial\rho_k^{lm}}{\partial t}\right)_{scatt}, \quad (SI.1)$$

where

$$H_k^{ml}(t) = \int \psi_k^{m*}(r)\hat{H}(r,t)\psi_k^{l}(r)dr. \quad (SI.2)$$

The Hamiltonian in the integral in Eq. (SI.2)

$$\hat{H}(r,t) = -\frac{\nabla^2}{2m} + V_{ion}(r) + V_H[n](r) + V_{XC}[n](r) + e\vec{r}\vec{E}(t). \quad (SI.3)$$

consists of the DFT Kohn-Sham Hamiltonian (the first four terms) and the laser-pulse perturbation potential (the last term). The time-dependence of the applied Gaussian pulse is

$$\vec{E}(t) = \vec{E}_0 e^{-\frac{t^2}{\tau^2}}, \quad (SI.4)$$

where $\vec{E}_0 = E_0(1,1,1)$ and $E_0 = 1V/A$ and $\tau = 100fs$ is the pulse duration.

Since

$$\left[-\frac{\nabla^2}{2m} + V_{ion}(r) + V_H[n](r) + V_{XC}[n](r)\right]\psi_k^m(r) = \varepsilon_k^m\psi_k^m(r), \quad (SI.5)$$

the matrix elements (SI.2) have a simple form

$$H_k^{ml} = \varepsilon_k^m\delta^{ml} + \vec{d}_k^{ml}\vec{E}(t), \quad (SI.6)$$

where

$$\vec{d}_k^{ml} = e\int \psi_k^{m*}(r)\vec{r}\psi_k^{l}(r)dr, \quad (SI.7)$$

are the transition dipole moments.

Finally, substituting Eq.(SI.6) into Eq.(SI.1) one obtains the explicit form of the Liouville equations:

$$i\frac{\partial\rho_k^{lm}(t)}{\partial t} = \left(\varepsilon_k^l - \varepsilon_k^m\right)\rho_k^{lm}(t) + \vec{E}(t)\sum_n\left(\vec{d}_k^{ln}\rho_k^{nm}(t) - \rho_k^{ln}(t)\vec{d}_k^{nm}(t)\right) + \left(\frac{\partial\rho_k^{lm}}{\partial t}\right)_{scatt}. \quad \text{(SI. 8)}$$

The diagonal and non-diagonal scattering matrix elements in Eq. (SI.8) have the following form:

$$\begin{aligned}\left(\frac{\partial\rho_k^{ll}}{\partial t}\right)_{scatt} = -2\pi\sum_{q,\nu} g_{q\nu}^2\delta\left(\varepsilon_{k+q}^l - \varepsilon_k^l - \omega_0\right)\{N(\omega_0)\rho_k^{ll}(t)\left[1-\rho_{k+q}^{ll}(t)\right] \\ - (N(\omega_0)+1)\rho_{k+q}^{ll}(t)\left[1-\rho_k^{ll}(t)\right]\} \\ -2\pi\sum_{q,\nu} g_{q\nu}^2\delta\left(\varepsilon_{k-q}^l - \varepsilon_k^l + \omega_0\right)\{(N(\omega_0)+1)\rho_k^{ll}(t)\left[1-\rho_{k-q}^{ll}(t)\right] \\ - N(\omega_0)\rho_{k-q}^{ll}(t)\left[1-\rho_k^{ll}(t)\right]\}, \quad \text{(SI. 9)}\end{aligned}$$

$$\begin{aligned}\left(\frac{\partial\rho_k^{lm}}{\partial t}\right)_{scatt} \\ = -2\pi\sum_{q,\nu,\sigma=\pm1} g_{q\nu}^2\delta\left(\varepsilon_{k+q}^l - \varepsilon_k^m - \sigma\omega_0\right)\{N(\sigma\omega_0)\left[\rho_k^{lm}(t)\rho_{k+\sigma q}^{mm}(t) - \rho_{k+\sigma q}^{lm}(t)\rho_k^{ll}(t)\right] \\ + [N(\sigma\omega_0)+1]\left[\rho_k^{lm}(t)\rho_{k+\sigma q}^{ll}(t) - \rho_{k+\sigma q}^{lm}(t)\rho_k^{mm}(t)\right]\} - \{k \leftrightarrow k+\sigma q\}, \text{(SI. 10)}\end{aligned}$$

where $N(\omega_0) = 1/[\exp[\omega_0/T] - 1]$ is the Bose distribution function with used temperature $T = 0.1eV$ and $\omega_0 = 40meV$ is the effective phonon frequency.

APPENDIX B: LIST OF PUBLICATIONS

Volodymyr Turkowski, **Naseem Ud Din**, Talat S Rahman *"Time-dependent density-functional theory and excitons in bulk and two-dimensional semiconductors"* Computation, 5(3), 39 (2017).

Tobias W Morris, IJ Huerfano, Miao Wang, David L Wisman, Alyssa C Cabelof, **Naseem Ud Din**, Christopher D Tempas, Duy Le, Alexander V Polezhaev, Talat S Rahman, Kenneth G Caulton, Steven L Tait, *"Multi-electron Reduction Capacity and Multiple Binding Pockets in Metal-organic Redox Assembly at Surfaces,"* Chem. Eur. J. , 25, 5565 (2019).

Christopher D Tempas, Tobias W Morris, David L Wisman, Duy Le, **Naseem Ud Din**, Christopher G Williams, MiaoWang, Alexander V Polezhaev, Talat S Rahman, Kenneth G Caulton, Steven L Tait, *"Redox-active ligand-controlled selectivity of vanadium oxidation on Au (100),"* Chem. Sci., 9, 1674 (2018).

Naseem Ud Din, Tao Jiang, Shima Gholam Mirzaeimoghadar, Michael Chini, Volodymyr Turkowski, "Electron-electron correlations and structural, spectral and polarization properties of tetragonal $BaTiO_3$" J, Phys.: Condens. Matter 32, 475601 (2020).

Naseem Ud Din, Volodymyr Turkowski, Talat Rahman, *"Excited states in hydrogenated single-layer MoS_2,"* J. Phys.: Condens. Matter 33, 075201 (2021).

Under Review

Naseem Ud Din, Volodymyr Turkowski, and Talat .S. Rahman, " *Ultrafast charge dynamics and photoluminescence in bilayer MoS_2*" under review 2D materials, October (2020)

(arXiv:2010.14044)

Hung-Tzu Chang, Alexander Guggenmos, Scott K. Cushing, Yang Cui, **Naseem Ud Din**, Shree Ram Acharya, Ilana J. Porter, Ulf Kleineberg, Volodymyr Turkowski, Talat S. Rahman, Daniel M. Neumark, and Stephen R. Leone, *"Electron Thermalization and Relaxation in Laser-Heated Nickel by Few-Femtosecond Core-Level Transient Absorption Spectroscopy"* under review Phy. Rev. B, September (2020) (arXiv:2009.14118)

In Preparation

Naseem Ud Din, Duy Le, and Talat .S. Rahman, "*Linear Transition Metal-Dipyridyltetrazine Chains with Active Metal Sites: A First-Principles Study"*

Tobias W. Morris, **Naseem Ud Din**, David L. Wisman, David A. Duncan, Duy Le, Eman Wasim, Talat S. Rahman, Steven L.Tait, *"Impact of Oxygen Binding on Surface Trans Effect in Metal-Ligand Complexes at Surfaces by X-Ray Standing Wave Spectroscopy"*

LIST OF REFERENCES

[1] M. Valden, X. Lai, and D. W. Goodman, science **281**, 1647 (1998).

[2] A. T. Bell, Science **299**, 1688 (2003).

[3] R. J. White, R. Luque, V. L. Budarin, J. H. Clark, and D. J. Macquarrie, Chemical Society Reviews **38**, 481 (2009).

[4] W. Jung, K. L. Gu, Y. Choi, and S. M. Haile, Energy & Environmental Science **7**, 1685 (2014).

[5] X.-F. Yang, A. Wang, B. Qiao, J. Li, J. Liu, and T. Zhang, Accounts of Chemical Research **46**, 1740 (2013).

[6] M. Born and R. Oppenheimer, Annalen der physik **389**, 457 (1927).

[7] L. H. Thomas, in *Mathematical Proceedings of the Cambridge Philosophical Society* (Cambridge University Press, 1927), pp. 542.

[8] E. Fermi, Zeitschrift für Physik **48**, 73 (1928).

[9] P. Hohenberg and W. Kohn, B864 (1964).

[10] W. Kohn and L. Sham, A1133 **405**, 406 (1965).

[11] S. H. Vosko, L. Wilk, and M. Nusair, Canadian Journal of physics **58**, 1200 (1980).

[12] J. P. Perdew and A. Zunger, Physical Review B **23**, 5048 (1981).

[13] C. Lee, W. Yang, and R. G. Parr, Physical review B **37**, 785 (1988).

[14] J. P. Perdew and Y. Wang, Physical Review B **45**, 13244 (1992).

[15] J. P. Perdew, K. Burke, and M. Ernzerhof, Physical review letters **77**, 3865 (1996).

[16] S. Grimme, Journal of computational chemistry **25**, 1463 (2004).

[17] S. Grimme, Journal of computational chemistry **27**, 1787 (2006).

[18] S. Grimme, J. Antony, S. Ehrlich, and H. Krieg, The Journal of chemical physics **132**, 154104 (2010).

[19] M. Dion, H. Rydberg, E. Schröder, D. C. Langreth, and B. I. Lundqvist, Physical Review Letters **92**, 246401 (2004).

[20] K. Lee, É. D. Murray, L. Kong, B. I. Lundqvist, and D. C. Langreth, Physical Review B **82**, 081101 (2010).

[21] F. Bloch, Zeitschrift für physik **52**, 555 (1929).

[22] H. J. Monkhorst and J. D. Pack, Physical review B **13**, 5188 (1976).

[23] J. C. Phillips, Physical Review **112**, 685 (1958).

[24] D. Hamann, M. Schlüter, and C. Chiang, Physical Review Letters **43**, 1494 (1979).

[25] D. Vanderbilt, Physical review B **41**, 7892 (1990).

[26] P. E. Blöchl, Physical review B **50**, 17953 (1994).

[27] G. Kresse and D. Joubert, Physical review b **59**, 1758 (1999).

[28] R. Bader, (Clarendon Press, Oxford, 1990).

[29] G. Henkelman, A. Arnaldsson, and H. Jónsson, Computational Materials Science **36**, 354 (2006).

[30] E. Runge and E. K. Gross, Physical Review Letters **52**, 997 (1984).

[31] S. Botti, A. Schindlmayr, R. Del Sole, and L. Reining, Reports on Progress in Physics **70**, 357 (2007).

[32] V. Turkowski and C. A. Ullrich, Physical Review B **77**, 075204 (2008).

[33] V. Turkowski, A. Leonardo, and C. A. Ullrich, Physical Review B **79**, 233201 (2009).

[34] W. Hanke and L. Sham, Physical Review B **21**, 4656 (1980).

[35] S. Albrecht, L. Reining, R. Del Sole, and G. Onida, Physical review letters **80**, 4510 (1998).

[36] M. Rohlfing and S. G. Louie, Physical review letters **81**, 2312 (1998).

[37] C. A. Ullrich, *Time-dependent density-functional theory: concepts and applications* (OUP Oxford, 2011).

[38] V. Turkowski, N. U. Din, and T. S. Rahman, Computation **5**, 39 (2017).

[39] R. Del Sole and E. Fiorino, Physical Review B **29**, 4631 (1984).

[40] A. Ramirez-Torres, V. Turkowski, and T. S. Rahman, Physical Review B **90**, 085419 (2014).

[41] J. D. Talman and W. F. Shadwick, Physical Review A **14**, 36 (1976).

[42] M. Norman and D. Koelling, Physical Review B **30**, 5530 (1984).

[43] Z.-h. Yang and C. A. Ullrich, Physical Review B **87**, 195204 (2013).

[44] J. Krieger, Y. Li, and G. Iafrate, Physical Review A **45**, 101 (1992).

[45] A. A. Herzing, C. J. Kiely, A. F. Carley, P. Landon, and G. J. Hutchings, Science **321**, 1331 (2008).

[46] J. Lin *et al.*, Angewandte Chemie International Edition **51**, 2920 (2012).

[47] U. Heiz, A. Sanchez, S. Abbet, and W. D. Schneider, Journal of the American Chemical Society **121**, 3214 (1999).

[48] Y. Lei *et al.*, Science **328**, 224 (2010).

[49] B. Qiao, L. Liu, J. Zhang, and Y. Deng, Journal of Catalysis **261**, 241 (2009).

[50] M. Turner, V. B. Golovko, O. P. H. Vaughan, P. Abdulkin, A. Berenguer-Murcia, M. S. Tikhov, B. F. G. Johnson, and R. M. Lambert, Nature **454**, 981 (2008).

[51] W. E. Kaden, T. Wu, W. A. Kunkel, and S. L. Anderson, Science **326**, 826 (2009).

[52] M. Haruta, T. Kobayashi, H. Sano, and N. Yamada, Chemistry Letters **16**, 405 (1987).

[53] J. M. Thomas, R. Raja, and D. W. Lewis, Angewandte Chemie International Edition **44**, 6456 (2005).

[54] B. Qiao, A. Wang, X. Yang, L. F. Allard, Z. Jiang, Y. Cui, J. Liu, J. Li, and T. Zhang, Nat Chem **3**, 634 (2011).

[55] J. M. Thomas, Z. Saghi, and P. L. Gai, Topics in Catalysis **54**, 588 (2011).

[56] M. Ranocchiari, C. Lothschütz, D. Grolimund, and J. A. van Bokhoven, in *Proc. R. Soc. A* (The Royal Society, 2012), pp. 1985.

[57] M. Flytzani-Stephanopoulos and B. C. Gates, in *Annual Review of Chemical and Biomolecular Engineering, Vol 3*, edited by J. M. Prausnitz2012), pp. 545.

[58] L. F. Allard, A. Borisevich, W. Deng, R. Si, M. Flytzani-Stephanopoulos, and S. H. Overbury, Journal of Electron Microscopy **58**, 199 (2009).

[59] Q. Fu, H. Saltsburg, and M. Flytzani-Stephanopoulos, Science **301**, 935 (2003).

[60] J. Boscoboinik, J. Kestell, M. Garvey, M. Weinert, and W. T. Tysoe, Topics in Catalysis **54**, 20 (2011).

[61] S. L. Tait, Y. Wang, G. Costantini, N. Lin, A. Baraldi, F. Esch, L. Petaccia, S. Lizzit, and K. Kern, Journal of the American Chemical Society **130**, 2108 (2008).

[62] H.-H. Yang, Y.-H. Chu, C.-I. Lu, T.-H. Yang, K.-J. Yang, C.-C. Kaun, G. Hoffmann, and M.-T. Lin, ACS Nano **7**, 2814 (2013).

[63] D. Skomski, C. D. Tempas, K. A. Smith, and S. L. Tait, Journal of the American Chemical Society **136**, 9862 (2014).

[64] D. Skomski, C. D. Tempas, B. J. Cook, A. V. Polezhaev, K. A. Smith, K. G. Caulton, and S. L. Tait, Journal of the American Chemical Society **137**, 7898 (2015).

[65] D. Le and T. S. Rahman, Faraday Discussions **204**, 83 (2017).

[66] P. Giannozzi *et al.*, Journal of physics: Condensed matter **21**, 395502 (2009).

[67] J. Klimeš, D. R. Bowler, and A. Michaelides, Physical Review B **83**, 195131 (2011).

[68] C. D. Tempas *et al.*, Chemical science **9**, 1674 (2018).

[69] D. Skomski, C. D. Tempas, G. S. Bukowski, K. A. Smith, and S. L. Tait, The Journal of Chemical Physics **142**, 101913 (2015).

[70] G. Kresse and J. Furthmüller, Computational materials science **6**, 15 (1996).

[71] P. Janthon, S. Luo, S. M. Kozlov, F. Viñes, J. Limtrakul, D. G. Truhlar, and F. Illas, Journal of Chemical Theory and Computation **10**, 3832 (2014).

[72] P. H. T. Philipsen and E. J. Baerends, Physical Review B **54**, 5326 (1996).

[73] Z.-T. Wang, M. T. Darby, A. J. Therrien, M. El-Soda, A. Michaelides, M. Stamatakis, and E. C. H. Sykes, The Journal of Physical Chemistry C **120**, 13574 (2016).

[74] J. Liu, J. Shan, F. R. Lucci, S. Cao, E. C. H. Sykes, and M. Flytzani-Stephanopoulos, Catalysis Science & Technology **7**, 4276 (2017).

[75] J. Liu, F. R. Lucci, M. Yang, S. Lee, M. D. Marcinkowski, A. J. Therrien, C. T. Williams, E. C. H. Sykes, and M. Flytzani-Stephanopoulos, Journal of the American Chemical Society **138**, 6396 (2016).

[76] M. D. Marcinkowski, J. Liu, C. J. Murphy, M. L. Liriano, N. A. Wasio, F. R. Lucci, M. Flytzani-Stephanopoulos, and E. C. H. Sykes, ACS Catalysis **7**, 413 (2017).

[77] A. J. Therrien, A. J. Hensley, M. D. Marcinkowski, R. Zhang, F. R. Lucci, B. Coughlin, A. C. Schilling, J.-S. McEwen, and E. C. H. Sykes, Nature Catalysis **1**, 192 (2018).

[78] K. C. Szeto *et al.*, The Journal of Physical Chemistry C **119**, 26611 (2015).

[79] D. R. Hartline, M. Zeller, and C. Uyeda, Journal of the American Chemical Society **139**, 13672 (2017).

[80] S. Pal and C. Uyeda, Journal of the American Chemical Society **137**, 8042 (2015).

[81] I. G. Powers, J. M. Andjaba, X. Luo, J. Mei, and C. Uyeda, Journal of the American Chemical Society **140**, 4110 (2018).

[82] H. R. Rounds, M. Zeller, and C. Uyeda, Organometallics **37**, 545 (2018).

[83] Y.-Y. Zhou, D. R. Hartline, T. J. Steiman, P. E. Fanwick, and C. Uyeda, Inorganic chemistry **53**, 11770 (2014).

[84] S. Fabris, S. Stepanow, N. Lin, P. Gambardella, A. Dmitriev, J. Honolka, S. Baroni, and K. Kern, Nano letters **11**, 5414 (2011).

[85] J. Čechal, C. S. Kley, R. m. Pétuya, F. Schramm, M. Ruben, S. Stepanow, A. Arnau, and K. Kern, The Journal of Physical Chemistry C **120**, 18622 (2016).

[86] Z. Liang, Q. Tang, J. Liu, J. Li, F. Yan, and Q. Miao, Chemistry of materials **22**, 6438 (2010).

[87] S. Miao, A. L. Appleton, N. Berger, S. Barlow, S. R. Marder, K. I. Hardcastle, and U. H. Bunz, Chemistry–A European Journal **15**, 4990 (2009).

[88] A. Togo, L. Chaput, and I. Tanaka, Physical Review B **91**, 094306 (2015).

[89] T. W. Morris *et al.*, Chemistry–A European Journal **25**, 5565 (2019).

[90] M. M. Furchi, D. K. Polyushkin, A. Pospischil, and T. Mueller, Nano Letters **14**, 6165 (2014).

[91] M. Buscema, J. O. Island, D. J. Groenendijk, S. I. Blanter, G. A. Steele, H. S. J. van der Zant, and A. Castellanos-Gomez, Chemical Society Reviews **44**, 3691 (2015).

[92] O. Lopez-Sanchez, D. Lembke, M. Kayci, A. Radenovic, and A. Kis, Nat Nano **8**, 497 (2013).

[93] A. Splendiani, L. Sun, Y. Zhang, T. Li, J. Kim, C.-Y. Chim, G. Galli, and F. Wang, Nano Letters **10**, 1271 (2010).

[94] H. J. Conley, B. Wang, J. I. Ziegler, R. F. Haglund, S. T. Pantelides, and K. I. Bolotin, Nano Letters **13**, 3626 (2013).

[95] Y. Li, S. Tongay, Q. Yue, J. Kang, J. Wu, and J. Li, Journal of Applied Physics **114**, 174307 (2013).

[96] V. P. Santos *et al.*, ACS Catalysis **3**, 1634 (2013).

[97] A. Andersen, S. M. Kathmann, M. A. Lilga, K. O. Albrecht, R. T. Hallen, and D. Mei, The Journal of Physical Chemistry C **115**, 9025 (2011).

[98] A. Kotarba, G. Adamski, W. Piskorz, Z. Sojka, C. Sayag, and G. Djéga-Mariadassou, The Journal of Physical Chemistry B **108**, 2885 (2004).

[99] Y. Cai, Z. Bai, H. Pan, Y. P. Feng, B. I. Yakobson, and Y.-W. Zhang, Nanoscale **6**, 1691 (2014).

[100] T. Komesu *et al.*, Applied Physics Letters **105**, 241602 (2014).

[101] M. Tosun, S. Chuang, H. Fang, A. B. Sachid, M. Hettick, Y. Lin, Y. Zeng, and A. Javey, ACS Nano **8**, 4948 (2014).

[102] T. Komesu *et al.*, Journal of Physics: Condensed Matter **29**, 285501 (2017).

[103] Y. Qu, H. Pan, and C. T. Kwok, **6**, 34186 (2016).

[104] D. Pierucci *et al.*, ACS nano **11**, 1755 (2017).

[105] L. Bartels, private communication (2017).

[106] K. Y. Ma, S. I. Yoon, A.-R. Jang, H. Y. Jeong, Y.-J. Kim, P. K. Nayak, and H. S. Shin, Journal of Materials Chemistry C **5**, 11294 (2017).

[107] H. Shi, H. Pan, Y.-W. Zhang, and B. I. Yakobson, Physical Review B **88**, 205305 (2013).

[108] G. W. Jeon, K. W. Lee, and C. E. Lee, Physica E: Low-dimensional Systems and Nanostructures **104**, 309 (2018).

[109] D. C. Sorescu, D. S. Sholl, and A. V. Cugini, The Journal of Physical Chemistry B **108**, 239 (2004).

[110] Y. Xu, Y. Li, X. Chen, C. Zhang, R. Zhang, and P. Lu, Aip Advances **6**, 075001 (2016).

[111] B. Shao, M. Schüler, G. Schönhoff, T. Frauenheim, G. Czycholl, and T. O. Wehling, Nano Letters **17**, 6721 (2017).

[112] J. Zou, L.-M. Tang, K. Chen, and Y. Feng, Journal of Physics: Condensed Matter **30**, 065001 (2018).

[113] -. W. Dan, -. Z. Juan, and -. T. Li-Ming, - Acta Physica Sinica - **68** (2019).

[114] G. Savini, A. Ferrari, and F. Giustino, Physical review letters **105**, 037002 (2010).

[115] V. Loktev and V. Turkowski, Journal of Low Temperature Physics **164**, 264 (2011).

[116] M. E. Casida, in *Recent Advances In Density Functional Methods: (Part I)* (World Scientific, 1995), pp. 155.

[117] A. Fetter and J. Walecka, (McGraw Hill, 1971).

[118] R. Ruger, E. Van Lenthe, Y. Lu, J. Frenzel, T. Heine, and L. Visscher, Journal of chemical theory and computation **11**, 157 (2015).

[119] M. Dresselhaus, G. Dresselhaus, S. Cronin, and A. Filho, Solid State Properties: From Bulk to Nano, Graduate Texts in Physics, (Springer, Berlin, 2018).

[120] A. Ramasubramaniam, Physical Review B 86**,** 115409 (2012).

[121] P. Johari and V. B. Shenoy, ACS Nano 6, 5449 (2012).

[122] Y. Ding, Y. Wang, J. Ni, L. Shi, S. Shi, and W. Tang, Physica B: Condensed Matter 40**6,** 2254 (2011).

[123] K. F. Mak, C. Lee, J. Hone, J. Shan, and T. F. Heinz, Physical Review Letters 10**5,** 136805 (2010).

[124] T. Komesu e*t al.*, Applied Physics Letters 10**5,** 241602 (2014).

[125] F. Ersan, G. k. Gökoğlu, and E. Aktürk, The Journal of Physical Chemistry C 11**9,** 28648 (2015).

[126] K. F. Mak, C. Lee, J. Hone, J. Shan, and T. F. Heinz, Physical review letters 10**5,** 136805 (2010).

[127] F. Wu, F. Qu, and A. H. Macdonald, Physical Review B 91**,** 075310 (2015).

[128] K. S. Novoselov, D. Jiang, F. Schedin, T. Booth, V. Khotkevich, S. Morozov, and A. K. Geim, Proceedings of the National Academy of Sciences 10**2,** 10451 (2005).

[129] Q. H. Wang, K. Kalantar-Zadeh, A. Kis, J. N. Coleman, and M. S. Strano, Nature nanotechnology 7, 699 (2012).

[130] M. Chhowalla, H. S. Shin, G. Eda, L.-J. Li, K. P. Loh, and H. Zhang, Nature chemistry 5, 263 (2013).

[131] S. Wu e*t al.*, Nature Physics 9, 149 (2013).

[132] S. Tongay, J. Zhou, C. Ataca, K. Lo, T. S. Matthews, J. Li, J. C. Grossman, and J. Wu, Nano letters 12**,** 5576 (2012).

[133] D. Braga, I. Gutiérrez Lezama, H. Berger, and A. F. Morpurgo, Nano letters 12**,** 5218 (2012).

[134] W. Zhao, Z. Ghorannevis, L. Chu, M. Toh, C. Kloc, P.-H. Tan, and G. Eda, ACS nano 7, 791 (2013).

[135] Q. Gao, Z. Zhang, X. Xu, J. Song, X. Li, and Y. Wu, Nature communications 9, 1 (2018).

[136] T. Kümmell, W. Quitsch, S. Matthis, T. Litwin, and G. Bacher, Physical Review B 91**,** 125305 (2015).

[137] Y. Li, Y. Rao, K. F. Mak, Y. You, S. Wang, C. R. Dean, and T. F. Heinz, Nano letters 13**,** 3329 (2013).

[138] S.-Y. Chen, C. Zheng, M. S. Fuhrer, and J. Yan, Nano letters 15**,** 2526 (2015).

[139] G. Plechinger, F. Mooshammer, A. Castellanos-Gomez, G. Steele, C. Schüller, and T. Korn, 2D Materials 2, 034016 (2015).

[140] T. Jiang, H. Liu, D. Huang, S. Zhang, Y. Li, X. Gong, Y.-R. Shen, W.-T. Liu, and S. Wu, Nature nanotechnology 9, 825 (2014).

[141] K. Liu e*t al.*, Nature communications 5, 1 (2014).

[142] B. R. Carvalho, L. M. Malard, J. M. Alves, C. Fantini, and M. A. Pimenta, Physical review letters 11**4,** 136403 (2015).

[143] A. Molina-Sánchez, K. Hummer, and L. Wirtz, Surface Science Reports 70**,** 554 (2015).

[144] R. Pisoni, T. Davatz, K. Watanabe, T. Taniguchi, T. Ihn, and K. Ensslin, Physical Review Letters 12**3,** 117702 (2019).

[145] Y. Chen e*t al.*, Nano letters 17**,** 194 (2017).

[146] H. J. Conley, B. Wang, J. I. Ziegler, R. F. Haglund Jr, S. T. Pantelides, and K. I. Bolotin, Nano letters 13**,** 3626 (2013).

[147] I. Neri and M. López-Suárez, Physical Review B 97**,** 241408 (2018).

[148] A. Kormányos, V. Zólyomi, V. I. Fal'ko, and G. Burkard, Physical Review B 98**,** 035408 (2018).

[149] H.-P. Komsa and A. V. Krasheninnikov, Physical Review B 86**,** 241201 (2012).

[150] A. Molina-Sánchez, D. Sangalli, K. Hummer, A. Marini, and L. Wirtz, Physical Review B 88**,** 045412 (2013).

[151] H. Yu, Y. Wang, Q. Tong, X. Xu, and W. Yao, Physical review letters 11**5,** 187002 (2015).

[152] H. Haug and S. Koch, World Scientific, Singapore (1990).

[153] G. Froehlicher, E. Lorchat, O. Zill, M. Romeo, and S. Berciaud, Journal of Raman Spectroscopy 49**,** 91 (2018).

[154] N. Scheuschner, R. Gillen, M. Staiger, and J. Maultzsch, Physical Review B 91**,** 235409 (2015).

[155] Á. Szabó, R. Rhyner, and M. Luisier, Physical Review B 92**,** 035435 (2015).

[156] H. Shi, R. Yan, S. Bertolazzi, J. Brivio, B. Gao, A. Kis, D. Jena, H. G. Xing, and L. Huang, ACS nano 7, 1072 (2013).

[157] T. Yu and M. Wu, Physical Review B 93**,** 045414 (2016).

[158] D. A. Ruiz-Tijerina, M. Danovich, C. Yelgel, V. Zólyomi, and V. I. Fal'ko, Physical Review B 98**,** 035411 (2018).

[159] D. Xiao, G.-B. Liu, W. Feng, X. Xu, and W. Yao, Physical Review Letters 10**8,** 196802 (2012).

[160] S. R. Acharya, V. Turkowski, G. Zhang, and T. S. Rahman, Physical Review Letters 12**5,** 017202 (2020).

[161] M. Dresselhaus, G. Dresselhaus, S. B. Cronin, and A. G. Souza Filho, (2018).

[162] T. P. Pearsall, in Qu*antum Photonics,* edited by T. P. Pearsall (Springer International Publishing, Cham, 2017), pp. 201.

[163] T. Cheiwchanchamnangij and W. R. Lambrecht, Physical Review B 85**,** 205302 (2012).

[164] J. Padilha, H. Peelaers, A. Janotti, and C. Van de Walle, Physical Review B 90**,** 205420 (2014).

[165] S. Ahmad and S. Mukherjee, Graphene Vol.3 No.4 , (2014).

[166] W. S. Yun, S. Han, S. C. Hong, I. G. Kim, and J. Lee, Physical Review B 85**,** 033305 (2012).

[167] Y. Fu e*t al.,* npj Quantum Materials 2, 1 (2017).

[168] C.-H. Chang, X. Fan, S.-H. Lin, and J.-L. Kuo, Physical Review B 88**,** 195420 (2013).